POLITECNICO DI MILANO
DEPARTMENT OF ENERGY

DOCTORAL PROGRAM IN
ENERGY AND NUCLEAR SCIENCE AND TECHNOLOGY

NOVEL APPROACHES FOR CFD MODELING OF DIESEL ENGINES

Doctoral Dissertation of:
Roberto Torelli

Supervisors:
Prof. Gianluca D'Errico
Dr. Robert M. McDavid
Dr. Vagelis Ikonomou

Tutor:
Prof. Angelo Onorati

The Chair of the Doctoral Program:
Prof. Carlo Enrico Bottani

2015 - XXVII Cycle STEN

Acknowledgements

First of all, I would like to acknowledge Caterpillar Inc. for providing the grant that sponsored my PhD and made this work possible. In particular, I want to thank Dr. Robert M. McDavid and Dr. Vagelis Ikonomou for their support and for the fruitful exchange of knowledge and ideas we carried out in these last three years.

A huge "thank you" goes to my supervisor, Prof. Gianluca D'Errico. He always encouraged my work and gave me the opportunity to grow as a researcher, letting my ideas and myself be fully expressed. Thanks to him, I had the chance to be part of a very stimulating environment and a wonderful research group.

A special mention goes to my tutor, Prof. Angelo Onorati, who always had the right word of advice and was a reference point during my doctorate.

The rest of the group at Politecnico di Milano, thank you all. Prof. Ferrari, Dr. Lucchini, Dr. Montenegro, Dr. Piscaglia, Dr. Cerri, Dr. Montorfano and Dr. Della Torre, you are among the most qualified and expert researchers I ever met and it was an honor to work side by side with all of you. I also want to thank all of my PhD colleagues with whom I shared more than just our office. Thank you all, it was a big pleasure and I wish you the best.

Another very important mention goes to Dr. Sibendu Som at Argonne National Laboratory, Lemont IL, USA. The six month period I spent at ANL gave me the opportunity to focus on diesel spray modeling and go deeply into the details of the physical mechanisms involved. Thanks to him, I had the chance to appreciate a high level research environment and to work side by side with very talented experts.

My girlfriend, Angela. Thank you so much for being there every moment I needed you and we both know which those moments were. I am so lucky to have you in my life and I could not ask for more. Thank you.

Finally, I would like to thank my mother Rosaria, my brother Salvatore and, most of all, my father Giovanni. He is not here anymore and I am so sorry he will not share with me and my family the joy I am experiencing in this moment of big achievement. Thank you dad, I made it and I made it also because of you.

Abstract

The present work focuses on the development of computational tools to model Diesel sprays in both constant volume vessels and engine applications in the context of RANS simulations.

Particular attention is dedicated to Eulerian-Lagrangian modeling of sprays: liquid-gas interaction and breakup mechanisms are deeply investigated and a new approach for exchange of mass, momentum and energy between the phases is presented.

Detailed description of development, implementation, testing and validation of the new methodology is discussed and results are evaluated comparing them with an available set of experimental data.

A novel methodology for automatic Cartesian grids generation is then presented and the application of it to both open "cold flow" and closed cycles is discussed. Different mesh sizes and discretization orders are evaluated and a validation of the mesh generation algorithm is proposed by means of comparison to both academic and industrial cases.

All the models used in this work were implemented within the OpenFOAM framework, as a contribution to the library "Lib-ICE", developed by the Internal Combustion Engine group of the Energy Department of Politecnico di Milano.

Publications

List of publications related to the discussed topics with author's contributions:

- R. Torelli, G. D'Errico, T. Lucchini, V. Ikonomou, R. M. McDavid
  "A Spherical Volume Interaction DDM Approach for Diesel Spray Modeling"
  Atomization and Spray Paper, May 2014
  DOI: 10.1615/AtomizSpr.2015010623
- T. Lucchini, M. Fiocco, R. Torelli, G. D'Errico
  "Automatic Mesh Generation for Full-Cycle CFD Modeling of IC Engines: Application to the TCC Test Case"
  SAE Technical Paper n. 2014-01-1131, April 2014
  DOI: 10.4271/2014-01-1131

Contents

List of Figures

List of Tables

CHAPTER 1

Introduction

1.1 Background

The thesis focuses on the development, implementation, testing and validation of computational tools for Diesel Engines modeling. Different aspects were investigated with a special attention on the Eulerian-Lagrangian description of the injection process and on the interaction of the injected liquid fuel with Cartesian mesh structures. Critical aspects were pointed out, mainly concerning the dependency of energy and momentum exchange between the phases on the spray-grid mutual orientation.

The first half of the thesis deals particularly with the effect that the adoption of Cartesian grid structures can have if evaluated on varying the injector nozzle position with respect to the cell hosting it. To this end, an implementation and evaluation of a novel approach for describing exchange of mass, momentum and energy in Diesel spray CFD simulations based on the Discrete Droplet Modeling (DDM) is presented. During the calculation, each parcel in the domain is surrounded by a spherical volume of ambient gas and interacts first with it instead of interacting directly with the cell volume hosting the parcel. In this way, the interaction volume is independent of the mesh and can be located in more than one cell. This model was implemented using the OpenFOAM® CFD opensource C++ library. It was developed with the aim to reduce grid dependencies related to spray-grid mutual orientation and to the choice of the injector nozzle position with respect to the cell hosting it.

All the sub-models constants were set to match experimental data of a chosen baseline case in non-reactant vaporizing conditions. Then the new approach predictions were firstly compared with standard DDM, initially by moving the injector position within the hosting cell and later by varying ambient density and injection pressure of fuel. In addition, a study of the dependency of the results on the spray-grid mutual orientation was carried out. High-speed imaging and Rayleigh-scattering measurements taken from the Engine Combustion Network (ECN) web database were used to assess numerical results: a good accuracy in the predictions of liquid and vapor spray penetration as well as axial and radial mixture fraction profiles, can be simultaneously achieved on varying thermo-physical and geometrical settings. If applied to engine calculations, the reduced dependency on the nozzle position becomes appreciable when injectors with multiple nozzles are used.

The second part of the thesis focuses on the development of an automated procedure for Cartesian grid generation. The definition of a robust methodology to perform a full-cycle CFD simulation of IC engines requires as first step the availability of a reliable grid generation tool, which does not have to guarantee only a high quality mesh but has to prove also to be efficient in terms of required time. In this part a novel approach entirely based on the OpenFOAM technology is presented. The available 3D grid generator was employed to automatically create meshes containing hexahedra and split-hexahedra from triangulated surface geometries in Stereolithography format. The possibility to introduce local refinements and boundary layers makes this tool suitable for IC engine simulations. Grids are sequentially generated at target crank angles, which are automatically determined depending on user specified settings such as maximum mesh validity interval and quality parameters like non-orthogonality, skewness and aspect ratio. This ensures high quality grids for the entire cycle and requires a reduced amount of user time. Experimental validation was carried out by simulating the full cycle in the so-called TCC (Transparent Combustion Chamber) engine, whose experimental data are available through the ECN database. In particular, a detailed comparison between computed and experimental in-cylinder pressure, turbulence intensity distribution and velocity field was performed so that it was possible to assess the requirements in terms of minimum mesh size and numerical method accuracy to be employed with the proposed methodology.

The final part shows the extension of the automatic Cartesian mesh generation process to sector grids for simulating full-cycle simulations involving injection of fuel and combustion. The choice to use sector meshes implies the hypothesis of axial symmetry, which is commonly accepted when the injector is located at the center of the cylinder head (typical of Diesel applications). The adoption of sector meshes requires the application of cyclic boundary conditions and consequently the perfect correspondence between points and faces on the two sides of the sector. Many features were added to the original approach so that Cartesian sector grids could be generated in OpenFOAM. The grids were generated starting from a real heavy-duty engine geometry and then tested and validated qualitatively and quantitatively on varying minimum mesh size. Detailed chemistry modeling coupled with Multizone discretization and In Situ Online Tabulation was adopted to describe the combustion process.

Good agreement and limited mesh dependency were found showing that this approach could be generally suitable for engine simulations and hence for application to industrial cases.

All the models, solvers and utilities used in this work were implemented within the OpenFOAM framework, as a contribution to the library "Lib-ICE", developed by the Internal Combustion Engine group of the Energy Department at Politecnico di Milano.

CHAPTER 2

Introduction to Lagrangian Modeling of sprays

2.1 Background

It is well known that spray processes play a key role in many technical systems and industrial applications. Examples include cooling systems, spray painting, humidification as well as spray combustion in gas turbines, rockets and, especially, Diesel and gasoline engines. In internal combustion engines the use of sprays is necessary to guarantee the mixing of liquid fuel with air and at the same time increase liquid surface area to obtain a more rapid evaporation and combustion. To have an idea, on a first order approximation, the evaporation rate is proportional to the overall surface area of the liquid, so atomizing a 2 mm drop into more or less eight million droplets of $10\,\mu\mathrm{m}$ increases the evaporation rate by a factor of 200. Moreover, in direct injection engines (both diesel and spark ignition), where the fuel is injected directly into the combustion chamber in order to form an ignitable mixture with air, defining an appropriate injection law for the spray is one of the most effective measures to control the combustion process. The kinetic energy of the liquid droplets represents the main source for turbulence production within the combustion chamber, and therefore governs the microscale air-fuel mixing by turbulent diffusion as well as the flame speed of a premixed flame front. The spray significantly affects the ignition behavior, heat release and pollutant formation rates and thus the noise level, fuel consumption and exhaust emissions of an engine. Therefore, a full understanding of spray processes is fundamental for the design of modem combustion engines which are characterized by more and more flexible injection rate shapes. At the same time, spray phenomena are very complex: the liquid fuel droplets interact in multiple ways with the turbulent gas phase and with the flame itself. Furthermore, engine combustion chambers represent a hostile environment that is hard to access with appropriate measuring techniques. Geometric and thermal boundary conditions experienced in the production engine are easily altered by the interaction of the necessary tools and sensors with the physical domain. All these complications make difficult to assess the quality of spray models identifying numerical simulations as a powerful tool able to provide valuable insight into spray processes and the complex interacting subprocesses involved. They allow access to any process or state variable at any position at any given point in time. If validated for a certain range of boundary conditions, spray models can effectively be utilized to interpret available experimental data and, with a certain confidence, also to obtain predictions for altered operating conditions. The depth of analysis possible with spray models has increased significantly over the past decades, also thanks to undoubted advances in computer technology and parallelization of codes. This trend is likely to continue such that spray modeling with CFD codes will be essential in the development of new engines and combustion systems in the near future.

2.2 Spray Regimes

Fig. 2.1 summarizes the most important spray regimes which affect both dynamics and evaporation of drops. Directly at the nozzle orifice an intact core of the liquid phase can be identified. It rapidly disintegrates into ligaments (churning flow) and further downstream into droplets, where it still occupies a considerable fraction of the two-phase mixture. In this region the spray is termed "thick" (or dense) and it is typically found in the immediate vicinity of the nozzle exit. At the other extreme, and in practical sprays, the liquid diverges away from the nozzle where the size of the drops is reduced due to evaporation and breakup. The spray drops far from the nozzle become isolated and have negligible mass and volume compared to that of the gas that was set in motion by the spraying process. In this case, the spray is termed "very thin" (or dilute) and, even if the drops continue to exchange mass, momentum and energy with the gas, the state of the gas is not altered appreciably by the exchange. The intermediate spray regime between the "very thin" and the "thick" regimes has been identified as "thin" spray [9]. Here, because of the conical spray shape and liquid evaporation, the average spacing between droplets expands further downstream of the nozzle, and the void fraction, i.e. the volume fraction occupied by the gas phase, increases and approaches unity. However, due to the liquid to gas density ratio, the mass fraction of the liquid phase may still be noticeable.

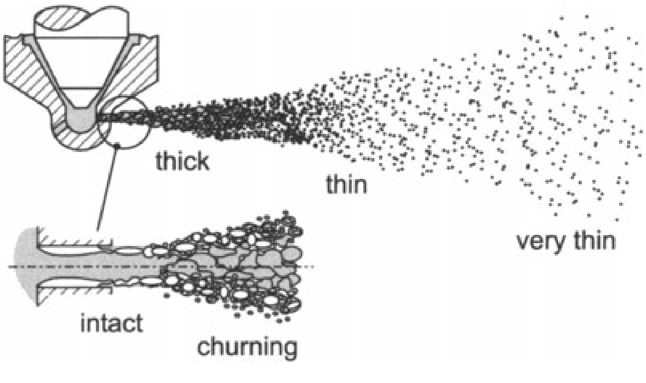

Figure 2.1: *Spray regimes* [1]

The behavior of various droplets within different regimes of a spray is quite different. Close to the nozzle orifice, droplet to droplet interactions such as collision and coalescence can be significant. Moreover, when the droplet spacing is small the boundary layer around a droplet may be affected by an adjacent droplet. As a matter of principle, it can no longer be assumed that there is an undisturbed gas phase around the droplet in order to calculate the exchange processes between liquid and gas. At the other extreme, in the dilute spray regime the droplet behavior can be calculated based on relations for an isolated droplet with good accuracy. Collisions between droplets are rare and typically neglected in the modeling. In the intermediate thin spray regime the liquid phase still accounts for a noticeable mass fraction as already pointed out. Here, momentum transfer from the droplets to the gas phase is considerable and, as a result, affects other droplets again. For instance, the reduced drag forces on those droplets located in the wake of the spray tip that are decelerated by the gas less rapidly and may therefore reach the droplets at the former spray tip that have been injected at an earlier timing. While the qualitative difference in the behavior of the two-phase flow is distinct between the various spray regimes, the transitions between the regimes are continuous and their definitions are somewhat arbitrary. Typically, they are defined in terms of the void fraction:

$$\theta = 1 - \iiint f \frac{4}{3}\pi r^3 \, dr \, d\mathbf{U}_d \, dT_d \tag{2.1}$$

In Eq. 2.1 f is the probable number of droplets per unit volume in the spray. It depends on time t, and on some droplet related quantities like radius r, temperature T_d, position $\mathbf{P}$ and velocity $\mathbf{U}_d$.

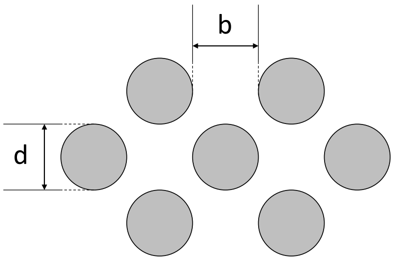

Figure 2.2: *Packing geometry for drops with diameter, d, spaced a distance, b, apart.*

For a regular arrangement of spherical droplets with a spacing equal to b as it is displayed in Fig. 2.2, it can be shown that the void fraction ca be calculated as:

$$\theta = 1 - \frac{\pi}{3\sqrt{3}(1 + b/d)^3} \tag{2.2}$$

so when the drops are spaced one drop diameter apart $\theta` = 0.92$ (i.e., when $b = d$). Consequently, it is often assumed that a spray behaves as a thick spray if the void fraction is less than about 0.9. O'Rourke [9] also considered an additional spray regime located between the intact core and the thick spray, termed "churning flow", for void fractions less than 0.5. The reason behind it is that for liquid volume fractions in excess of 50 %, the liquid can no longer be assumed to be fully dispersed within a continuous gas phase and a different set of equations becomes necessary to describe the problem.

However, there are still considerable uncertainties in the governing equations. This spray regime, which only applies to an extremely small volume close to the nozzle orifice, is often neglected in practical applications. Most available CFD-codes utilized in combustion engine simulations are based on thin or dilute spray assumptions. These assumptions are justified when the computation begins someway downstream of the injection nozzle where the spray has already been diluted by the gas phase. But even if the injector is located within the computational domain, a thin spray may still be assumed when the computational grid cell is large compared to the size of the nozzle hole. In typical combustion engine applications, minimum mesh size is in the range between 0.25 and 0.5 mm whereas a modern passenger car diesel injector has a hole diameter of only about 0.15 mm. Approximations of thick spray effects can later be added by superimposing submodels to the conservation and exchange equations.

2.3 The Spray Equation

2.3.1 Equations and exchange terms

In typical diesel sprays the liquid fuel is atomized into a number of up to 100 millions droplets with average diameters in the ten-micrometer range. These numbers make it prohibitive to resolve each single droplet in numerical simulations. Instead, some kind of statistical averaging technique becomes necessary with additional submodels in order to describe the subscale processes.

Generally the problem can be defined by the so-called spray equation as formulated by Williams [10]. In this approach the probable number of drops per unit volume at time t, that are located between position $\mathbf{P}$ and $\mathbf{P} + d\mathbf{P}$ and characterized by a velocity between $\mathbf{U}_d$ and $\mathbf{U}_d + d\mathbf{U}_d$, a radius between r and $r + dr$ and a temperature between T_d and $T_d + dT_d$ is described with the probability density function f. Since both the droplet position $\mathbf{P}$ and its velocity $\mathbf{U}_d$ have three spatial coordinates, f has a total of nine independent variables:

$$\frac{\text{probable number of droplets}}{\text{unit volume}} = f(\mathbf{P}, \mathbf{U}_d, r, T_d, t)\, d\mathbf{U}_d\, dr\, dT_d \tag{2.3}$$

It should be noted, that the above formulation is based on the assumption that the droplets are ideally spherical and that their size or mass is thus explicitly defined by their radius r. However, this assumption is valid only if the relative velocity between gas and droplet is small, which is not generally the case in typical engine sprays. Especially, in the vicinity of the injection nozzle considerable relative velocities between liquid and gas phases are encountered, such that aerodynamic forces cause droplet distortion and even breakup. Therefore, in most CFD-codes applied for engine simulations with spray combustion, two additional independent variables are included in the distribution function: the droplet distortion parameter y and its temporal rate of change $\dot{y}$. Thus, f becomes a function of eleven independent variables, and Eq. 2.3 now reads:

$$\frac{\text{probable number of droplets}}{\text{unit volume}} = f(\mathbf{P}, \mathbf{U}_d, r, T_d, y, \dot{y}, t)\, d\mathbf{U}_d\, dr\, dT_d\, dy\, d\dot{y} \tag{2.4}$$

The temporal and spatial evolution of the distribution function is described by a conservation equation which can be derived phenomenologically in analogy to the conservation equations of the gas phase [10]. It is commonly referred to as the spray equation and can be written as:

$$\frac{\partial f}{\partial t} = -\frac{\partial}{\partial \mathbf{P}_i}(f\mathbf{U}_{d,i}) - \frac{\partial}{\partial \mathbf{U}_{d,i}}(f\mathbf{F}_i) - \frac{\partial}{\partial r}(fR) - \frac{\partial}{\partial T_d}(f\dot{T}_d) - \frac{\partial}{\partial y}(f\dot{y}) - \frac{\partial}{\partial \dot{y}}(f\ddot{y}) + \dot{f}_{coll} + \dot{f}_{bu} \tag{2.5}$$

Eq. 2.5 follows the Einstein convention. $\mathbf{F}$ denotes a force per unit mass, i.e. an acceleration. Thus the component $\mathbf{F}_i$ is the acceleration along the spatial coordinate $\mathbf{P}_i$ ($\mathbf{F}_i = d\mathbf{U}_{d,i}/dt$). R, $\dot{T}_d$ and $\ddot{y}$ are the time rates of change of droplet radius r, temperature T_d and oscillation velocity $\dot{y}$. The source terms f_{coll} and f_{bu} account for changes in the distribution function due to droplet collision and breakup, respectively.

The solution of the spray equation gives the so-called source or exchange terms that describe the interactions between the liquid and gas phases. In order to assure conservation of mass, momentum and energy of the total (two-phase) system, these terms need to be included in the gas phase conservation equations. The source term accounting for mass evaporation of the liquid droplets becomes (Reitz [6]):

$$\dot{\rho}^s = -\int f\rho_l 4\pi r^2 R \, d\mathbf{U}_d \, dr \, dT_d \, dy \, d\dot{y} \tag{2.6}$$

The rate of momentum gain due to droplet drag, body forces and evaporation is:

$$\rho_g \mathbf{F}^s = -\int f\rho_l \left(\frac{4}{3}\pi r^3 \mathbf{F}' + 4\pi r^2 R \mathbf{U}_d\right) d\mathbf{U}_d \, dr \, dT_d \, dy \, d\dot{y} \tag{2.7}$$

And the energy transfer between gas and droplets related to evaporation, heat transfer into the droplet and work due to turbulent fluctuations is

$$\dot{Q}^s = -\int f\rho_l \left\{4\pi r^2 R \left[u_d + \frac{1}{2}(\mathbf{U}_d - \mathbf{U}_g)^2\right] + \frac{4}{3}\pi r^3 \left[c_{p,d}\dot{T}_d + \mathbf{F}'(\mathbf{U}_d - \mathbf{U}_g - \mathbf{U}'_g)\right]\right\} d\mathbf{U}_d \, dr \, dT_d \, dy \, d\dot{y} \tag{2.8}$$

The destruction of turbulent kinetic energy due to droplet dispersion is obtained by:

$$\dot{W}^s = -\int f\rho_l \frac{4}{3}\pi r^3 \mathbf{F}' \cdot \mathbf{U}'_g \, d\mathbf{U}_d \, dr \, dT_d \, dy \, d\dot{y} \tag{2.9}$$

In Eqs. 2.6 to 2.9 the superscript s indicates that the source terms are due to spray effects (as opposed to effects of chemical reactions that will be denoted by superscript c). $\mathbf{F}'$ is the difference between $\mathbf{F}$ and the gravitational acceleration $\mathbf{g}$, $(\mathbf{U}_d - \mathbf{U}_g)$ is the relative velocity between droplets and gas phase, and $\mathbf{U}'_g$ is the turbulent fluctuation of the gas velocity. Note, that in Eq. 2.8 u_d denotes the specific internal energy of the droplet and is not to be mistaken for the droplet velocity $\mathbf{U}_d$.

2.3.2 Numerical implementation

There are generally two possible ways of solving the spray equation in addition to the gas phase conservation equations. The obvious method would be to directly solve Eq. 2.5 with a Eulerian finite difference or finite volume scheme similar to the numerical solution of the gas phase. This method has been applied in ref. [11] and has been termed the continuum droplet model (CDM) in the literature [12]. However, the CDM requires to discretize the droplet probability function f in all eleven independent dimensions, and thus imposes extremely high demands with respect to computer memory and power. For example, discretizing the problem on a coarse mesh with only ten grid points in each dimension results in a total of 10^{11} grid points. For this reason the CDM has been proven impractical for most technical applications. An alternative and more practical approach is the so-called discrete droplet model (DDM) proposed by Dukowicz [13] and used in its original or similar forms in most CFD codes applied for engine spray and combustion simulations. It features a Monte-Carlo based solution technique for the spray equation, that describes the spray droplets by stochastic particles which are usually referred to as parcels [14].

These parcels can be viewed as representative classes of identical, non-interacting droplets, and they are tracked through physical space in a Lagrangian manner. The collection of such parcels within the computational domain represents a discretized solution of the spray distribution function, and thus, as the number of spray parcels in the spray are increased, the spray statistics are improved. It should be noted that while the spray parcels are usually viewed as groups of identical droplets, they are - in a strict mathematical sense - really statistical items describing the probability that the spray reacts in a certain way. The ostensive interpretation of droplet groups is probably due to the fact that due to available memory and CPU-power there are typically significantly fewer parcels considered than there are droplets in the spray (typically 10^3 to 10^4 parcels compared to about 10^8 droplets). However, the number of parcels necessary in order to obtain statistical significance is really independent of the number of droplets within the spray.

Account must be taken of the coupling between the Lagrangian liquid and the Eulerian gaseous phases in the DDM. While some codes utilizes the non-iterative Dukowicz method [13] where the drop motion equations are solved as functions of time, other spray codes are based on the so-called particle-source-in-cell (PSI Cell) technique proposed by Crowe et al. [15]. This technique begins by solving the gas flow field neglecting the presence of any spray particles in the flow. The obtained gas phase results are then used in order to calculate trajectories of the droplets as well as mass, momentum and energy exchanges between the two phases. Thereafter the gas phase is recalculated, now including the source terms caused by the spray particles, and the whole procedure is repeated in an iterative manner until a certain convergence criterion is met. Consequently, the PSI cell method is particularly suited for calculating steady-state spray processes, but it is not so well suited for modeling droplet dispersion in turbulent flows since these processes are inherently unsteady [6].

Besides its many obvious advantages it must be mentioned that a significant difficulty in modeling sprays with the stochastic particle method exists, in that there is typically a strong influence of the numerical grid design on the simulation results. Therefore a wide experience is often necessary in order to design a numerical mesh that is appropriate for a given spray problem. Finally, it should be noted that with both approaches of solving the spray equation, i.e. with the continuum droplet model as well as with DDM, the interface between a single droplet and the gas phase cannot be directly resolved because of computer limitations. Instead, an averaging of the flow process over a scale that is greater than the typical droplet diameter becomes necessary. Consequently, additional submodels are needed to describe the phase interactions at the droplet-gas interface. These submodels will be discussed in subsequent sections.

2.4 Droplet kinematics

In the Lagrangian formulation of the discrete droplet model the position of a drop or actually the position of a parcel containing a group of identical drops is characterized by the vector $\mathbf{P}$. The movement of the drop during one computational time step dt is derived from:

$$\frac{d}{dt}\mathbf{P} = \mathbf{U}_d \tag{2.10}$$

where the change in the drop velocity vector is determined from

$$\frac{d}{dt}\mathbf{U}_d = \mathbf{F} \tag{2.11}$$

The force $\mathbf{F}$ acting on the droplet is composed of body forces and the drag force caused by the relative velocity of the droplet to the surrounding gas phase. The latter force depends on the drop size and its drag coefficient (see Sect. 2.5) as well as on the mean gas velocity and its turbulent fluctuations (see Sect. 2.6). The change in drop size over time is given by

$$\frac{d}{dt}r_d = \dot{R} \tag{2.12}$$

where the quantity R depends on vaporization of the droplet (see Sect. ?ref?) and on breakup and collisions (Sects. ?ref? and ?ref?, respectively). The latter effects can lead to the change in the number of droplets in a specific size class and even to the appearance or disappearance of droplet classes from the computation. Thus, the number of parcels considered within a computation may change over time which can be expressed as

$$\frac{df}{dt} = \dot{f}_{cell} + \dot{f}_{bu} \tag{2.13}$$

2.5 Drop Drag and Deformation

The drag force acting upon a particle surrounded by gas of density ρ_g and velocity $\mathbf{U}_g$ can generally be expressed as

$$\rho_l V_d \mathbf{F} = \frac{1}{2}\rho_g C_D A_p \cdot |\mathbf{U}_g - \mathbf{U}_d| \cdot (\mathbf{U}_g - \mathbf{U}_d) \tag{2.14}$$

where A_p is the frontal area of the particle, i.e. ($A_p = \pi r_d^2$) for a spherical droplet. The drag coefficient C_D is a mostly empirically determined parameter that depends on the geometrical shape of the particle as well as on the flow conditions and gas properties. For low relative velocities (Re ≤ 1) around a spherical particle separation effects of the gas flow around the particle are negligible and the drag force is mainly due to friction drag by viscous stress. For this regime the drag coefficient is formulated by Stoke's law as

$$C_D = \frac{24}{\text{Re}} \tag{2.15}$$

where the Reynolds number is defined as

$$\text{Re} = \frac{2 r_d \rho_g \left| \mathbf{U}_g - \mathbf{U}_d \right|}{\mu_g} \tag{2.16}$$

For greater Reynolds numbers, and thus for greater relative velocities as they are typically encountered in engine sprays, the gas flow separates from the particle surface and form drag becomes increasingly more important than viscous drag. The drag coefficient of the sphere is amplified which is usually expressed by the following relations:

$$\begin{aligned} C_D &= \frac{24}{\text{Re}} \left(1 + \frac{1}{6} \text{Re}^{2/3} \right) && \text{Re} \leq 1000 \\ C_D &= 0.424 && \text{Re} > 1000 \end{aligned} \tag{2.17}$$

In order to account for thick spray effects that may increase the effective drag coefficient at positions close to the nozzle orifice, O'Rourke and Bracco [16] suggested to replace the first of the Eqs. 2.17 with a similar relation that additionally includes the local void fraction θ:

$$C_D = \frac{24}{\text{Re}} \left(\theta^{-2.65} + \frac{1}{6} \text{Re}^{2/3} \theta^{-1.78} \right) \text{Re} \leq 1000 \tag{2.18}$$

Eq. 2.18 was obtained from experiments on fluidized beds and other sources [9]. The above correlations for the drag coefficient are valid for ideally spherical (solid) particles. However, in engine sprays the liquid droplets are typically distorted from their ideal spherical shape prior to breakup. This will obviously have an effect on the drag coefficient which has been accounted for by Liu et al. [17], who applied the TAB model in order to determine the drop distortion parameter y. The TAB (Taylor-Analogy Breakup) model assumes a one-dimensional oscillation of the droplet in analogy to a spring-mass system. In this analogy the liquid viscosity acts as a damping element and the surface tension has the effect of a restoring force. The distortion parameter y is normalized by the droplet radius r and defined in accordance to Fig. 2.3.

The drag coefficient of the distorted droplet is now given as

$$C_D = C_{D,sphere} \left(1 + 2.632 y \right) \tag{2.19}$$

which is based on the consideration that for high Reynolds numbers the drag coefficient of a disc is approximately 3.6 times greater than that of a sphere.

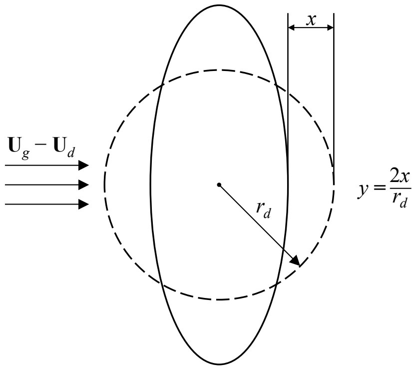

Figure 2.3: *Droplet distortion in the TAB model*

2.6 Turbulent Dispersion/Diffusion

In turbulent sprays the liquid droplets are not only decelerated and deformed by the gas phase, but an additional dispersion or diffusion of the liquid phase can be observed that is caused by the turbulent eddies in the gas flow. On average, the random orientation of the turbulent velocity fluctuations leads to a quicker, more homogeneous dispersion of the liquid droplets than in a laminar gas flow. At the same time the momentum transfer between gas and liquid modulates the turbulence level within the gas phase.

The mechanism can be explained following the schematic diagram in Fig. 2.4. It shows a vortex structure (solid line), i.e. the track of an arbitrary gas molecule within a turbulent gas flow, as well as three possible droplet trajectories (dashed lines) that start out at the same position as the gas molecule. Typically, a particle is assumed to interact with an eddy for a time period taken as the smaller of either the eddy lifetime t_e or the transit time t_t, required for the particle to pass through the eddy:

$$t_{int} = \min\left(t_e, t_t\right) \tag{2.20}$$

The characteristic eddy size is assumed to be the dissipation (integral) length scale

$$l_I = C_\mu^{3/4} \frac{k^{3/2}}{\varepsilon} \tag{2.21}$$

where the constant C_μ is the same as in the *k-epsilon* turbulence model ($C_\mu = 0.09$, see [18]). For isotropic turbulence the turbulent kinetic energy is related to the turbulence intensity by

$$k = \frac{1}{2}\left(U'^{\,2}_{g,x} + U'^{\,2}_{g,y} + U'^{\,2}_{g,z}\right) = \frac{3}{2} U'_g{}^{2} \tag{2.22}$$

and thus, the eddy life time is expressed as

$$t_e = \frac{l}{U'_g} = \frac{C_\mu^{3/4}}{\sqrt{2/3}} \cdot \frac{k}{\varepsilon} \tag{2.23}$$

The transit time can be estimated by linearizing the drop let momentum equations and is given by the expression

$$t_t = -\tau \ln \left[1 - \frac{l}{\tau \left| \mathbf{U}_g - \mathbf{U}_d \right|} \right] \tag{2.24}$$

The particle relaxation time τ is defined by the particle acceleration,

$$\frac{d\mathbf{U}_d}{dt} \equiv \frac{\mathbf{U}_g - \mathbf{U}_d}{\tau} \tag{2.25}$$

and can be derived from the particle's equation of motion, Eq. 2.14:

$$\rho_l V_d \frac{d\mathbf{U}_d}{dt} = \frac{1}{2} \rho_g C_D A_p \left(\mathbf{U}_g - \mathbf{U}_d \right)^2 \tag{2.26}$$

Thus, the relaxation time becomes

$$\tau = \frac{8}{3} \frac{\rho_l r_d}{\rho_g C_D \left| \mathbf{U}_g - \mathbf{U}_d \right|} \tag{2.27}$$

or, if Stoke's law is utilized for the drag coefficient, Eq. 2.15, we obtain

$$\tau = \frac{2}{9} \frac{\rho_l r_d^2}{\mu_g} \tag{2.28}$$

When $l \geq \tau \left| \mathbf{U}_g - \mathbf{U}_d \right|$, Eq. 2.24 has no solution. This can be interpreted as the eddy having captured a particle so that the interaction time becomes equal to the eddy life time t_e.

Crowe et al. [19] have observed that small drops in a turbulent flow tend to follow the gas flow, whereas the larger drops with their smaller drag/inertia ratios leave the large-scale vortex structures. A time-scaling ratio was proposed which, assuming Stokes drag for the particles, gives the Stoke's number:

$$\mathrm{St} = \frac{\tau}{t_e} \tag{2.29}$$

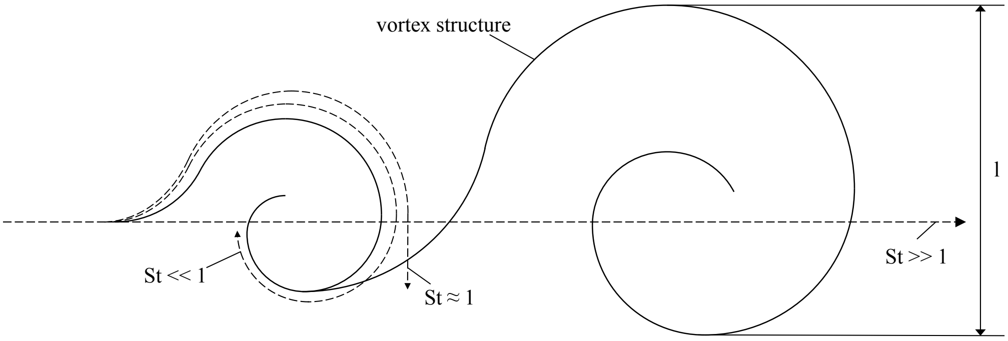

Figure 2.4: *Possible particle trajectories in a turbulent flow*

As depicted in Fig. 2.4, particles with Stoke's numbers much less than unity, i.e. small particles, are trapped within the eddies and directly follow the vortex structure. Particles with very large Stokes numbers remain unaffected by the eddies, and for Stoke's numbers in the order of unity a centrifuging effect may occur that leads to a particle dispersion which exceeds that of the gas phase. The numerical implementation of the above phenomena in CFD codes can be established by calculating the change in droplet motion for the interaction time period t_{int} as a function of the total gas velocity ($\mathbf{U}_g = \overline{\mathbf{U}}_g + \mathbf{U}'_g$) present at the beginning of the interaction. In order to yield a more realistic distribution of the turbulent dispersion effects, the fluctuating velocity component $\mathbf{U}'_g$ is typically sampled from a Gaussian distribution with a variance equal to the turbulence intensity $\left|\mathbf{U}'_g\right|$:

$$G(\mathbf{U}'_g) = \frac{1}{\sqrt{2\pi}\sqrt{2k/3}} \cdot \exp\left(-\frac{\left|\mathbf{U}'_g\right|^2}{4k/3}\right) \tag{2.30}$$

Experiments by Modarress and co-workers [20] on turbulent round jets revealed that the spread rates of two-phase jets are smaller than those of single-phase jets. Moreover, it was shown that the turbulence level within two-phase jets depends on the liquid mass loading: it decreases for greater amounts of liquid mass dispersed in the turbulent jet. These results indicate that the droplet turbulence interactions have a modulating influence on the gas phase turbulence. This is usually accounted for by adding the additional source term $\dot{W}^s$ in the k and ε conservation equations of the *k-epsilon* turbulence model. $\dot{W}^s$ has been specified in Eq. 2.9, and for incompressible turbulence in the absence of gradients the conservation equations become

$$\rho\frac{dk}{dt} = \dot{W}^s \tag{2.31}$$

$$\rho\frac{d\varepsilon}{dt} = C_s\frac{\varepsilon}{k}\dot{W}^s \tag{2.32}$$

It can be shown that the turbulence length scale l_I given in Eq. 2.21 is unchanged by this turbulence modulation if the empirical constant in Eq. 2.32 is chosen as $C_s = 3/2$ [6].

2.7 Spray Atomization

In engine fuel injection systems the fuel typically leaves the injector nozzle in a more or less continuous liquid phase that can obviously not be reproduced with the Lagrangian discrete droplet approach. Therefore, additional submodels are necessary in order to describe the breakup processes that lead to the formation of droplets, before the DDM can be applied. This procedure seems reasonable since in high pressure injection systems the disintegration of the continuous liquid phase into small droplets starts very close to the nozzle orifice. Thus, the impact of the intact liquid core on the gas phase is extremely small compared to the influence that the dispersed liquid droplets have on the gas phase in the entire spray.

Two different types of liquid breakup into ligaments and droplets are typically distinguished, e.g. [21]. The first kind of breakup occurs at or in direct vicinity of the injection nozzle orifice, i.e. in the region that has been scaled up in the bottom part of Fig. 2.1 and it is referred to as spray atomization or primary breakup. It describes the breakup of the intact liquid phase into first ligaments and droplets. Later on, the relatively large initial droplets can be further distorted and subsequently broken up into smaller secondary droplets. This kind of breakup is termed secondary breakup and will be discussed later. Typically, the secondary breakup takes place a little further downstream of the nozzle, i.e. within the thick, thin, and very thin spray regimes indicated in the schematic illustration of Fig. 2.1.

2.7.1 Breakup regimes

The primary breakup of liquid jets at the nozzle exit can be caused by a combination of three mechanisms: turbulence within the liquid phase, implosion of cavitation bubbles and aerodynamic forces acting on the liquid jet [22]. Due to the pressure drop across the injection nozzle the liquid fuel is accelerated within the small nozzle holes. Thereby a high level of turbulence is generated within the liquid phase that has a destabilizing effect on the jet once it exits the nozzle hole. Additionally, at sharp edges along the flow path inside the nozzle, e.g. at the inlet of the nozzle hole, the streamlines are contracted such that the effective cross-section the flow is reduced and its velocity is accelerated even more. According to Bernoulli's law this causes a reduction in the static pressure, and locally the static pressure may be decreased to a value as low as the vapor pressure of the fuel.

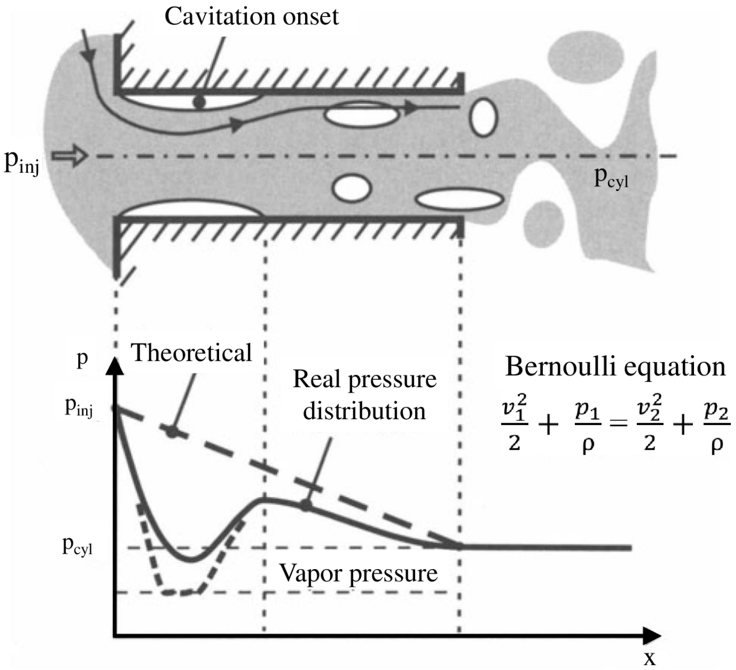

Figure 2.5: *Schematic illustration of cavitation formation inside the nozzle hole*

This phenomenon is schematically shown in Fig. 2.5, where the theoretical (linear) pressure distribution inside the nozzle hole is compared to a more realistic distribution along a streamline. The effect is that cavitation bubbles are generated inside the injection nozzle. This can be seen in Fig. 2.6 which shows an exemplary photograph of a cavitating flow through an acrylic glass nozzle. The cavitation bubbles are swept out of the nozzle into the combustion chamber where they implode and contribute to the disintegration of the spray. The third mechanism is that the relative velocity between the liquid jet and the gas results in aerodynamic forces that act on the liquid surface. Therefore, surface disturbances develop and start to grow that lead to breakup as well. Depending on injection parameters such as the relative velocity between liquid and gas, the liquid and gas densities and the liquid viscosity and surface tension, the relative contribution of each of the three above mechanisms to the spray breakup varies, and several different breakup modes can be identified. They are characterized mainly by different breakup lengths, i.e. the distance between the nozzle orifice and the breakup position, and by the sizes of the resulting droplets.

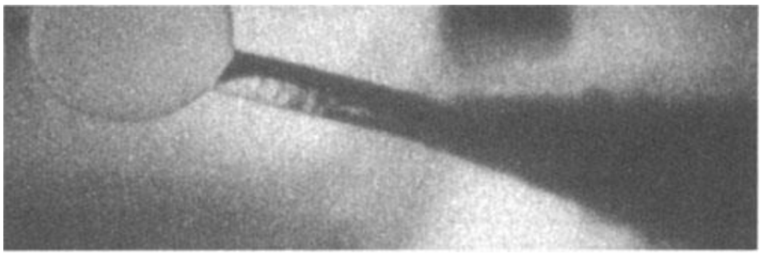

Figure 2.6: *Cavitation inside an acrylic glass diesel injection nozzle. The liquid phase is transparent, the gas phase is opaque.* $p_{inj} = 65$ MPa, $p_{cyl} = 0.1$ MPa , $d_{noz} = 0.22$ mm [2]

A widely agreed classification of breakup regimes has been proposed by Reitz and Bracco [23] in terms of the above injection parameters and fluid properties. For general applicability those quantities are expressed through the dimensionless Reynolds, Weber and Ohnesorge numbers, defined respectively as

$$\mathrm{Re} = \frac{\rho U_{\mathrm{inj}} d_{\mathrm{noz}}}{\mu} \tag{2.33}$$

$$\mathrm{We} = \frac{\rho U_{\mathrm{inj}}^2 d_{\mathrm{noz}}}{\sigma} \tag{2.34}$$

$$\mathrm{Z} = \frac{\mu}{\sqrt{\rho \sigma d_{\mathrm{noz}}}} \tag{2.35}$$

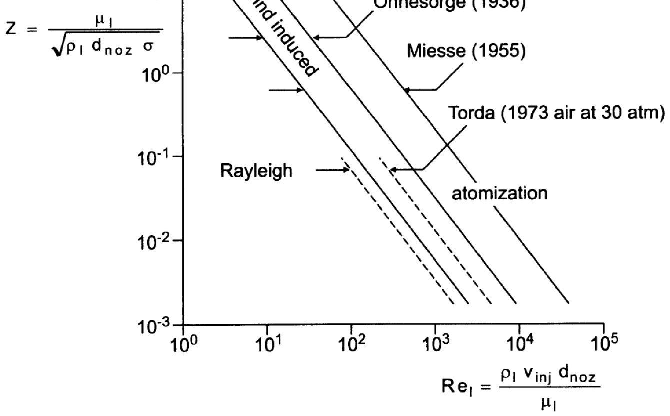

Figure 2.7: *Jet breakup regime boundaries by Miesse* [3] *and Ohnesorge* [4]

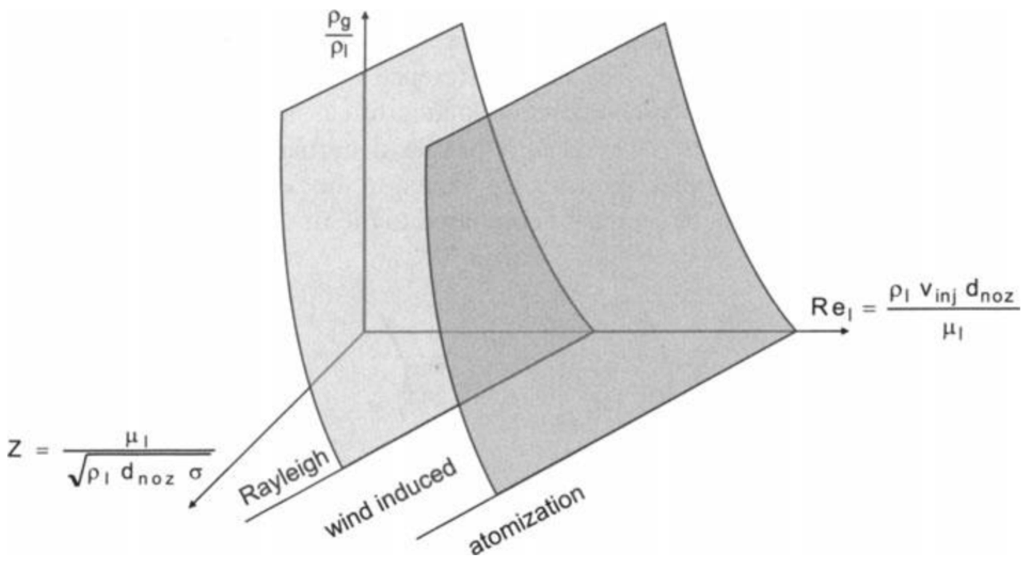

Figure 2.8: *Schematic chart of influence of gas density on breakup regime boundaries* [5]

Four different spray regimes are typically distinguished, the Rayleigh, first wind induced, second wind induced and the atomization regime. Ohnesorge [4] and Miesse [3] suggested a definition by the liquid Reynolds and Ohnesorge numbers, i.e. the liquid phase properties are used in Eqs. 2.33 and 2.35. Fig. 2.7 displays the results in which the first and second wind induced regimes have been combined. However, the definition in terms of the liquid properties implies that the effect of the gas phase on breakup is not taken into account in the classification, which is in contrast to the observation that the atomization can be enhanced by increasing the gas density (pressure) [24]. Therefore, Ranz [25] proposed a breakup classification in terms of the gas phase Weber number, which is based on the density of the gas phase ρ_g and the surface tension of the liquid σ_l. This approach however is incomplete as well, since now the influence of the liquid viscosity on breakup is neglected. In order to overcome these limitations Reitz [5] suggested to include the gaseous to liquid density ratio in the analysis, such that the two-dimensional plot in Fig. 2.7 now becomes a three-dimensional one as depicted in Fig. 2.8.

Fig. 2.9 shows a schematic illustration of jet breakup in the characteristic breakup regimes. For relatively low injection velocities the Rayleigh breakup (a) is primarily governed by the inertia forces on the oscillating liquid and by its surface tension. The breakup length is far (many nozzle diameters) downstream of the nozzle orifice and the diameter of the resulting droplets is greater than the nozzle diameter.

In the first wind induced breakup regime (b) the inertia of the gas phase becomes more and more important. Surface disturbances are caused by the gas-liquid interactions that increase in amplitude and eventually lead to breakup. The average drop size decreases and is now in the range of the nozzle diameter. The breakup length is still a multiple of the nozzle diameter. For further increased injection velocities the second wind induced regime is reached. In Fig. 2.9 it has been combined with the first wind induced regime since the basic mechanisms leading to breakup are similar. The main difference is that as the relative velocity between liquid and gas increases, the aerodynamic forces acting on the liquid surface are intensified and the wavelength of the disturbances becomes shorter. Therefore, the average droplet diameter is reduced in the second wind induced regime and the breakup length decreases compared to the first wind induced regime.

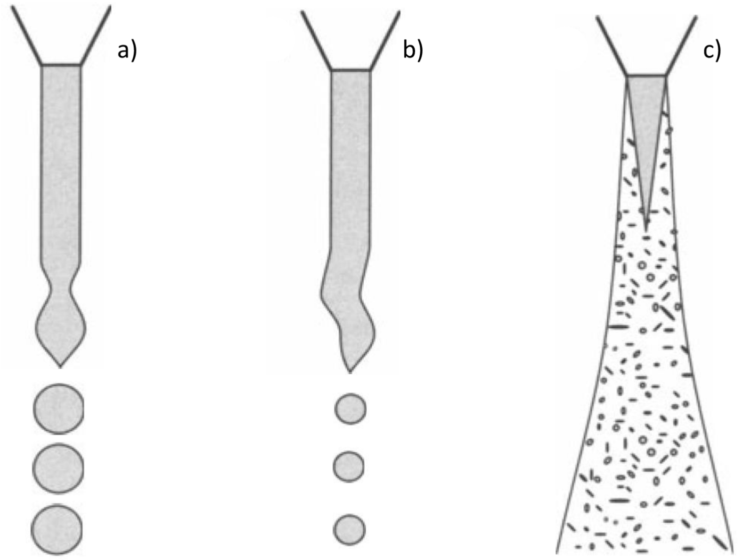

Figure 2.9: *Schematic depiction of breakup modes. a) Rayleigh b) Wind induced c) Atomization*

Finally, for increased gas densities and large injection velocities the gas phase Weber number increases further and the atomization regime is reached (c). In this regime two different breakup lengths can be identified: the surface breakup begins directly at the nozzle orifice whereas an intact core may still be present several nozzle diameters downstream of the orifice. Furthermore, a conical shape of the overall spray is now observed. The mean droplet diameters are much smaller than the nozzle diameter.

The atomization regime is the most important for high pressure diesel injectors. However, a detailed experimental assessment of the primary spray breakup directly at the nozzle is extremely difficult because the spray is very dense and almost opaque at this position. Therefore, the detailed mechanisms that lead to primary spray breakup or atomization at the nozzle of modern diesel engine injection systems with injection pressures of up to 200 MPa are still not exactly understood. However, there is a general agreement that as the injection pressure increases, the effects of the inner nozzle flow such as the liquid phase turbulence and cavitation become more and more important.

2.7.2 Wave-Breakup Model

It has been discussed above that the development and aerodynamically driven growth of surface disturbances on the liquid phase is an important if not the dominant mechanism for breakup of jets. Vital contributions to deriving the theory behind this phenomenon and to establishing a coherent and continuous breakup model have been made by Reitz and co-workers, e.g. [5,23,26]. Since this so called wave-breakup model (also referred to as Kelvin-Helmholtz breakup model) is widely applied in primary as well as in secondary breakup models it will be summarized here.

The analysis starts out from a cylindrical liquid jet of radius a that penetrates through a circular orifice into a stationary incompressible gas environment, Fig. 2.10. The liquid surface is subject to a number of infinitesimal perturbations with an initial amplitude of η_0 and a spectrum of wavelengths λ typically expressed through the wave number $k = 2\pi/\lambda,$. The initial disturbances may be caused by effects of the inner nozzle flow, e.g. by turbulence within the liquid phase. Their amplitudes will be increased exponentially by the liquid-gas interactions with a complex growth rate of $\omega = \omega_r + i\omega_i$:

$$\eta_t = \mathrm{R}\left(\eta_0 \mathrm{exp}\left[ikx + \omega t\right]\right) \tag{2.36}$$

Assuming that the gas phase behaves as an inviscid fluid, i.e. there is free slip at the liquid-gas interface, and that the perturbations are much smaller than the jet radius ($\eta << a$) the so-called dispersion relation can be derived, that relates the growth rate ω to the wave number k [26]:

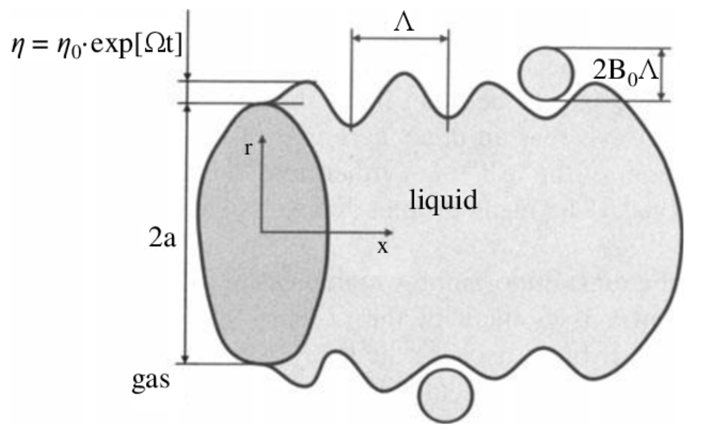

Figure 2.10: *Schematic growth of surface perturbations in the Wave-breakup model* [6]

$$\begin{aligned}\omega^2 + 2\nu_l k^2 \omega \left[\frac{I_1'(ka)}{I_0(ka)} - \frac{2kl}{k^2+l^2}\frac{I_1(ka)}{I_0(ka)}\frac{I_1'(la)}{I_1(la)}\right] &= \frac{\sigma k}{\rho_l a^2}\left(1-k^2a^2\right) \\ \cdot\left(\frac{l^2-k^2}{l^2+k^2}\right)\frac{I_1(ka)}{I_0(ka)} + \frac{\rho_g}{\rho_l}\left(U_g - \frac{i\omega}{k}\right)^2 k^2 &\left(\frac{l^2-k^2}{l^2+k^2}\right)\frac{I_1(ka)\cdot K_0(ka)}{I_0(ka)\cdot K_1(ka)}\end{aligned} \tag{2.37}$$

In the above equation I_n and K_n are the n^{th} order modified Bessel functions of the first and second kind, respectively. The prime indicates differentiation, ν_l is the kinematic viscosity of the liquid phase while U_g is the gas velocity at the liquid-gas interface, and $l^2 = k^2 + \omega/\nu_l$.

Even though the perturbations of different wave lengths will superpose each other in the real jet, it is assumed that only the fastest growing perturbation, indicated by growth rate Ω, that corresponds to the wave length Λ will ultimately lead to breakup. However, Eq. 2.37 is difficult to solve for a maximum value of ω since l is still a function of ω. To simplify the problem, Reitz [7] generated curve-fits of numerical solutions to Eq. 2.37 and obtained the following expressions for the maximum growth rate Ω and its corresponding wave length Λ:

$$\frac{\Lambda}{a} = 9.02\frac{(1+0.45\sqrt{\mathrm{Z}})(1+0.4\mathrm{Ta}^{0.7})}{(1+0.865\mathrm{We}_g^{1.67})^{0.6}} \tag{2.38}$$

$$\Omega\sqrt{\frac{\rho_l a^3}{\sigma}} = \frac{0.34+0.38\mathrm{We}_g^{1.5}}{(1+\mathrm{Z})(1+1.4\mathrm{Ta}^{0.6})} \tag{2.39}$$

where $\mathrm{Z} = \frac{\sqrt{\mathrm{We}_l}}{\mathrm{Re}_l}$, $\mathrm{Ta} = \mathrm{Z}\sqrt{\mathrm{We}_l}$, $\mathrm{We}_l = \frac{\rho_l U_g^2 a}{\sigma}$, $\mathrm{We}_g = \frac{\rho_g U_g^2 a}{\sigma}$, $\mathrm{Re}_l = \frac{U_g a}{\nu_l}$

The above relations have the effect that the growth rate increases and the corresponding wavelength decreases for increasing gas Weber numbers. This is in agreement with the experimental observation that for increasing injection velocities, breakup is enhanced while the average diameters of the resulting droplets become smaller. The effect of liquid viscosity which appears in the Reynolds number Re and thus in the Ohnesorge number Z is that the wave growth rate is reduced.

In order to estimate the sizes of droplets formed by breakup, it is often assumed that there is a linear dependency between the resulting droplet radius r_d and the wave length Λ of the most unstable surface disturbance, e.g. [7],

$$r_d = \mathrm{B}_0\Lambda \tag{2.40}$$

where B_0 is of order of unity. The length of the "intact" liquid core of the spray may be approximated by considerations of the mass removed from the jet by the atomization process,

$$L = \frac{ca}{f(\mathrm{Ta})}\sqrt{\frac{\rho_l}{\rho_g}} \tag{2.41}$$

where Ta is defined as in Eqs. 2.38 and 2.39, and $f(\mathrm{Ta})$ asymptotically approaches $(3^{0.5}/6)$ for $(\mathrm{Ta} > 100)$, which is typically satisfied in diesel sprays. The constant c ranges from about 15 to 30 and accounts for various effects of the inner nozzle flow that are not resolved in detail.

The half-angle $(\alpha/2)$ of the cone shaped spray observed in the atomization regime of high speed jets has been specified in ref. [23] based on the assumption that the droplet velocity component perpendicular to the spray direction $v_\perp$ is proportional to the wave growth rate of the most unstable wave:

$$\tan\left(\frac{\alpha}{2}\right) = \frac{v_\perp}{|\mathbf{U}_d|} = \frac{\Omega\Lambda}{A|\mathbf{U}_d|} = \frac{4\pi}{A}\sqrt{\frac{\rho_g}{\rho_l}}f(\mathrm{Ta}) \tag{2.42}$$

The expression $f(\mathrm{Ta})$ is the same as in Eq. 2.41, and the constant A accounts for the nozzle geometry. In ref. [6] it has been defined in terms of the length to diameter ratio of the nozzle hole as

$$A = 3.0 + \frac{l_{noz}/d_{noz}}{3.6} \tag{2.43}$$

2.7.3 Blob-Injection Model

Reitz [7] applied the above Wave-breakup model to high speed diesel jets by assuming that during the injection duration there are continuously added large drops (so-called blobs) with a diameter comparable to the size of the nozzle hole to the gas phase. The frequency of the addition of new blobs is related to the fuel injection rate in a straightforward manner, assuming constant density of the liquid fuel and ideally spherical blobs. Immediately after injection the Kelvin-Helmholtz instabilities described by the wave-model start to grow on the blob surface, such that sm all secondary droplets are "sheared off" the blob surface as shown in Fig. 2.11.

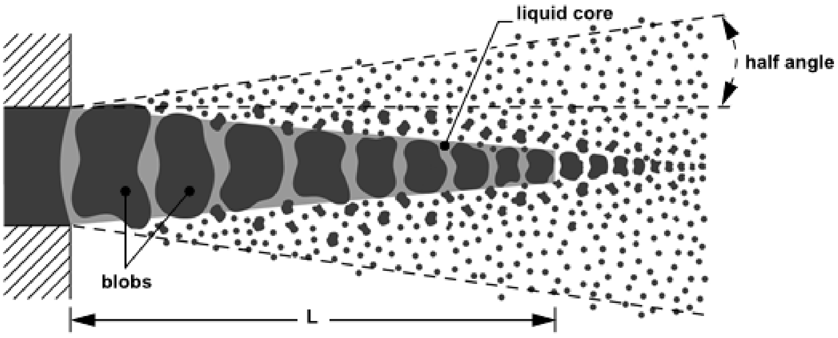

Figure 2.11: *Schematic illustration of the blob-injection model* [7]

The calculation of the fastest growing wave length Λ and its corresponding growth rate Ω is executed in analogy to Eqs. 2.36 to 2.39. In ref. [7] the relation

$$r_d = B_0 \Lambda \tag{2.44}$$

was suggested to estimate the resulting droplet radii with a value of $B_0 = 0.61$ in the stripping breakup regime. For higher injection velocities and catastrophic breakup in the atomization regime, which is typical for diesel type injectors, Liu et al. [27] proposed the formulation

$$B_0 = 0.3 + 0.6P \tag{2.45}$$

where P is a random number within the interval between zero and one. By this method a distribution of droplet sizes is obtained which is more realistic for breakup of high speed jets. In both cases a bi-modal droplet size distribution is obtained for the complete spray, consisting of a number of larger droplets remaining from the original jet and a number of small drop lets resulting from the above Kelvin-Helmholtz breakup.

Eqs. 2.44 and 2.45 may be used only if the resulting droplet diameter is less than the radius of the remaining parent drop, i.e. if $(B_0\Lambda \leq a)$. Otherwise, the resulting radius of the newly formed droplet is estimated by

$$r_{d,new} = \min \begin{cases} \sqrt[3]{3\pi a^2 \dfrac{\mathbf{U}_{rel}}{2\Omega}} \\ \sqrt[3]{3a^2 \dfrac{\Lambda}{4}} \end{cases} \quad ((B_0\Lambda > a, \text{one time only}) \tag{2.46}$$

which is based on the assumption that the jet disturbance has a frequency of $\Omega/2\pi$, i.e. one drop is formed each wave period, or that the drop size is determined from the volume of liquid contained under one surface wave.

Due to the breakup and generation of new small droplets, the size of the original blob is reduced. The temporal change in radius of this parent drop is given by

$$\frac{da}{dt} = -\frac{a - r_d}{\tau} \tag{2.47}$$

where τ is the breakup time:

$$\tau = 3.788 B_1 \frac{a}{\Lambda\Omega} \tag{2.48}$$

The constant B_1 has been introduced in order to account for effects of the inner nozzle flow on the breakup time that cannot be resolved directly. In ref. [7] a value of $B_1 = 20$ has been suggested whereas other references reported better results with values ranging from 1.73 [28] up to 30 [29]. This suggests that the inner nozzle flow has indeed an influence on primary spray breakup in addition to the liquid-gas interactions that is not yet included in the breakup analysis.

In order to reproduce the spray cone angle observed in diesel type sprays the child droplets separated from the initial blobs are equipped with a velocity component perpendicular to the main spray orientation. The maximum possible value of this component is obtained from the spray half angle specified in Eq. 2.42, and Reitz [7] suggests to choose an even distribution between zero and the maximum normal velocity for the various droplets in order to achieve a realistic droplet density within the spray.

In many recent applications of the blob injection method the above Wave- or Kelvin-Helmholtz breakup model has been combined with the so-called Rayleigh-Taylor model in order to estimate the disintegration of the blobs into secondary droplets. The Rayleigh-Taylor model describes the instabilities that develop on a liquid-gas interface subject to strong normal accelerations pointed towards the gas phase. However, the disintegration of large drops into small droplets is considered a secondary breakup mechanism and therefore the Rayleigh-Taylor breakup will be discussed in the next section.

It should be noted here, that the Kelvin-Helmholtz mechanism may be viewed as a secondary breakup mechanism as well, since it describes the breakup of large drops or blobs into smaller droplets. In fact, the model is used not only to estimate the disintegration of primary blobs but also to model the subsequent breakup of secondary droplets into even smaller droplets.

2.8 Secondary Droplet Breakup

2.8.1 Drop Breakup Regimes

The secondary breakup of liquid fuel drops into even smaller droplets is primarily driven by aerodynamic forces employed on the drops by the surrounding gas phase. These forces cause a distortion of the initially spherical droplet that will eventually lead to breakup if the surface tension that counteracts the deformation is exceeded. Consequently, the dimensionless droplet Weber number, which relates the dynamic pressure to the surface tension and is defined as

$$\mathrm{We} = \frac{\rho_g r_d v_{rel}^2}{\sigma}, \tag{2.49}$$

is a characteristic measure of the breakup behavior of liquid droplets. Depending on the relative velocity between droplet and gas phase, and thus depending on the Weber number, several different breakup mechanisms have been observed in experimental studies. Often the five different breakup regimes schematically shown in Fig. 5.24 are distinguished.

For very low Weber numbers near the critical value of about six, the droplet executes an oscillation and may breakup into two new droplets of approximately equal size. If the Weber number is slightly increased, the original drop will be deformed into a bag shape. After breakup a bimodal droplet size distribution will result with larger droplets originating from the rim and smaller ones originating from the trailing edge. For Weber numbers between approximately 10 and 25 an additional streamer-shaped interior may develop within the bag, leading to a class of droplets with a similar size to the ones resulting from the rim of the bag. Stripping breakup occurs for Weber numbers between 25 and 50. It is characterized by very small secondary droplets that are stripped or sheared off the surface of the bigger parent droplet. Finally, for large Weber numbers above about 50 the so-called catastrophic breakup takes place. It is dominated by surface instabilities that develop on a liquid-gas interface subject to strong accelerations in a direction normal to the interface. It should be noted though that there is some uncertainty about the limiting Weber numbers, especially towards the high-end of Weber numbers between the stripping and catastrophic regimes. For example, Arcoumanis et al. [22] distinguish two different kinds of stripping breakup, namely the sheet stripping and the wave crest stripping regimes, and extend their applicability to significantly greater Weber numbers such that catastrophic breakup does not occur until a value of We ≈ 500 is exceeded.

In high pressure diesel or gasoline sprays all of the above mechanisms may be present. Starting close to the injector orifice the relative velocity between droplets and gas as well as the Weber number are very large, such that catastrophic breakup is the dominant mechanism. However, further downstream of the nozzle droplets with significantly smaller Weber numbers may be present because of both lower relative velocities and smaller diameters resulting from previous breakup and evaporation.

A variety of mathematical models for drop breakup have been proposed in the literature. Most of these models have been established in order to describe one particular of the five breakup mechanisms. Nevertheless, in engine spray simulations they are - for the sake of simplicity - often applied to the entire spectrum of breakup regimes. This is not entirely true though. In recent years it has become more and more standard to determine the goveming breakup mechanism for a droplet class and then apply the more appropriate of at least two breakup models, e.g. a combination of the Kelvin-Helmholtz and the Rayleigh-Taylor model.

In the subsequent sections among the secondary breakup models that are applied most often in engine spray simulations only the KH-RT will be discussed.

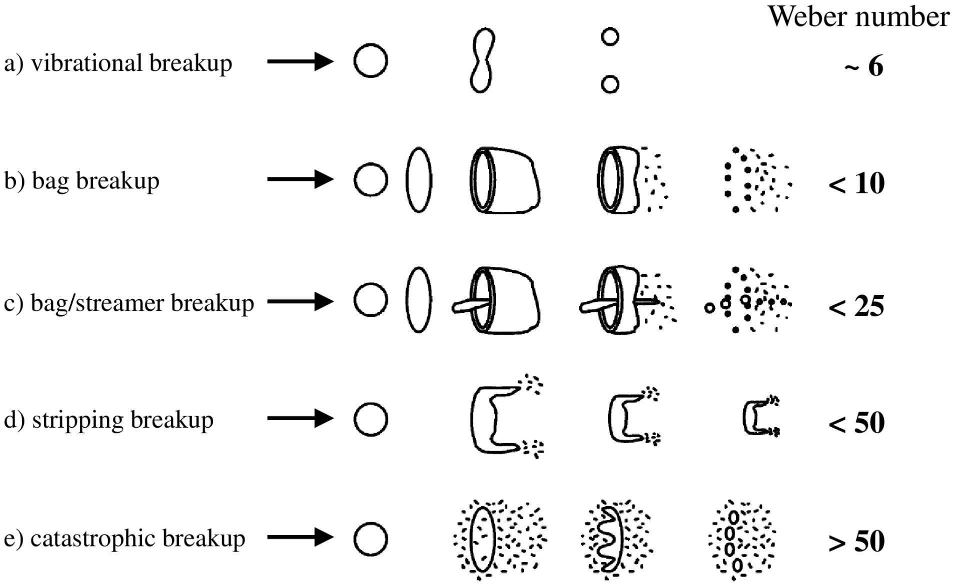

Figure 2.12: *Drop breakup regimes* [8]

2.8.2 The Kelvin-Helmholtz Breakup Model

Reitz [7] has shown that the wave-breakup theory describing the development of Kelvin-Helmholtz (KH) instabilities on a jet surface can be also be applied to model the secondary breakup of droplets, see Sects. 2.7.2 and 2.7.3. The complete formulation has already been given above and, as already discussed, there is considerable uncertainty about the value of B_1. In the literature values ranging from 1.73 up to 30 have been used, and in ref. [6] it was pointed out that B_1 may need to be adjusted to different initial disturbance levels of the droplet. Another aspect worth of mention is related to the fact that the numerical implementation of the KH breakup mechanism results in a bimodal droplet size distribution with small droplets that are sheared off the surface of the parent droplets and larger droplets remaining from the original parent droplet. This effect is always implemented into the numerical scheme of the CFD code by generating additional droplet parcels after breakup.

2.8.3 The Rayleigh-Taylor Breakup Model

The Rayleigh-Taylor (RT) breakup model is based on theoretical considerations of Taylor [30], who investigated the stability of liquid-gas interfaces when accelerated in a normal direction to the plane. Generally, it can be observed that the interface is stable when acceleration and density gradient point to the same direction, whereas Rayleigh-Taylor instabilities can develop if the fluid acceleration has an opposite direction to the density gradient. For a liquid droplet decelerated by drag forces in a gas phase this means that instabilities may grow unstable at the trailing edge of the droplet as schematized in Fig. 2.13.

The acceleration (or deceleration) of a droplet is due to drag forces and follows from Eq. 2.14,

$$\mathbf{F} = \frac{3}{8} C_d \frac{\rho_g}{\rho_l} \frac{|\mathbf{U}_{rel}|^2}{r_d} \tag{2.50}$$

where $\mathbf{U}_{rel}$ is the relative velocity between droplet and gas, and r_d is the droplet radius. Based on the assumption of linearized disturbance growth rates and negligible viscosity the frequency and wavelength of the fastest growing waves are

$$\Omega = \sqrt{\frac{2}{3\sqrt{3\sigma}} \frac{[|\mathbf{F}|(\rho_l - \rho_g)]^{3/2}}{\rho_l + \rho_g}} \tag{2.51}$$

and

$$\Lambda = 2\pi \sqrt{\frac{3\sigma}{|\mathbf{F}|(\rho_l - \rho_g)}} \tag{2.52}$$

respectively [31]. In many applications of the RT-breakup model the gas density is neglected in the above equations because it is significantly smaller than that of the liquid. It is apparent from Eq. 2.51 that the acceleration is the prime factor causing a rapid growth of Rayleigh-Taylor instabilities, whereas the surface tension counteracts the breakup mechanism.

The breakup time is found as the reciprocal of the frequency of the fastest growing wave:

$$t_{bu} = \Omega^{-1} \tag{2.53}$$

Furthermore, the size of the new child drop lets is calculated in dependence of the RT-wavelength A, and breakup is only allowed when A is less than the diameter of the parent droplet [29]. In ref. [32] the number of new droplets is determined as the ratio of the maximum diameter of the deformed parent droplet to Λ, and the corresponding diameter of the child droplets is obtained from mass conservation principles.

Typically, the Rayleigh-Taylor breakup model is not applied as the only method to describe secondary droplet breakup, but it is rather used in combination with an additional breakup model, most often with the Kelvin-Helmholtz model describing stripping breakup. In that case the RT- and KH-models are implemented in a competing manner, i.e. the droplet breaks up by the mechanism that predicts a shorter breakup time. Close to the injector nozzle where the droplet velocities are highest, the RT-breakup is usually the governing mechanism, whereas the KH-breakup becomes more dominant further downstream.

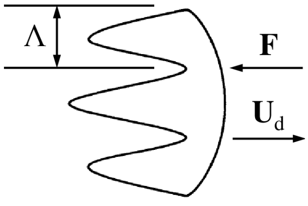

Figure 2.13: *Schematic illustration of Rayleigh-Taylor instabilities on a liquid droplet*

However, one more constraint exists in most applications. In order to be able to reproduce experimentally obtained intact core or breakup lengths, e.g. given by the relation

$$L_{bu} = C_{bu} d_{noz} \sqrt{\frac{\rho_l}{\rho_g}} \tag{2.54}$$

the RT-breakup model that would predict extremely rapid breakup directly at the nozzle exit is switched off within this breakup length [33].

Since the RT-breakup model predicts the disintegration of a parent droplet into a number of equally sized child droplets, the combination of the RT- and KH-breakup models counteracts the formation of sprays with a distinct bimodal droplet size distribution as they will be predicted if the KH-model is applied as the only mechanism of secondary droplet breakup.

2.9 Fuel Evaporation

Fuel evaporation is a process of great importance especially in direct injection engines. It has a direct effect on the combustion rate since only vaporized fuel that has been mixed with air in a combustible ratio can chemically react with the oxygen contained in the fresh intake air. Thus, an engine's thermodynamic efficiency is affected by the evaporation rate. And moreover, the fuel evaporation can have a significant influence on the emission formation as well. Poor evaporation will typically cause increased soot and unburned hydrocarbon emissions, while very rapid evaporation, especially during the ignition delay in diesel engines, will cause an increase in nitrogen oxides because of rapid premixed combustion associated with high temperatures. Consequently, a thorough understanding of the dominating processes in fuel vaporization is a prerequisite in order to assess the overall quality of mixture formation and spray combustion. In direct injection engines the major fraction of the fuel mass evaporates after the spray has broken up into small droplets. This is because the liquid fuel is typically below its boiling temperature when it exits the injection nozzle and its specific surface area is very small prior to atomization. Therefore, droplet evaporation is the most important part in evaporation modeling. However, under certain boundary conditions additional evaporation mechanisms such as wall film evaporation, e.g. after spray wall impingement, or flash boiling, e.g. for volatile fuels, may become important, too.

2.9.1 Droplet Evaporation

Droplet evaporation is governed by conductive, convective and radiative heat transfer from the hot gas to the colder droplet and by simultaneous diffusive and convective mass transfer of fuel vapor from the boundary layer at the drop surface into the gas environment. However, it is not feasible to directly resolve the flow field in and around the many droplets of a complete spray due to constraints with respect to computer power and memory. Therefore, in engine applications it is most often assumed that the droplets are ideally spherical and averaged flow conditions and transfer coefficients around the droplets are determined. Moreover, the radiative heat transfer between gas and drops is typically neglected as it is small compared to convection.

Nevertheless, several additional effects on droplet vaporization have been investigated in detail by various researchers. In ref. [34] it was shown that vaporization reduces both the heat transfer rate to the droplet and its drag coefficient. However, as reported in ref. [6] numerical studies performed with the CFD-code KIVA suggested that this effect is relatively small for diesel-type sprays.

Taking into account that the fuel drops are significantly distorted during the majority of their lifetime in diesel sprays, Gavaises and co-workers [22, 35] investigated the effect of non-spherical droplets on the fuel evaporation rate. They evaluated not only the drag coefficient as a function of this phenomenon but also accounted for a modification in the exchange area between drop and gas by assuming that the distorted drop becomes a spheroid that can be characterized by the maximum and minimum diameters calculated from the breakup model. Accordingly, more detailed correlations derived from heat transfer studies on spheroids were used to estimate the dimensionless Nusselt and Sherwood. The reported results indicate that the consideration of droplet deformation effects yields an increased overall evaporation rate for complete sprays. Thus, there is an influence on the spatial equivalence ratio distribution, and ignition timings and locations are likely to be affected as well.

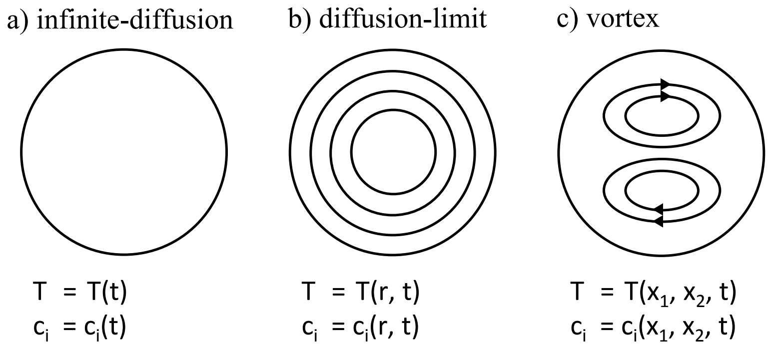

Figure 2.14: *Modeling approaches for the droplet interior*

The above droplet evaporation models are all based on the lumped capacitance method, i.e. the temperature within the droplet is assumed to be spatially uniform and depends on time only. A measure whether this assumption is valid is given by the Biot number which relates the resistance to heat conduction within the droplet to the resistance to heat convection from the gas to the droplet, see e.g. [36]:

$$\mathrm{Bi} = \frac{R_{cond}}{R_{conv}} = \frac{h r_d}{k_l} \tag{2.55}$$

For Biot numbers much less than unity the assumption of a uniform temperature within the droplet is justified. However, this may not always be the case in engine sprays as has been shown by several authors who investigated the evaporation process including the spatial and temporal evolutions of the droplet interior under Diesel like conditions, e.g. [37–39]. However, these sophisticated evaporation models that account for two- or even three-dimensional flows within the droplet interior are limited to studies of isolated droplets or simple arrays of droplets and cannot be used in complete spray simulations because of computer limitations. For this purpose three different degrees of simplification have been proposed and examined in the literature, Fig. 2.14.

Besides the simplest *infinite-diffusion* model, that is based on the lumped capacitance method and assumes a well-mixed droplet interior without spatial gradients at any time, the so-called *diffusion-limit* model has been proposed. It assumes a one-dimensional temperature and, in the case of a multicomponent fuel, mass distribution as a function of the drop let radius. The heat and mass exchange processes inside the droplet are governed by conduction and diffusion, respectively, and are solved on a one-dimensional numerical grid of concentric shells. The most comprehensive of the simplified models is the *vortex model*. It considers an inviscid liquid flow region inside the droplet that is assumed to be given by Hill's vortex.

Aggarwal [40] compared the three above droplet models for varying boundary conditions and observed that the infinite-diffusion model yields results that are markedly different from the two more complex models. This is especially the case for multicomponent fuel mixtures where the species concentrations of the more and less volatile compounds in the vapor phase are significantly over-predicted and under-predicted, respectively. The diffusion-limit and the vortex models were found to produce remarkably similar results under most conditions and thus, the use of the diffusion-limit model is recommended as it is easier to handle and computationally more efficient.

It should be noted though, that the simple droplet evaporation model that assumes a spherical, well-mixed droplet and is based on a single-component fuel, can still be viewed as the standard in today's engine spray simulations. This is mainly due to its simplicity and because of computing time requirements. Nevertheless, the number of numerical studies including more comprehensive evaporation models is steadily increasing. The focus has especially shifted towards a more realistic description of real diesel and gasoline fuels that can hardly be characterized by a single-component model fuel since they are a mixture of several hundred different hydrocarbon components.

CHAPTER 3

Spherical Volume Interaction DDM

3.1 Introduction

Fuel-air mixing, combustion and pollutant formation in Diesel Engines are strictly influenced by how the introduction of the liquid fuel and the interaction of it with the physical domain take place. Accurate prediction of these processes is fundamental to meet more and more stringent emission regulations and to improve the engine performance.

As it happens for every other physical phenomena, numerical description of Diesel sprays should rely on spatial and temporal averaging and discretization procedures of the relevant differential equations.

Different approaches were proposed in the past with the aim to correctly describe the liquid-gas interaction. As already pointed out in Chap. 2, the Discrete Droplet Modeling (DDM) described by Dukowicz [13] is perhaps the most widely adopted method applied to Diesel spray modeling in the last three decades. This approach consists of a fully-interacting combination of Eulerian fluid and Lagrangian particle calculations and presents at the same time well-known advantages and drawbacks. Among the upsides of this approach, a Lagrangian description of the particles avoids numerical diffusion, and allows individual attributes, such as particle size, composition, etc., to be statistically assigned for each particle. It is also notable that this approach relies on strong basic assumptions such as low liquid volume fraction and homogeneously distributed parcels in the computational cells that are usually not satisfied in the near nozzle region. To partially overcome these issues and to assure numerical stability, it is often necessary to adopt minimum cell sizes larger than the nozzle diameter. This choice may cause an inadequate resolution of the flow structures. Moreover, even when the basic hypothesis are fulfilled, results show strong dependencies on the choice of the grid structure and on the mutual orientation of the spray trajectory with respect to the grid [41, 42]. This makes hard to define a best practice that is independent of the used grid to discretize the physical domain. It becomes even harder in light of the fact that, with the aim to automate more and more CFD calculations, most of the software are lately adopting automatic mesh generation that often produce Cartesian grids. These meshes are mainly characterized by a well organized structure made of hexahedral elements arranged along a Cartesian system of axes. Such a structure is therefore basically independent on the geometry of the physical domain. The present study focuses particularly on the effect that the choice of this grid structure can have if evaluated on varying the injector nozzle position with respect to the cell hosting it.

In DDM approach every parcel injected in the domain represents a statistical entity occupying a precise position at any given time and is characterized by any significant physical quantity considered useful to the analysis. The parcel evolves with time interacting with the surrounding environment that, according to the standard DDM approach, coincides with the cell hosting the parcel in the given time. As briefly outlined before, this approach shows grid dependencies on the mesh structure and size which cannot be neglected. Moreover if the mesh is Cartesian and the injection direction is aligned with one of the main directions of the grid elements, these dependencies are also related to the position of the injector nozzle within the cell hosting it. This study shows that high uncertainties are introduced even only by gradually moving the injector from the center of the cell to one of the vertexes. Keeping everything constant but the point from which the liquid is injected, affects the way mass, momentum and energy are transferred from the Lagrangian phase to the Eulerian domain and different liquid length and jet penetration, as well as mixture fraction and velocity distribution have been calculated and pointed out.

In this chapter an implementation of a different approach based on a spherical volume which acts as intermediary between the Lagrangian and Eulerian phases is proposed. The aim of the work is to evaluate the application of this approach to Diesel spray modeling by simultaneously comparing it with standard DDM approach and experimental data. These measurements data were taken from the ECN web database [43] and include all the parameters listed before.

A sensitivity analysis is finally included to test the robustness of the new approach keeping constant every tunable parameter of the included sub-models (evaporation, turbulence, break-up models, etc.). This analysis was conducted setting every model to match experimental data from a baseline case and then on varying ambient conditions such as density and temperature, as well as using different injection laws (i.e., different injection pressures).

3.2 Model Description

3.2.1 The VSB2 model as a starting point

In the past years several authors have implemented different approaches with the aim to reduce the grid dependency that affects the behavior of a liquid spray in engine simulations. The attention was focused on various aspects of the liquid-gas interaction. Abraham [44] presented a Virtual Liquid Source (VLS) model that treats the liquid region of the spray as a source of mass, momentum and energy without directly computing the liquid phase. This model uses the assumption that volume and mass occupied by liquid fuel is small relative to to the volume and mass of the total injected fuel. The authors showed that a good agreement between computed and experimental data was achieved but the model was completely inapplicable to simulations of sprays imping-ing a wall. Schmidt [45] analyzed the grid dependency problem from the point of view of the collision algorithm. In their work they extended the use of the no-time-counter (NTC) method to the general case of varying numbers of droplets in parcels. They outlined that an induced grid dependency appears when a Cartesian mesh is used and at the same time a multi-nozzle hollow cone spray is generated. In these conditions it could happen that very close to the injector nozzle there could be a collision interaction between two parcels with totally different trajectories (because injected from different points with different directions). The involved parcels would experience a change in their velocity even if the collision is physically not verified and the main consequence pointed out by the authors was the induction of a non-physical cloverleaf structure of the jet. To overcome this problem they applied the NTC algorithm combined with the use of a polar mesh properly designed for the collision process at each time-step. By doing this they could group the parcels so that they could interact in a more physical way and be more easily sorted when the collision algorithm was applied. Another way to reduce grid dependency is to consider the gaseous interaction volume surrounding each parcel. The idea to consider a sphere around every parcel is not completely new. Kösters et al. [46] applied it in the implementation of the *Stochastic Blob and Bubble spray model*, also known as VSB2 model. In that approach the idea was to construct a model that treats the spray and its break-up as one process, instead of summing individual, fragmenting droplets to a spray. VSB2 uses also the definition of an irregular *blob* that contains droplets sized according to some distribution and replaces the parcel containing identical droplets. The blob then interacts with a gaseous sphere, defined as *bubble*, whose radius is calculated considering the radius of an equivalent sphere including all the droplets in the parcel. This quantity is finally increased by the turbulent length scale, l_t, calculated in the cell hosting the parcel according to the well-known definition:

$$l_t = C_\mu \frac{k^{\frac{3}{2}}}{\varepsilon} \tag{3.1}$$

3.2.2 The new model

What associates the VSB2 model to the Spherical Volume Interaction DDM (SVI-DDM) is the idea to use a spherical volume with which the parcel interacts along its path inside the domain. The first difference between the two methods is that the new model keeps the standard definition of the parcel (i.e., it does not adopt any size distribution) and also does not assign to the sphere a turbulence based radius but a user defined value that in this study is set equal to the minimum cell size. This choice, that will be more clear later, is due to the fact that typical turbulent length scales in Diesel sprays (usually 0.1 to 1.0 times the nozzle diameter) are smaller than the mesh size adopted in this work (five times the nozzle diameter). Another important difference lies in the fact that this method allows interaction with every cells intersected by the sphere and located around the one hosting the parcel (Fig. 3.1). This guarantees an exchange of quantities between the phases that is in principle independent of the mesh structure.

This said, it is clear now that the adoption of a turbulence based radius with a minimum mesh size at least five times bigger than the injector nozzle would almost always result in the generation of spheres that are completely included in the cell where the parcel is located. This would make ineffective the use of the SVI approach with respect to the standard DDM.

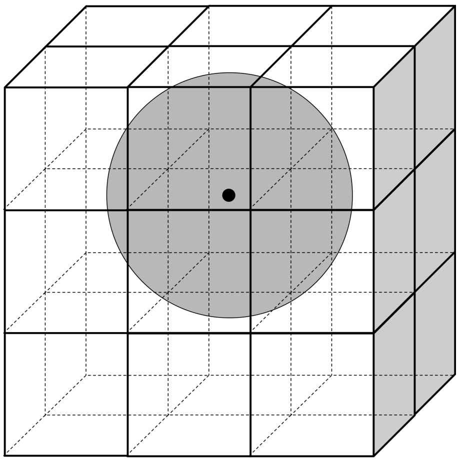

Figure 3.1: *Interaction volume: the sphere radius is equal to the cell size*

An analytical solution is not available to calculate the volumes resulting from the intersections between the sphere and the grid. For this purpose, the choice to use an approximate method was made. Once the sphere is defined, a cloud of $N_{p,tot}$ uniformly distributed points is collocated inside it. Then they are counted in each of the k cells in the proximity of the parcel and the fraction of the sphere volume included in the *i-th* cell is proportional to ratio of the number of points in the cell, $N_{p,i}$, over the total number of points in the sphere:

$$V_i = V_{sph} \frac{N_{p,i}}{N_{p,tot}} \quad , \quad i = 1, ..., k \tag{3.2}$$

The algorithm keeps track of the subdivision of the points in the involved cells and excludes all the ones that are outside of the domain (as it happens when a parcels is very close to the wall boundaries). By doing this, the barycenter of every section, $\mathbf{C}_i$, can be calculated and this information is then used to interpolate the physical properties of each section. Knowing the interpolated values and by means of weighted averages, it is possible to calculate the overall quantities referred to the gas included in the sphere. For example mass, velocity, temperature and pressure of the gas included in the sphere are computed as follows:

$$m_{sph} = \sum_{i=1}^{k} m_i = \sum_{i=1}^{k} [\tilde{\rho}_i(\mathbf{C}_i)\, V_i] \tag{3.3}$$

$$\mathbf{U}_{sph} = \frac{\sum_{i=1}^{k} \tilde{\mathbf{U}}_i(\mathbf{C}_i)\, m_i}{m_{sph}} \tag{3.4}$$

$$T_{sph} = \frac{\sum_{i=1}^{k} \tilde{T}_i(\mathbf{C}_i)\, m_i}{m_{sph}} \tag{3.5}$$

$$p_{sph} = \frac{\sum_{i=1}^{k} \tilde{p}_i(\mathbf{C}_i)\, m_i}{m_{sph}} \tag{3.6}$$

The way the values of the physical quantities at each barycenter are estimated is briefly explained in Sec. 3.2.6.

3.2.3 Numerical environment

The CFD tool used in the present work is OpenFOAM (version 2.0.x), together with the Lib-ICE set of solvers and libraries developed by the authors to simulate I.C. engines ([47] and [48]). Every solver, model, sub-model and library that were not already present in the standard version of OpenFOAM have been implemented in the Lib-ICE including the here presented SVI-DDM approach and a different interpretation of the KHRT breakup sub-model (see Sec. 3.3.2 and appendix A).

3.2.4 Liquid phase equations

The properties of each parcel (position, velocity, temperature, ...) at any given time are calculated by solving the mass, momentum and energy equations in a Lagrangian way. Multi-component sprays are supported, allowing simulation of realistic fuel surrogates. Droplet momentum is influenced by drag and gravity forces, while the liquid evaporation is estimated through the D^2-law and by suitable relaxation times calculated under standard and boiling conditions. The energy equation accounts for heat transfer and evaporation. Here, the equations for the liquid phase referred to a droplet of diameter D are presented in summary form; for further details refer to [49].

Droplet momentum equation:

$$m_d \frac{d\mathbf{U}_d}{dt} = -\frac{\pi D^2}{8} \rho C_d |\mathbf{U}_d - \mathbf{U}_g| (\mathbf{U}_d - \mathbf{U}_g) + m_d \mathbf{g} \tag{3.7}$$

Droplet mass equation (under standard evaporation):

$$\frac{dm_d}{dt} = -\frac{m_d}{\tau_e} \quad , \quad \frac{dD}{dt} = -\frac{D}{3\tau_e} \tag{3.8}$$

Droplet mass equation (under boiling conditions):

$$\frac{dm_d}{dt} = -\frac{m_d}{\tau_b} \quad , \quad \frac{dD}{dt} = -\frac{D}{3\tau_b} \tag{3.9}$$

Droplet energy equation:

$$m_d \frac{dh_d}{dt} = \dot{m}_d h_v(T_d) + \pi D \kappa \mathrm{Nu}(T - T_d) f \tag{3.10}$$

In the equations above, the subscript d refers to the single droplet, C_d is the drag coefficient, τ_e and τ_b are respectively the characteristic times for evaporation and boiling conditions. In the last equation h_v is the evaporation enthalpy at the temperature of the droplet, κ is the thermal conductivity, Nu is the Nusselt number and f is a factor which corrects the rate of heat exchange due to presence of mass transfer (see [49]).

3.2.5 Gas phase equations

The mass, momentum and energy equations are solved for a compressible, multi-component gas flow using the RANS approach ([49], [1]).

Conservation of mass:

$$\frac{\partial \rho}{\partial t} + \nabla \cdot (\rho \mathbf{U}_g) = \dot{\rho}^s \tag{3.11}$$

Conservation of species mass fractions:

$$\frac{\partial \rho Y_i}{\partial t} + \nabla \cdot (\rho \mathbf{U}_g Y_i) - \nabla \cdot [(\mu + \mu_t) \nabla Y_i] = \dot{\rho}_i^s + \dot{\rho}_i^{chem} \tag{3.12}$$

Conservation of momentum

$$\begin{aligned} \frac{\partial \rho \mathbf{U}_g}{\partial t} + \nabla \cdot (\rho \mathbf{U}_g \mathbf{U}_g) = \\ -\nabla p + \nabla \cdot [(\mu + \mu_t)(\nabla \mathbf{U}_g + (\nabla \mathbf{U}_g)^T)] \\ -\nabla \cdot [(\mu + \mu_t)(\frac{2}{3} \mathbf{tr}(\nabla \mathbf{U}_g)^T)] \rho \mathbf{g} + \mathbf{F}^s \end{aligned} \tag{3.13}$$

Conservation of energy:

$$\frac{\partial \rho h}{\partial t} + \nabla \cdot (\rho \mathbf{U}_g h) - \nabla \cdot [(\alpha + \alpha_t) \nabla h] = \dot{Q}^s + \frac{Dp}{dt} \tag{3.14}$$

In the equations above Y_i represent the mass fraction of the i-th specie, α is the thermal diffusivity and all the quantities with the t subscript are contribution obtained from the turbulence model. The symbols $\dot{\rho}^s$, $\dot{\rho}_i^s$, $\mathbf{F}^s$, $\dot{Q}^s$ identify source terms for mass, momentum and energy exchange between the gas and the liquid phases. The turbulence viscosity, μ_t, is provided by the turbulence model that in this work is always the standard *k-epsilon* as proposed in the original formulation of [18].

Equations 3.11 to 3.14 are discretized with the second-order, finite-volume method on a polyhedral mesh [50, 51]. The discretization schemes adopted in this work will be shortly presented in Sec. 3.4. Discretization of Laplacian, convection and temporal derivatives terms can be performed with the different schemes originally available in the code [50]. The transient SIMPLE algorithm is used for the pressure-velocity coupling [52].

3.2.6 Gas to liquid coupling

The technique to calculate gas velocity at parcel position slightly differs between the two methods but rely on the same *cell-point-face* approach [49]. This method lets the parcels experience a continuous velocity field within the computational domain and in both standard and SVI approach it allows a reduction of grid dependency. Firstly, the velocity field, which is stored at the mesh cell centers, is interpolated both at the mesh faces and mesh points locations. Then, a tetrahedron is built with the closest points (cell centers, face centers, mesh points) around the point of interest, $\mathbf{P}$. The distance between $\mathbf{P}$ and one of the tetrahedron faces is α_i, while $\alpha_i + \beta_i$ represents the distance between the same face and its opposite vertex. The interpolated velocity at the point $\mathbf{P}$ is:

$$\mathbf{U}(\mathbf{P}) = \sum_{i=1}^{4} \frac{\beta_i}{\alpha_i + \beta_i} \mathbf{U}_i \tag{3.15}$$

If the standard DDM approach is used, $\mathbf{P}$ represents the parcel position, while in the SVI-DDM $\mathbf{P}$ is the generic barycenter of one of the intersections between the sphere and the mesh. This means that in the new approach proposed here the procedure is repeated for every sphere fraction and then the velocity values are averaged according to the Eq. 3.4. For stability reasons, the same technique cannot be employed to estimate the gas phase temperature and pressure at the parcel positions: to avoid problems in the evaluation of the divergences therms, these quantities are assumed to have the same values of the cell center where the parcel is found [49]. As before in the case of the SVI-DDM the cell center values are assigned to the sphere fractions and then averaged according to Eqs. 3.5 and 3.6.

3.2.7 Liquid to gas coupling

Every parcel is tracked along its path by using a face-to-face algorithm. In the standard DDM approach this makes it possible to identify all the cells crossed by each parcel during one time step and to split the Lagrangian source terms of the Eulerian equations accordingly. This technique was proved to increase the accuracy and stability of Diesel spray simulations [49].

In the SVI-DDM some features are added. The Lagrangian source terms are split according to the cells intersected by the sphere along the parcel path and to the gas mass contained in every sphere section. Since the new methodology is more computational demanding with respect to the standard procedure, the sphere properties are updated within the time step every time the parcel covers a distance larger than the $10\ \%$ of the sphere radius. This choice was made after testing the model on a simple case: the percentage of the radius was gradually increased and the choice of the $10\ \%$ ensured a good compromise between accuracy and reduction of computational time.

3.3 Spray sub-models

3.3.1 Injection Model

In accordance with the break-up model (described in Sec. 3.3.2) the Blob-Injection model was used [1]. Every parcel is injected from a point located in a disk whose size is equal to the injector nozzle: the points are randomly chosen according to a uniform distribution. The frequency of the addition of new parcels is directly related to the fuel injection rate, assuming constant density of the liquid fuel and ideally spherical droplets. Every injected parcel is characterized by the same diameter which is comparable to the size of the nozzle hole on the side of the gas phase. They are introduced in the domain according to the following relation, knowing the total number of parcel to inject:

$$N(t) = \max\left(1, \Delta t \frac{N_{tot}}{(t_{eoi} - t_{soi})}\right) \tag{3.16}$$

The mass and the velocity assigned to each parcel are calculated as a function of injection profile and total mass to inject. The half-angle of the spray is derived from the assumption that the droplet velocity component perpendicular to the spray axis is proportional to the wave growth rate, Ω, of the most unstable wave of the liquid jet:

$$\tan\left(\frac{\alpha}{2}\right) = \frac{v_\perp}{|\mathbf{U}_d|} = \frac{\Omega\Lambda}{A|\mathbf{U}_d|} = \frac{4\pi}{A}\sqrt{\frac{\rho_g}{\rho_l}}f(\mathrm{Ta}) \tag{3.17}$$

where Λ is the wave length and $f(\mathrm{Ta})$ is a function of the Taylor number that asymptotically approaches $(3^{0.5}/6)$ for Ta > 100, which is typically satisfied in Diesel sprays. The quantity A is defined in terms of the length to diameter ratio of the nozzle hole as:

$$A = 3.0 + \frac{l_{noz}/d_{noz}}{3.6} \tag{3.18}$$

The injection direction is then assigned as uniformly distributed in a cone of half-angle $\alpha/2$.

3.3.2 Breakup Model

Primary breakup is described by means of the Blob-Injection model (see Sec. 3.3.1) combined with the Wave-breakup model. Secondary break-up is calculated by means of the KHRT model that was used to describe atomization of the spray droplets. Due to a different interpretation of the theory at the base of the KHRT model the implementation here adopted differs from the one presented in the official version of OpenFOAM [53], so a complete description of the KHRT is provided in the appendix A.

3.3.3 Evaporation, Heat Exchange and Drag Models

The drag force acting on the droplets is modeled by means of the correlations proposed by Krajli [54]. To correctly describe the mass and energy exchange between the liquid and the surrounding gas, Eq. 3.8 requires expressions for the Sherwood and Nusselt numbers which are modeled according to the approach described by Crowe [55]. According to Kosaka [56] turbulent dispersion is one of the processes which produce the inhomogeneous distribution of fuel mass concentration, but for the purposes of this work and to reduce the results sensitivity to the turbulence model [1] effects of turbulent dispersion were not considered. Collision models were also not used, because of their limited effects on the Sauter Mean Radius (SMR) of an evaporating spray [57].

3.4 Mesh management tools

The grids used in this work, due to the very simple geometry of the physical domain, were created by means of the *blockMesh* OpenFOAM utility. What is important to mention is that the *adptive local mesh-refinement* (*ALMR*) technique was used [58].

3.4.1 Refinement strategy

To preserve a good quality of the mesh, only hexahedral and degenerated hexahedral cells (wedges) can be refined. An initial computational mesh has to be provided by the user and the size should be fine enough to correctly reproduce the geometrical domain to be simulated and the main details of the initial flow-field [50]. A geometric field is chosen as an error estimator and when its values lie in a user-specified interval the parent cell is split into eight child cells by introducing new nodes at the cell centroid and at the mesh face centers [50]. An arbitrary level of refinement is chosen by the user, and a maximum number of cells can be specified in order to keep a desired value of the mesh size. Refined cells are marked with a flag number and by means of it the mesh can be easily unrefined when the values of the error estimator are outside the specified interval. In this work the unrefinement feature was disabled while the initial mesh size was set equal to 4 mm, with three levels of auto-refinement. In this way a minimum mesh size of 0.5 mm was reached. The choice to adopt a 0.5 mm size was due to the necessity of keeping a reasonable number of cell during the calculations, especially for what concerns the engine simulations that will be shown in Sec. 3.6 and that will involve a number of elements in the range of 2.5-3.0 millions.

3.4.2 Refinement criterion

The geometric field used as a refinement criterion is represented by the total fuel mass fraction (liquid and gas) in each cell:

$$Y_{l+g} = \frac{m_{f,l} + \rho Y_{tf} V_{cell}}{\rho V_{cell}} \tag{3.19}$$

where $m_{f,l}$ is the liquid mass of all the parcels belonging to the cell, Y_{tf} is the fuel mass fraction in the continuous phase, ρ is the gas phase density and V_{cell} is the cell volume. The lower threshold value was set to 10^{-4} while the higher was 1. This allows an adequate refinement of the mesh close to the nozzle in the first time steps.

3.5 Results and discussion

The proposed approach was validated with different sets of experiments run in non-reacting conditions. All the tests were conducted in an optical, constant-volume vessel with a single-component fuel (n-dodecane, $C_{12}H_{26}$) and the collected data were used to tune the spray model constants. As briefly outlined in the introduction, in order to select a common setup for all the cases, experimental data of a baseline case were used. After reaching a good agreement in terms of liquid length and fuel vapor penetration between calculated results and experimental measurements, four analyses were conducted. In the first one the injector position was moved from the center of the cell (taken as reference condition) to one of the corner vertices, considering also an intermediate position. This was made for both, standard and SVI DDM with the aim to test the predictive capability of the latter. After this first phase, ambient density and injection pressure were varied to test the robustness of the chosen setup and the sensitivity of the new approach to the varied conditions. The third analysis was focused on the dependency of the results on the spray-grid mutual orientation. Finally a simplified engine case was simulated to test the behavior of the new model when multiple-nozzle injectors are used.

3.5.1 SANDIA constant volume vessel

All the simulations in this work were conducted on a mesh representing the SANDIA constant volume vessel. The vessel has a cubical-shaped combustion chamber. The characteristic dimension of the cube is 108 mm. The fuel injector is located in one side port using a metal insert that forms the right wall of the combustion chamber. Two spark plugs and a mixing fan are mounted in another metal insert that forms the top wall of the chamber. Optical access is provided by four sapphire windows with clear apertures of 102 mm located in the other four ports. For wall heat transfer modeling purposes, the steel vessel and metal inserts for the injector and spark plugs are made of 4340 steel.

In this chamber a mixture of gases can be burnt to reach the necessary conditions in terms of pressure, density, temperature and chemical composition. To obtain a non-reacting environment for the spray to evolve, a stoichiometric mixture was burnt to obtain a negligible oxygen content after the combustion.

To describe the geometry, a cubic mesh whose edge is 108 mm was created. The grid is three-dimensional and its cells are perfectly cubic with an initial size of 4 mm. The injector is placed in a cell belonging to what will become the second plane of cells starting from the wall after the refinement procedure.

Fig. 3.2 is a simple scheme to show the three different positions chosen to perform the calculations.

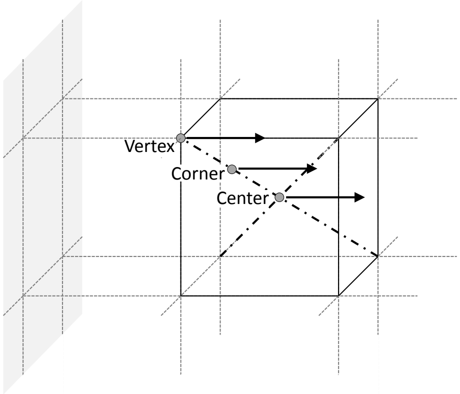

Figure 3.2: *Injection positions and directions*

3.5.2 Analysis strategy

Among the numerous data available from the experiments run on the Sandia Constant Volume Vessel, the Spray A series was selected. The Tab. 3.1 summarizes the analyzed cases. The first row refers to the baseline case on which the various sub-models were set, second and third row to the ambient density variation the last two to injection pressure variation.

Case Name	***Injection Pressure*** **[MPa]**	***Ambient Density*** **[kg/m^3]**	***Ambient Temperature*** **[K]**	***Ambient Pressure*** **[MPa]**
Baseline	**150**	**22.8**	**900**	**6**
Density15.2	**150**	**15.2**	**900**	**4**
Density7.6	**150**	**7.6**	**900**	**2**
Pressure100	**100**	**22.8**	**900**	**6**
Pressure50	**50**	**22.8**	**900**	**6**

Table 3.1: *Simulated cases*

As said before the reference case had the injector placed in the cell center. The model constants (turbulence, breakup, etc.) were set to match experimental data referring to the baseline case.

The Tab. 3.2 reports the constants used to tune the turbulence model. If compared to the original formulation C_1 is the only constant that was tuned to match experimental data better.

C_μ	C_1	C_2	C_3	σ_k	σ_ϵ
0.09	1.552	1.92	-0.33	1	1.4

Table 3.2: *k-epsilon turbulence model constants*

The graphic in Fig. 3.3 shows the achieved agreement in terms of liquid length and vapor penetration.

The calculated liquid length was measured taking the distance of the parcel representing the 99 % of liquid mass in system, while the jet penetration is taken as the farthest point along the injection direction where the mixture fraction, Z, is at least equal to the 0.1 % of the cell volume. Fig. 3.4 shows good results also in terms of Mixture Fraction profiles at different locations and contours of Fig. 3.5 confirm this. Fig. 3.5 shows also that the calculated results are not able to catch finer spray structure present in experimental measures. This is mostly due to the nature of RANS simulations which leads to time-averaged fields characterized by an isotropic turbulence combined with what is mainly an axi-symmetrical problem. Furthermore, the choice of a minimum mesh size of 0.5 mm does not allow to predict smaller structures.

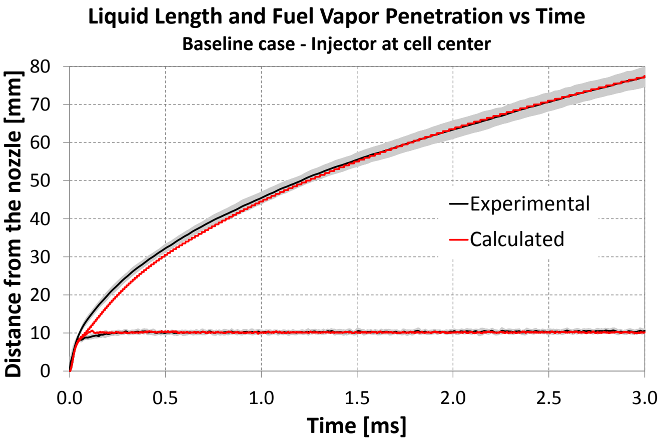

Figure 3.3: *Liquid Length and Vapor Penetration. Baseline*

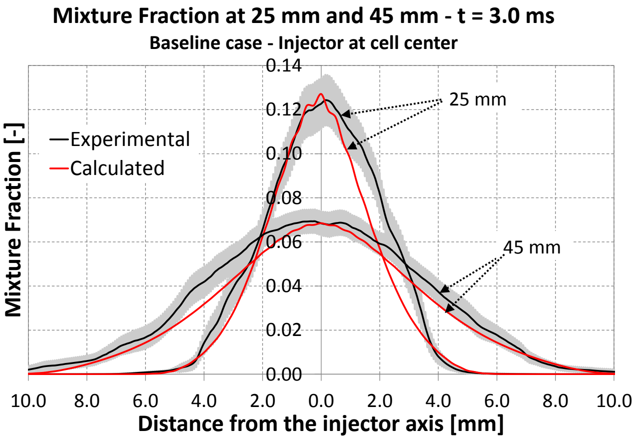

Figure 3.4: *Mixture Fraction at 25 mm and 45 mm. Baseline*

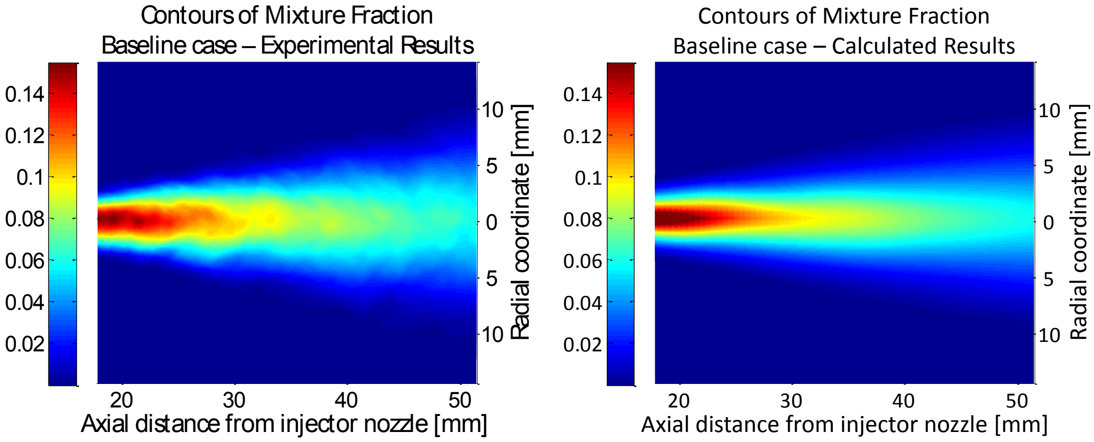

,

Figure 3.5: *Mixture Fraction contours. Baseline*

3.5.3 SVI-DDM vs new model comparison

Once defined the best setup, the baseline case was simulated on varying the injector position and comparing results of the SVI-DDM to those obtained with the standard DDM approach. In order to guarantee consistency, the same set of sub-models constant was used. As shown in Figs. 3.6 to 3.10 the standard approach is strongly affected by the choice of the injector location. This is due to the path followed by the parcels across the cells involved in the exchange processes. The case with standard DDM and nozzle at the vertex gives the most similar results to those obtained with the SVI-DDM: this happens because, injecting from a vertex and due to the disk injection (see Sec. 3.3.1), the parcels are uniformly distributed along four rows of cells so that the exchange of mass, momentum and energy is distributed on more cells than in the other two cases. In the same way the case with the nozzle in the center shows a larger penetration in terms of both liquid and vapor.

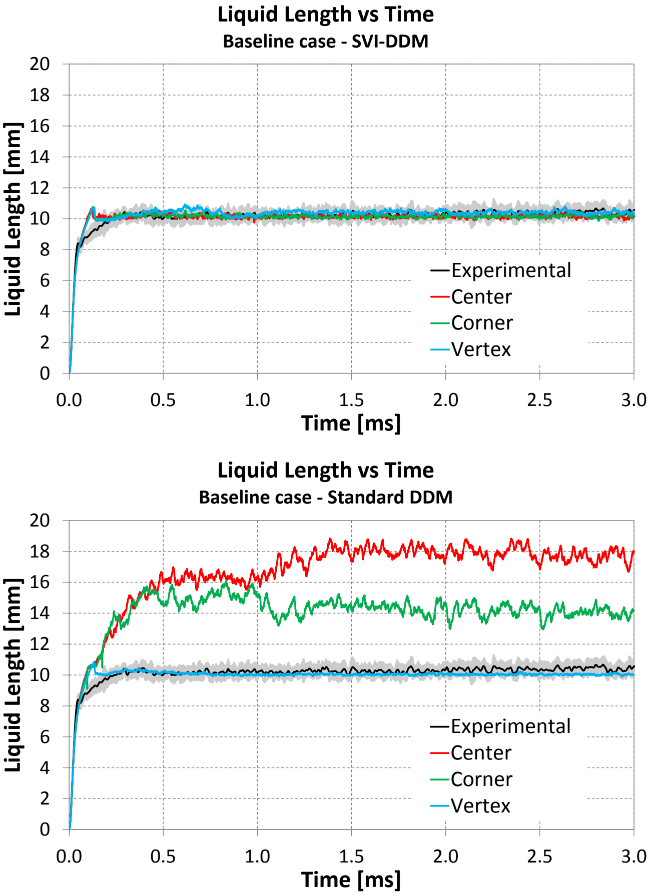

Figure 3.6: *Liquid Length on varying injector position*

The adoption of the new approach allows to obtain a very good independence on the nozzle position. The calculated liquid length is practically the same for all the cases and a more contained variability in jet penetration is observed. The new model allows also to reduce indirectly the fluctuations observed in the liquid penetration (Fig. 3.6). They are probably due to the reduced drag acting on the parcels when most of them interact with a smaller number of cells . Because of the locally higher momentum exchanged with the Eulerian domain, gas velocity increases and drag decreases. A lower drag slows less the parcels which penetrate more and create a spray where the liquid is more spread in the axial direction than in the radial. This, combined with a 99% threshold on liquid mass results in a more fluctuating liquid length.

Standard approach seems to catch better initial vapor penetration in corner and center cases. This is due to higher gas velocities that allow the jet to penetrate more in the domain. Even if at the beginning the jet penetration is better described, the higher velocities lead to over-estimate the jet length in the steady state phase of injection. An increasing of mesh resolution in the near nozzle region (keeping an acceptable void fraction value) could represent better vapor penetration in the initial part of injection using the SVI-DDM. This should be able to catch velocity peaks that are probably smoothed by the adoption of a 0.5 mm minimum mesh size.

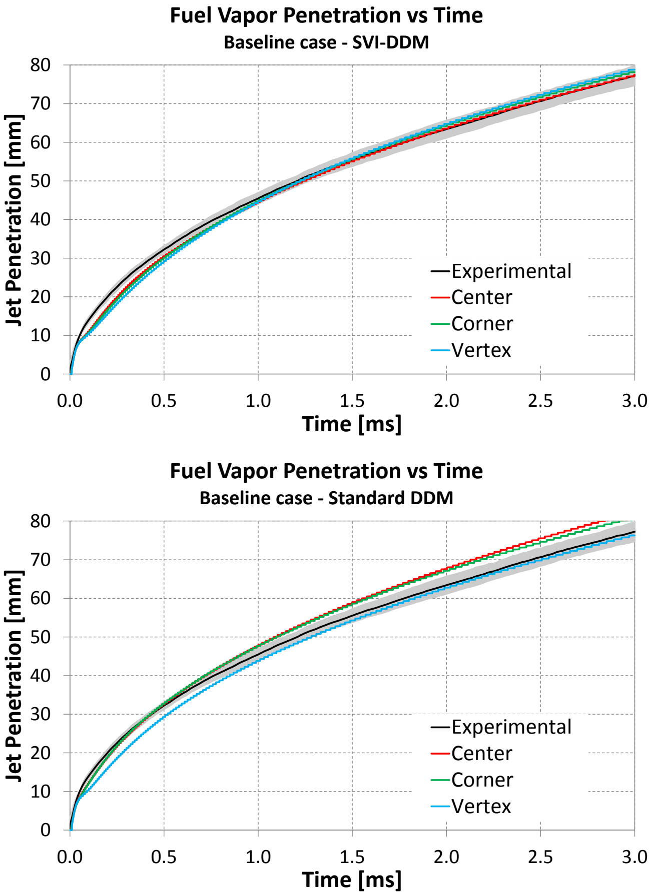

Figure 3.7: *Vapor Penetration on varying injector position*

Figs. 3.8 to 3.9 show the axial profile of mixture fraction and axial component of gas velocity. It is clear that the mixture fraction is certainly described better by the SVI-DDM. Indeed, using the standard DDM and keeping the same constants setup could result (cell center case) in an inconsistent mixture fraction profile in the near-nozzle region. This behavior could be explained as follows: the first peak is mainly related to a strong creation of new droplets in the near nozzle region according to the KH breakup, the second peak is due to a delayed catastrophic breakup (RT mechanism) that takes place too far from the nozzle creating a non-physical distribution of mixture fraction and making the liquid penetrate more. The same behavior is shown also in the corner case, but with more limited consequences: since the liquid penetrates less than in the center case, but more than in the vertex one, mixture fraction shows a flat profile between 3 and 7 mm from the nozzle due to a slightly delayed catastrophic breakup.

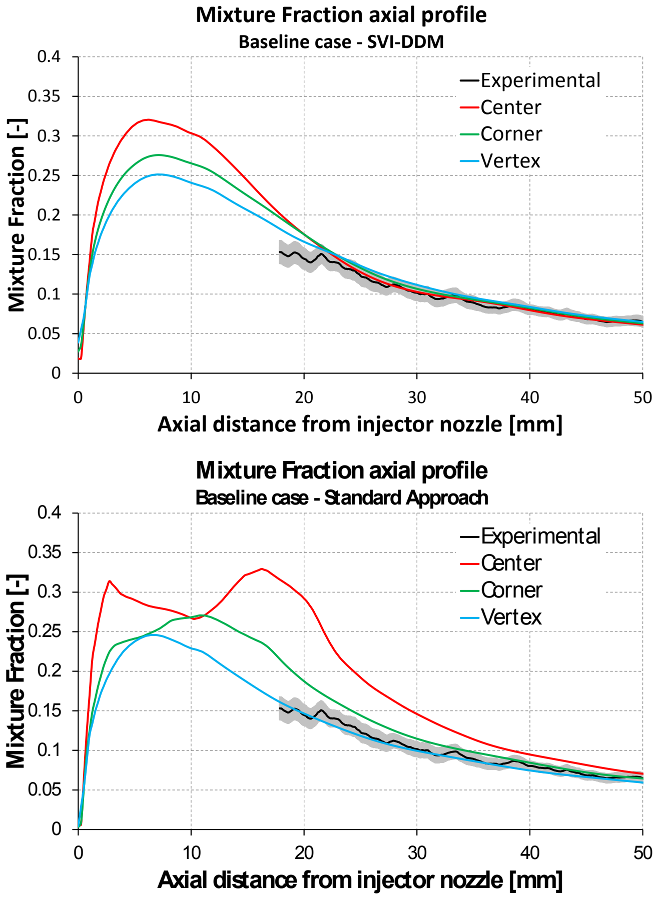

Figure 3.8: *Axial mixture fraction on varying inj. position*

Also the axial velocity profiles are less dependent on the injection position if the SVI-DDM is used. Having a reduced variability of axial velocity and smaller velocity gradients in the near-nozzle results in a good agreement of the three cases in the far-nozzle region, especially starting from 22-23 mm from the injector nozzle. The only noticeable difference in favor of the standard approach is that the vertex case predicts slightly better the mixture fraction distribution in the region at 18-20 mm from the nozzle. This happens because of the spherical control volumes around the parcel created by the SVI-DDM: in the vertex case the spheres ideally overlap around the injection axis concentrating the momentum exchange mainly in the cell of that area. This increases the gas velocity in that region, explaining the small differences at 18-20 mm in the axial profiles of the two vertex cases.

Fig. 3.9 shows that the SVI-DDM is able to reduce peak velocities in both the critical cases of standard approach. The reduction is more evident in the center case (about

20%) while in the corner case is more contained (in the order of the 10%). Because of lack of experimental data in the near nozzle region, nothing can be said about the predicted value, but the fact that, using the new approach, the variability of results is smaller can lead to more focused analysis of near nozzle region in future works.

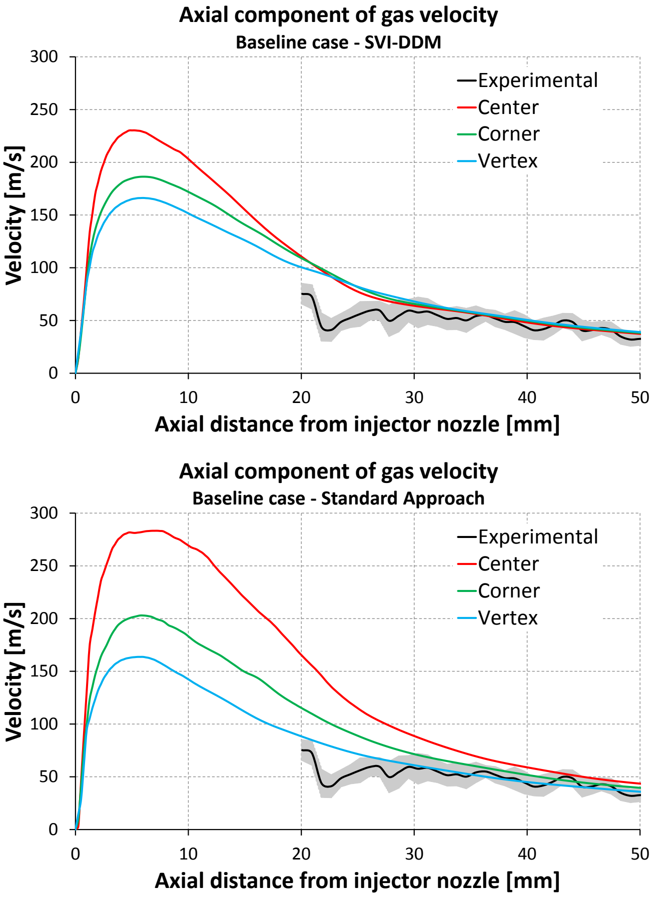

Figure 3.9: *Axial velocity profiles on varying inj. position*

3.5.4 Global and local analysis of spray morphology for baseline conditions

This section shows how the adoption of the SVI-DDM approach is effectively valid to reduce also the variability of global and local characteristics of the liquid spray morphology. Fig. 3.10 shows the global Sauter Mean Diameter vs time. As previously pointed out, corner and center positions with standard approach lead to have parcels interacting with less cells. This affects the drag that causes a lower deceleration of the parcels due to lower relative velocities. The correlation of the resulting wavelength in the RT breakup (see appendix A) shows that it increases as the deceleration of the parcel decreases making less probable the RT breakup mechanism itself and enhancing the KH breakup. At the same time KH usually creates very small parcels when liquid mass is shredded from the parent parcels resulting in a lower SMD.

The trend seen in Fig. 3.10 is confirmed by the analysis of the local droplet size distribution. Figs. 3.11 to 3.28 have been created at 1.0 ms after the start of injection

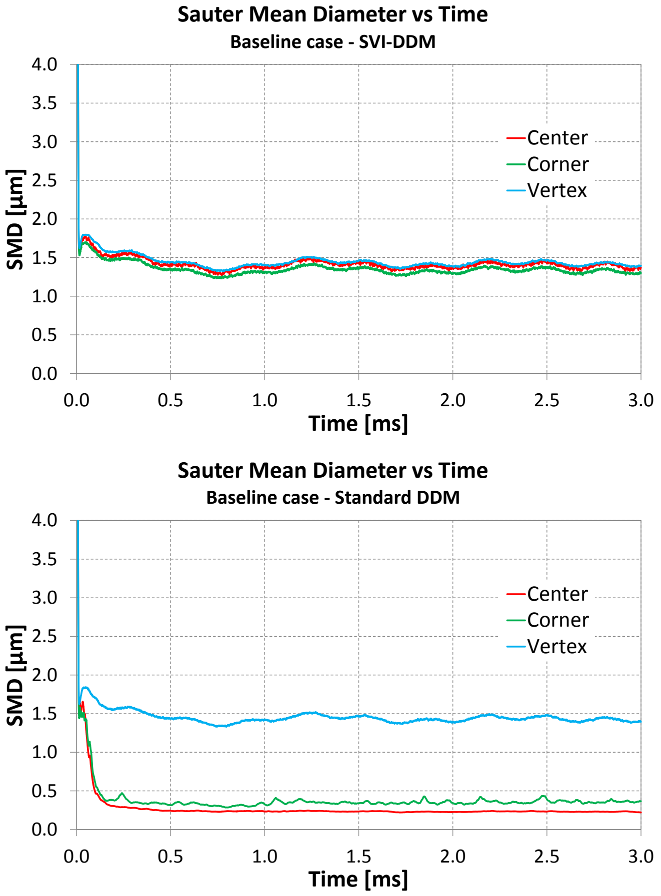

Figure 3.10: *SMD on varying injector position*

(conditions of steady state liquid penetration). The results refers to all the droplets contained in a plane normal to the injection axis with a thickness equal to the minimum cell size and located at a user-defined distance from the nozzle. The black bars represent the probability density function (PDF) of the droplet radius (scale is on the left), while the grey area shows the cumulative distribution function (CDF) calculated according to the liquid mass included in the considered slice (scale is on the right). As it is possible to see, a very contained variability of the shape of the CDF is observed with the new approach, furthermore the only case that shows similarities between the two DDM approaches is again the vertex case. The shapes of the CDFs help to explain also why the value of SMD is higher when SVI-DDM is used: only 10% of the liquid mass is included in parcels characterized by a very small radius. This value increases to 20-25 % at 2.5 mm and to 55-60 % at 5.0 mm when standard DDM is adopted consequently leading to a lower value of the global SMD.

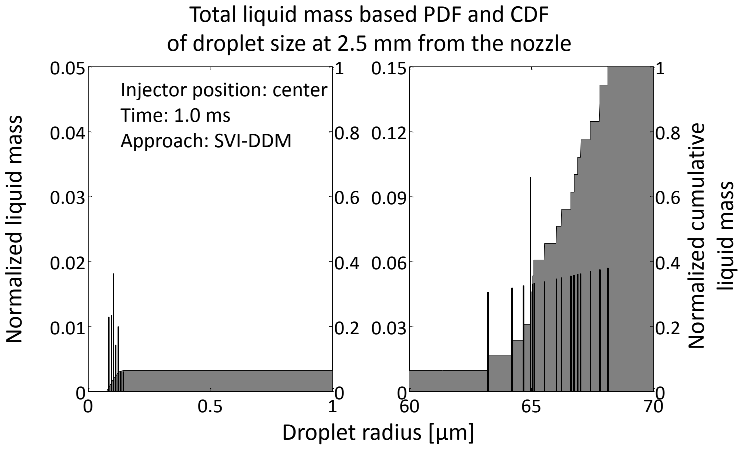

Figure 3.11: *Droplet size distribution at 2.5 mm from the injector nozzle. Center case with SVI-DDM*

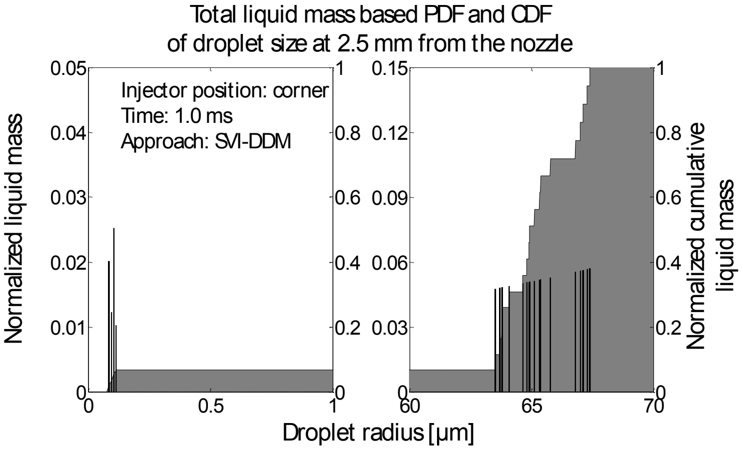

Figure 3.12: *Droplet size distribution at 2.5 mm from the injector nozzle. Corner case with SVI-DDM*

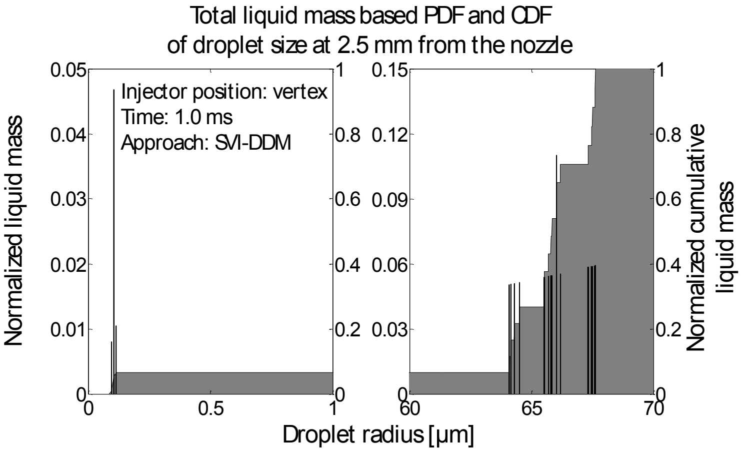

Figure 3.13: *Droplet size distribution at 2.5 mm from the injector nozzle. Vertex case with SVI-DDM*

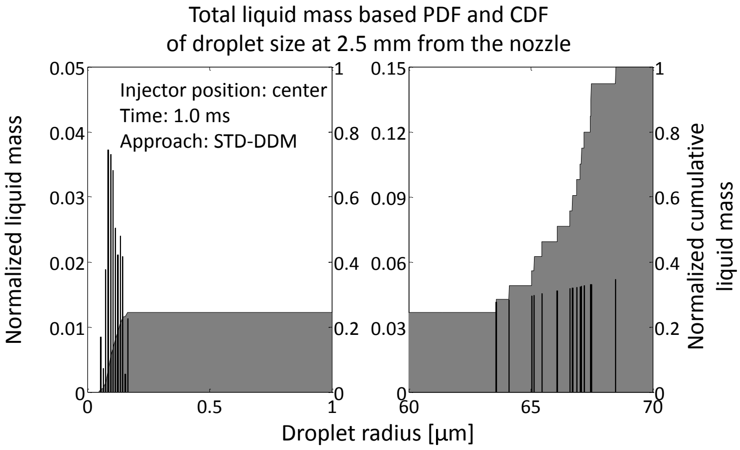

Figure 3.14: *Droplet size distribution at 2.5 mm from the injector nozzle. Center case with std DDM*

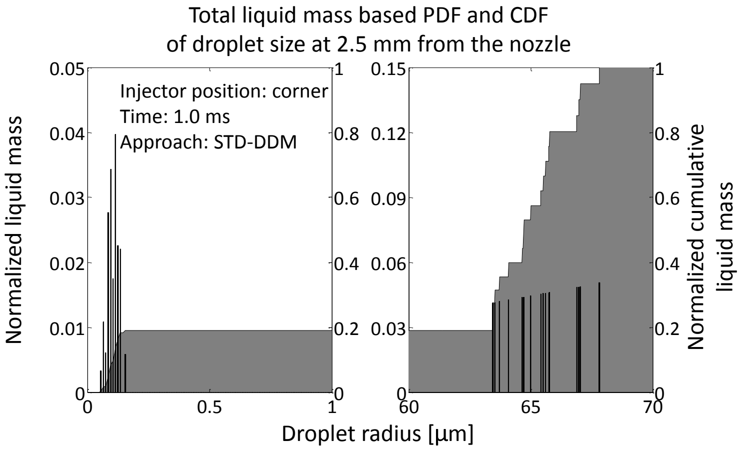

Figure 3.15: *Droplet size distribution at 2.5 mm from the injector nozzle. Corner case with std DDM*

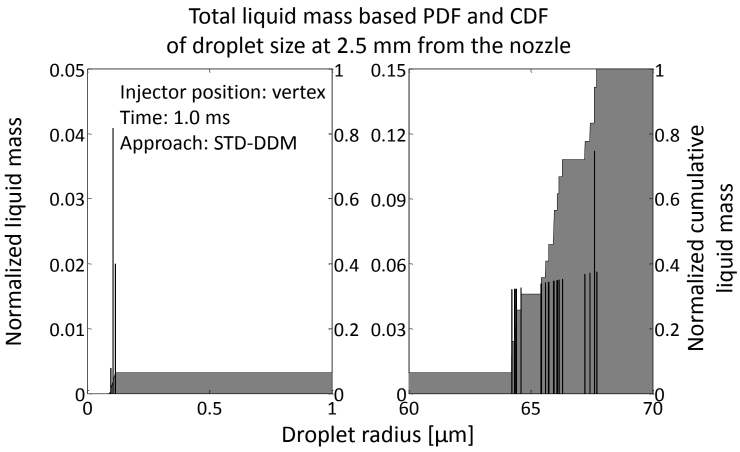

Figure 3.16: *Droplet size distribution at 2.5 mm from the injector nozzle. Vertex case with std DDM*

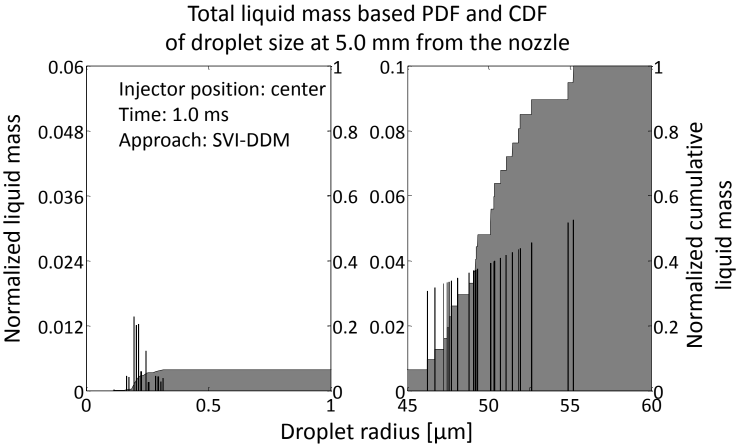

Figure 3.17: *Droplet size distribution at 5.0 mm from the injector nozzle. Center case with SVI-DDM*

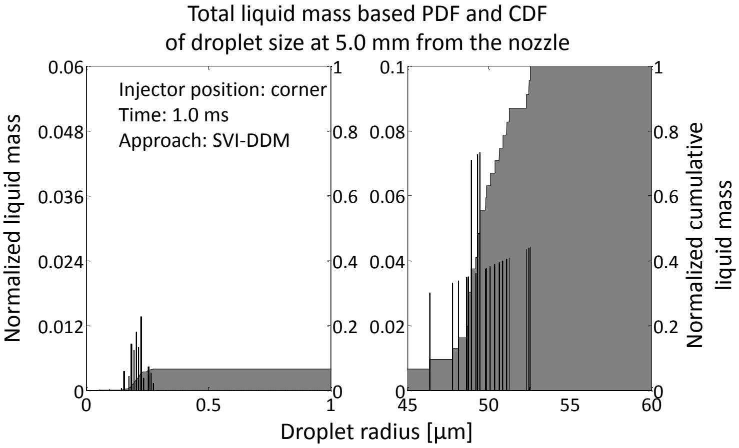

Figure 3.18: *Droplet size distribution at 5.0 mm from the injector nozzle. Corner case with SVI-DDM*

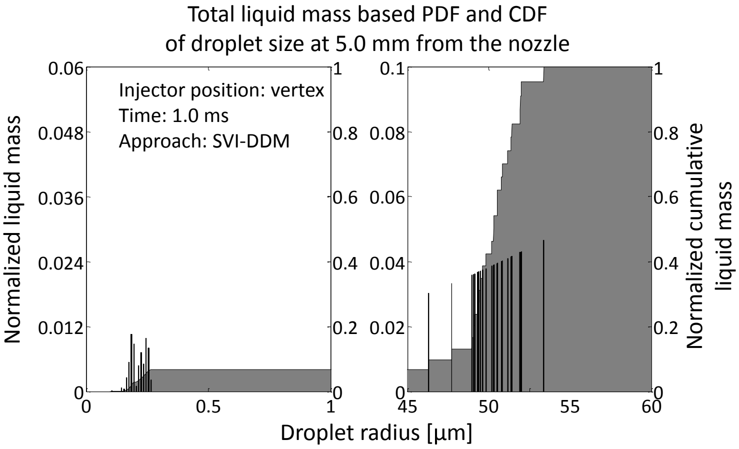

Figure 3.19: *Droplet size distribution at 5.0 mm from the injector nozzle. Vertex case with SVI-DDM*

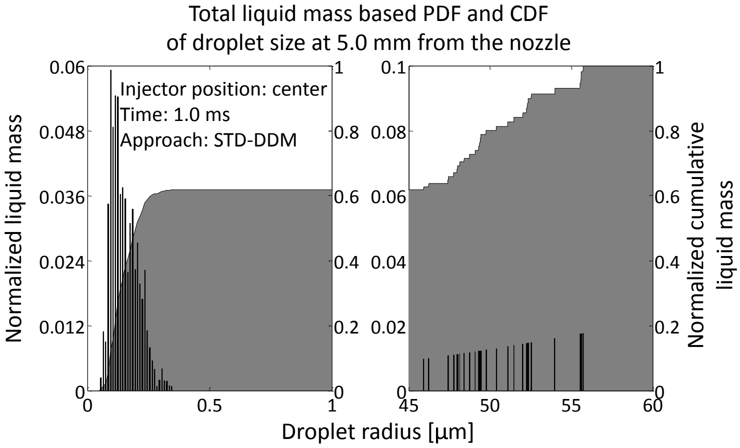

Figure 3.20: *Droplet size distribution at 5.0 mm from the injector nozzle. Center case with std DDM*

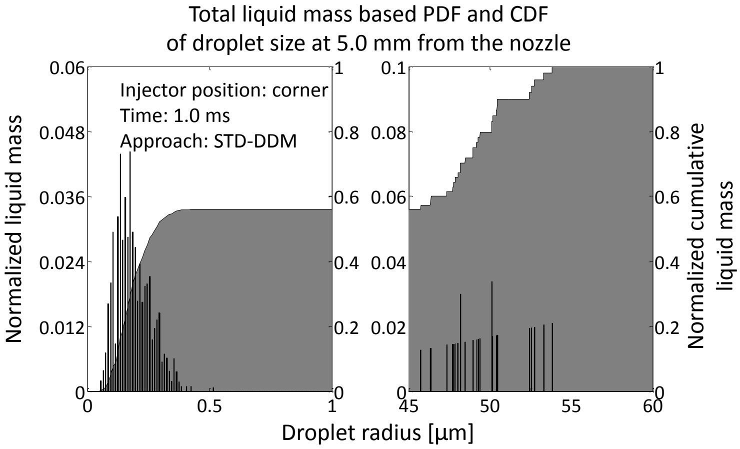

Figure 3.21: *Droplet size distribution at 5.0 mm from the injector nozzle. Corner case with std DDM*

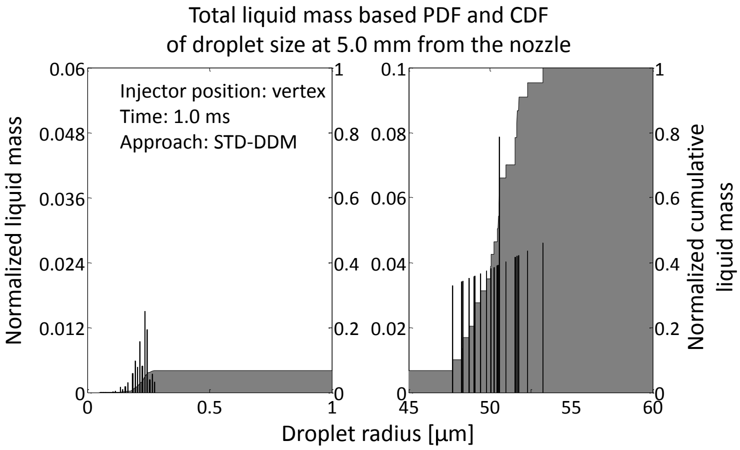

Figure 3.22: *Droplet size distribution at 5.0 mm from the injector nozzle. Vertex case with std DDM*

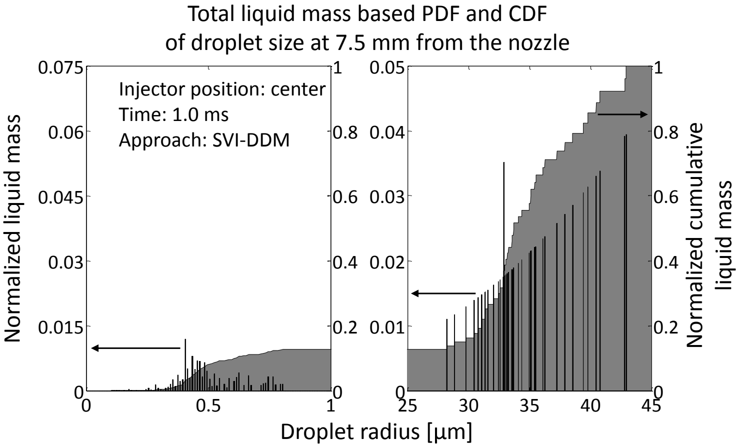

Figure 3.23: *Droplet size distribution at 7.5 mm from the injector nozzle. Center case with SVI-DDM*

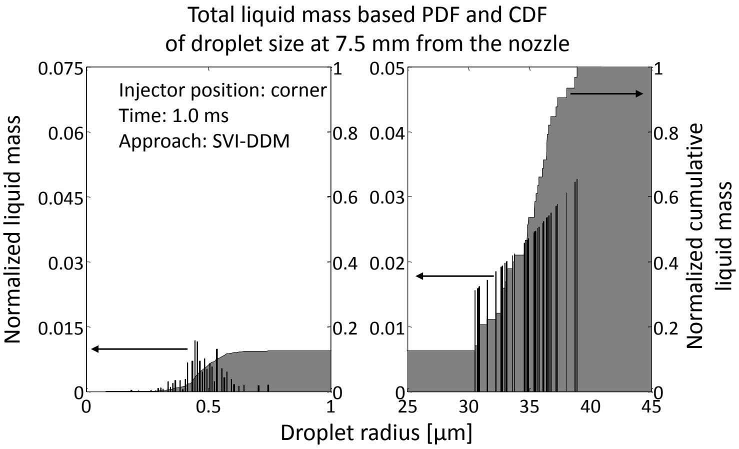

Figure 3.24: *Droplet size distribution at 7.5 mm from the injector nozzle. Corner case with SVI-DDM*

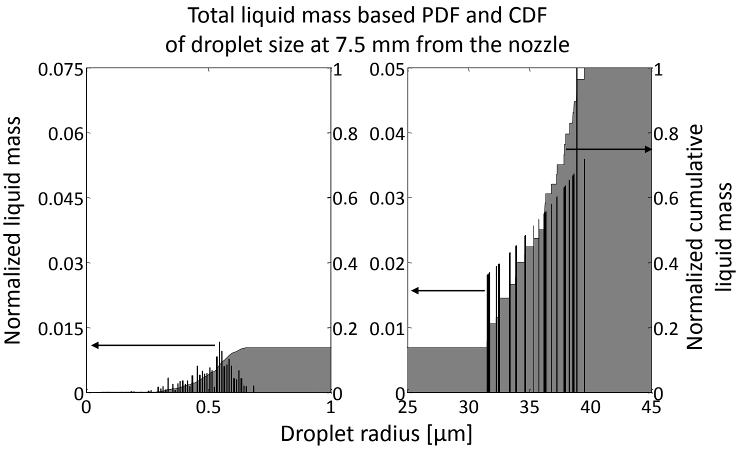

Figure 3.25: *Droplet size distribution at 7.5 mm from the injector nozzle. Vertex case with SVI-DDM*

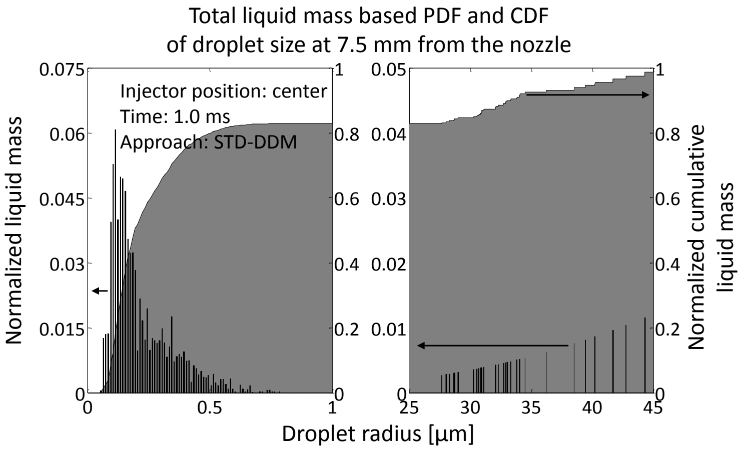

Figure 3.26: *Droplet size distribution at 7.5 mm from the injector nozzle. Center case with std DDM*

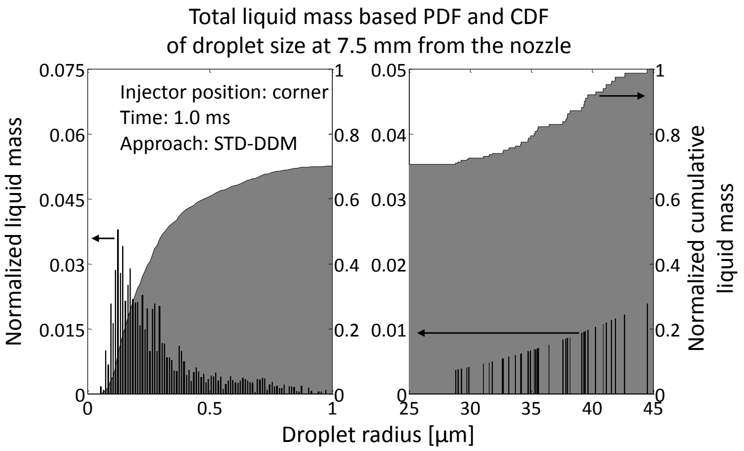

Figure 3.27: *Droplet size distribution at 7.5 mm from the injector nozzle. Corner case with std DDM*

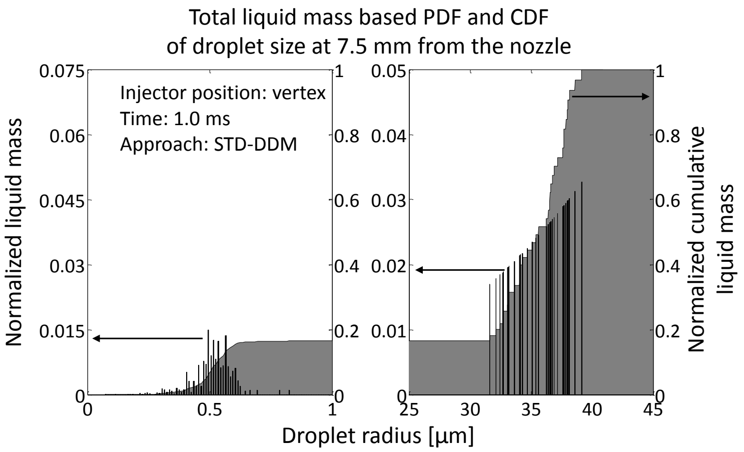

Figure 3.28: *Droplet size distribution at 7.5 mm from the injector nozzle. Vertex case with std DDM*

3.5.5 Model response to ambient density variation

The same analysis of Sec. 3.5.3 was performed using different ambient conditions. The density was decreased from 22.8 to 15.2 and 7.6 kg/m^3, keeping constant ambient temperature. The tunable parameters were left the same as they were defined after matching experimental baseline results. The only available experimental measurement for the two cases was the vapor penetration and, as showed in Figs. 3.29 to 3.31, both approaches were able to respond to the changed ambient conditions. The only inconsistency was identified in a flat trend of liquid length with standard DDM when the ambient density was increased from 15.2 to 22.8 kg/m^3. This could be seen as a confirmation that using the standard DDM approach is necessary to tune the models every time the injector position changes in order to avoid a wrong estimation of the momentum exchange. As for the baseline case, the SVI-DDM showed a more contained variability of the results with respect to the injector position for what concerns vapor penetration. Also computed liquid length (see Fig. 3.29) showed a similar behavior as for the baseline case, indeed is shown that this quantity was practically independent on the injector position responding only to the ambient density variation. Furthermore, even if experimental measurements of liquid length were not available for the simulated injector, the found average value was in accordance to the trend shown in the work of [59]. In that work the authors simulated a similar injector in comparable conditions to those of the present work.

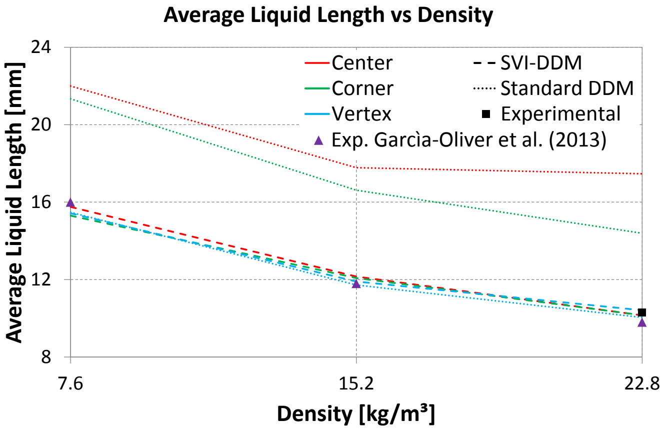

Figure 3.29: *Average Liquid Length on varying injector position and ambient density*

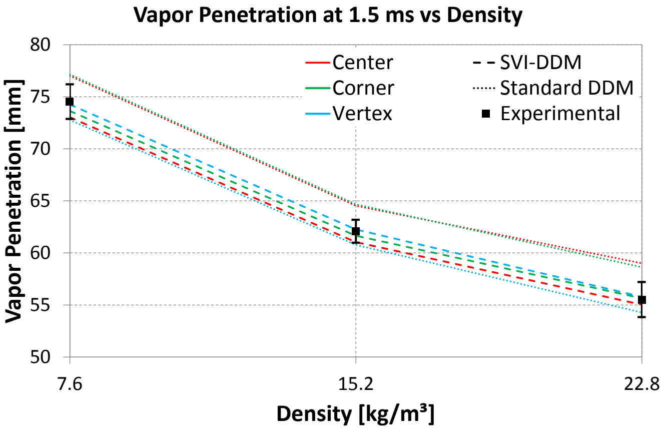

Figure 3.30: *Vapor Penetration at 1.5 ms on varying injector position and ambient density*

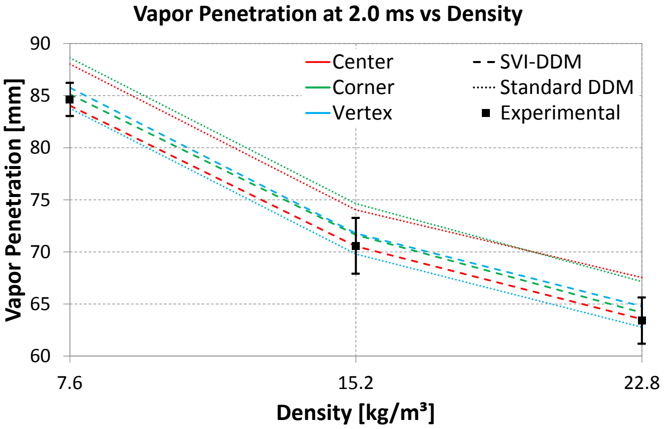

Figure 3.31: *Vapor Penetration at 2.0 ms on varying injector position and ambient density*

3.5.6 Model response to injection pressure variation

The analysis made in this section aims to show how the two approaches respond to a change of the injection pressure. As done for most of the previous analysis, the experimental data were taken from the SANDIA ECN database [43], while the three injection laws used to simulate the injection pressure variation were generated by means of an algorithm made available by CMT [60]. This algorithm is able to generate a coherent injection law, starting from injection and ambient pressures, nozzle diameter, nozzle discharge coefficient, fuel type and injection duration. As done for the previous sections the results of Figs. 3.32 to 3.34 are shown on varying the injector position within the hosting cell.

Fig. 3.32 confirms again that the SVI-DDM approach is able to guarantee a very contained variability in terms of calculated average liquid length. As for the previous cases the most similar results between the two models can be obtained only if the injector is placed in a cell vertex when the standard DDM is used. Both models predict a correct liquid length for the 100 MPa case, while in the 50 MPa case a slightly larger value results. Figs. 3.33 and 3.34 show a more contained variability of the calculated jet length when the new DDM approach is used. The vapor penetration is a little underestimated with respect to experimental results, but the general trend is well caught. The differences in liquid and vapor penetration could be due to choice to use an algorithm for generating the injection law that does not take in account that the real law used in the experiments could be slightly different from the one here adopted. As seen for the density variation analysis, the case with injector in the center and standard DDM is the most critical. The liquid length shows a divergent trend going from 100 to 150 MPa. Again, the probable explanation is that the use of a wrong set of models constants leads to a wrong computation of the momentum exchange between the two phases.

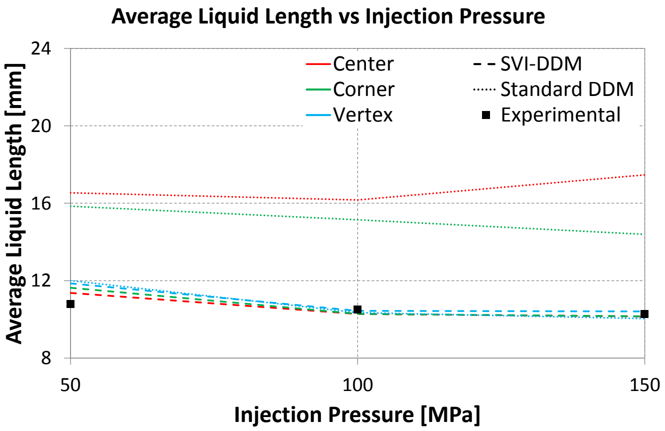

Figure 3.32: *Average Liquid Length on varying injector position and injection pressure*

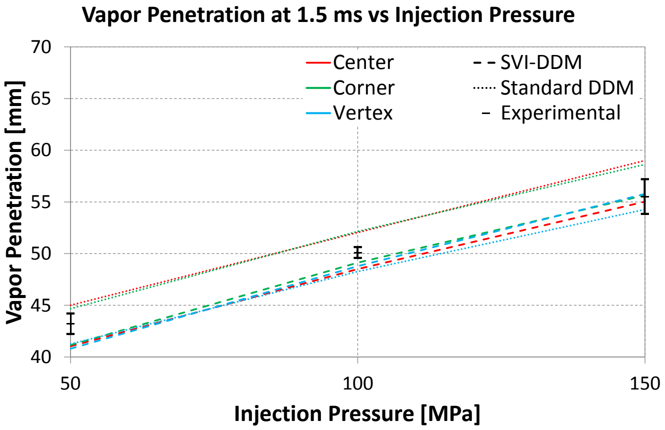

Figure 3.33: *Vapor Penetration at 1.5 ms on varying injector position and injection pressure*

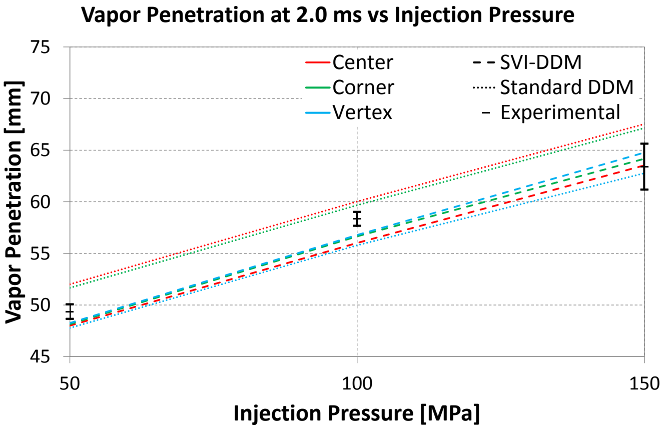

Figure 3.34: *Vapor Penetration at 2.0 ms on varying injector position and injection pressure*

3.5.7 Spray-grid mutual orientation analysis

In order to test and compare the sensitivity of the two approaches to the spray-grid mutual orientation, a new mesh was created in which the mesh elements were rotated by $45°$ with respect to the injector axis. This was done to make the parcels interacting with a mesh not-aligned with the spray. Having a mesh not aligned with the spray means that there is not a preferential lane in which the spray can evolve. This should reduce the dependency on the injector nozzle also using standard DDM approach. The aim of the analysis described in this section is to test how the two approaches react to the changed mesh orientation. In this case, changing the position from the cell center to the vertex does not make a significant variation of the cells interacting with the spray, so two new injectors positions replaced the "vertex" and "corner" cases. On this meshes, the injector was placed in the cell center as reference case and then it was moved to a face center and to an edge center (Fig. 3.35).

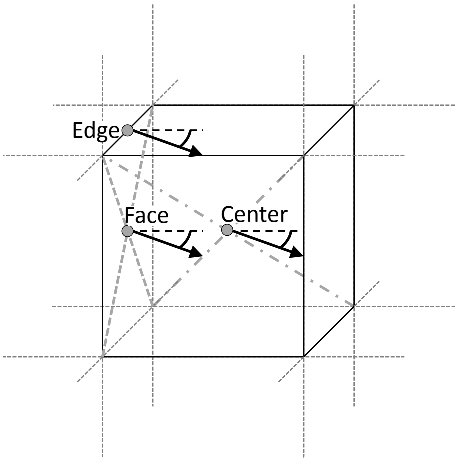

Figure 3.35: *Injection positions and directions.* $45°$ *cases*

The most critical case among the three is the "edge center" because the spray involves two planes of cells, while in the other two cases it interacts mainly with the plane containing the hosting cell and the injection axis. Figs. 3.36 to 3.37 show that using the same setup as for the baseline case, an under-estimated vapor penetration is observed for both the approaches, while liquid length is not strongly affected by the mesh orientation. The reason of this behavior could be related to the presence of a mesh-induced false diffusion [61]. Due to the orientation of the mesh cells with respect to the spray, the fluxes of the gaseous phase present a component that is normal to the injection axis and tends to enlarge the jet to the sides and to shrink it in the axial direction (see Fig. 3.38). This difference could be limited by tuning the turbulence model in order to have a reduction in the turbulent viscosity that could allow a larger fuel jet penetration or by adopting a higher order solution scheme possibly coupled with a smaller time step. Nevertheless the adoption of the SVI-DDM model resulted in a more contained variability especially in the near-nozzle region during the first phase of the injection. Indeed it is clear how the three curves are practically overlapped in the first millisecond of the injection, where the jet tip reaches a maximum penetration of 40 mm. As opposite the standard DDM approach showed divergent fuel jet penetrations since the very first part of the injection (see Fig. 3.37). Also the trend showed among the three cases is consistent with the simulations with the spray-aligned mesh. Here the edge case is the more similar to the vertex case because of the reasons explained before and as before it is the one that shows the largest penetration with SVI-DDM and the lowest with standard approach.

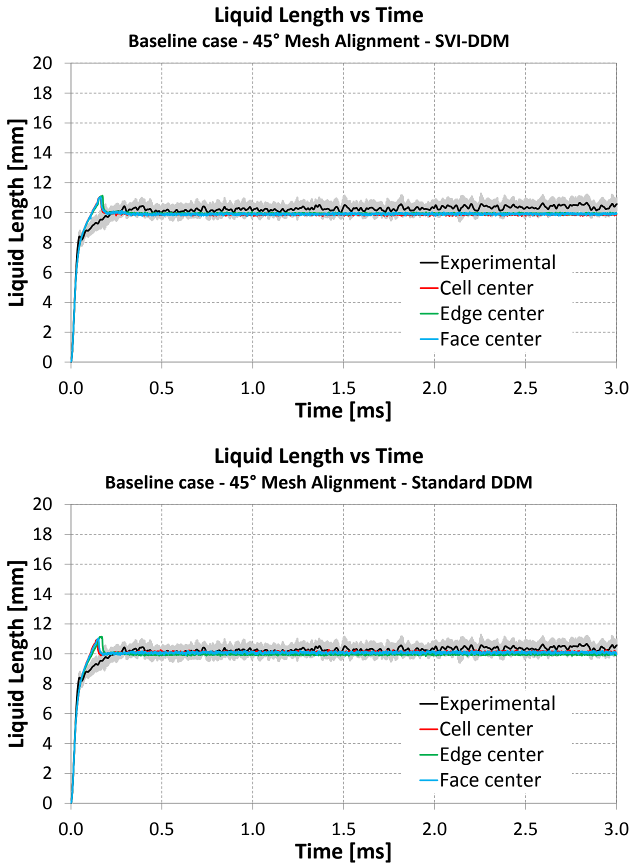

Figure 3.36: *Liquid Length on varying injector position*

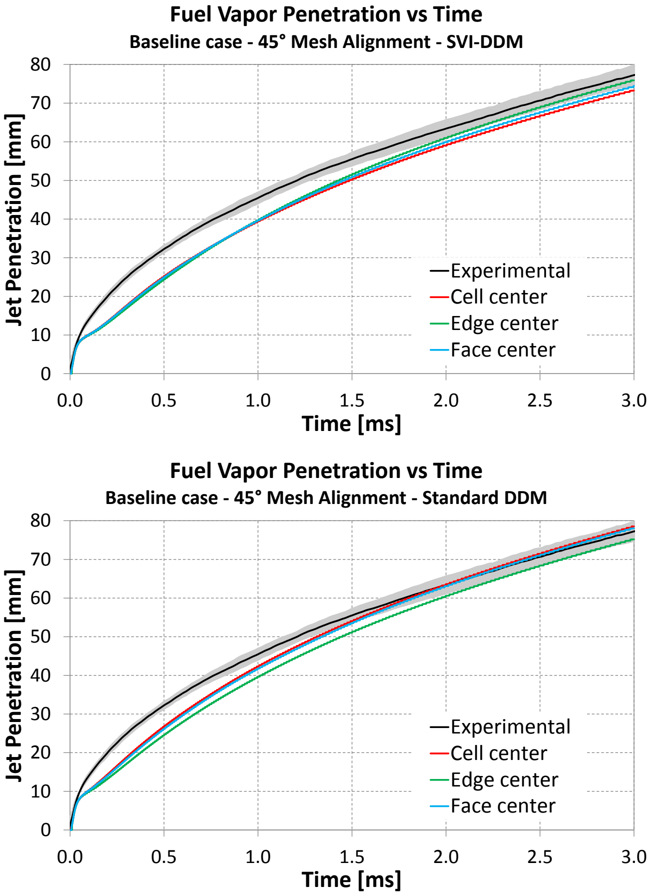

Figure 3.37: *Vapor Penetration on varying injector position*

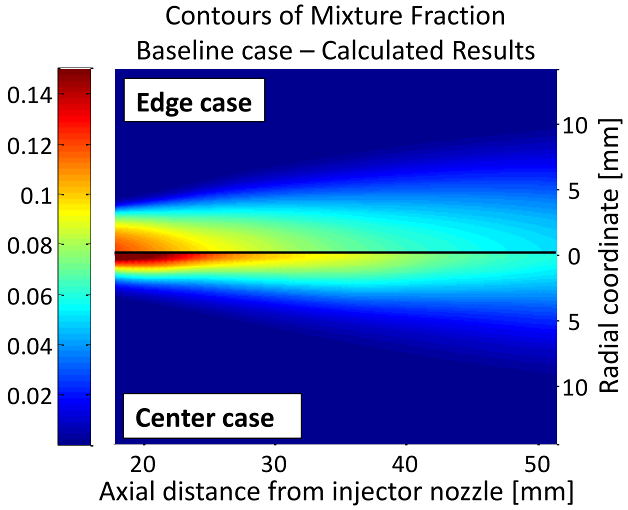

Figure 3.38: *Mixture Fraction contours. Comparison between Baseline Center and Edge cases using SVI-DDM approach*

3.6 Application on an engine geometry

The last part of this work has been dedicated to test the SVI-DDM approach on a simplified engine geometry in non-reacting conditions. The mesh was created starting from the geometry of a Cat Engine (C7.1 model). For the purposes of this study an axi-symmetrical domain was preferred hence the head details were simplified in a flat surface and a crevices volume was introduced to preserve the compression ratio. All the meshes used for this simulation were created by means of the OpenFOAM utility snappyHexMesh [62]. Starting from the beginning of the simulation every mesh has its own range of validity expressed as the crank angle interval along which the mesh is moved and deformed. Once the limit of validity of the mesh is reached, all the information contained in the Eulerian domain are mapped on the new following mesh. SnappyHexMesh is a tool that allows to create cartesian meshes automatically by means of a pre-meshed prismatic block and a surface file containing the information of the geometry. This means that the main structure of the mesh will be defined by how the block is discretized. The CFD domain will be the result of the intersection of the surface file with the block and the elements that are located on this intersection will be snapped to catch as well as possible the shape of the surface. Furthermore it is also possible to locally refine the mesh with respect to user-defined regions and surfaces. In this case the mesh was refined in the region in which the liquid spray was thought to interact with the gaseous phase in order to have a minimum mesh size of 0.5 mm. As already pointed out in Sec. 3.4.1, the choice to use this value is mainly related to the necessity to keep the number of cells in a range between two and three millions elements. Due to the size of this engine, a further refinement would have resulted in an increase in the amount of cells that was considered not acceptable for the aim of this the study. Fig. 3.39 shows half of the geometry at 10° before the TDC. It is possible to see the refinement region around the injector, furthermore the Lagrangian phase of one of the four simulated sprays is shown to give an idea of its trajectory across the domain.

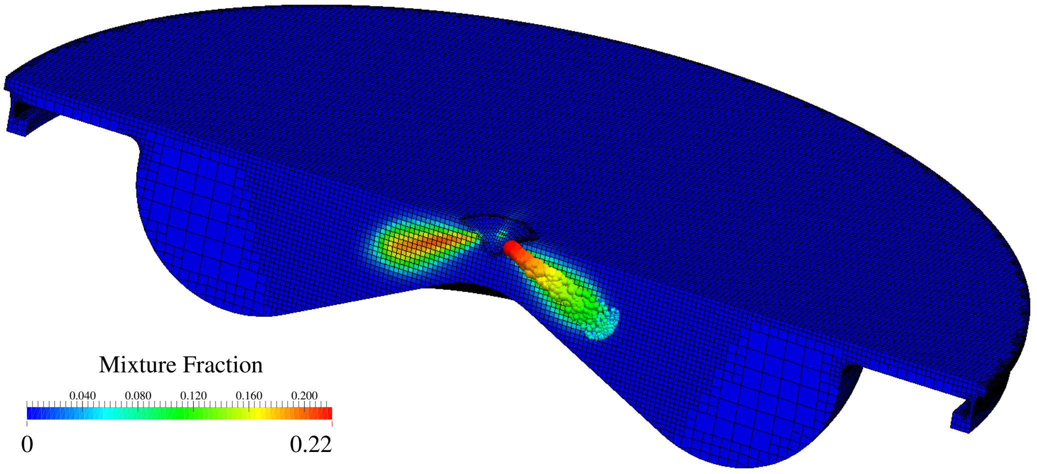

Figure 3.39: *Engine simulation. Detail of the grid*

3.6.1 Description of the simulation and results

The simulation started at the Intake Valve Closing using an experimental set of given thermo-physical initial conditions. In order to keep the axial symmetry, the flow field has been initialized neglecting the presence of any swirl motion. This means that the velocity field at the start of injection was only related to the piston motion during the compression phase. The Tab. 3.3 summarizes the main data of the engine simulation. These data were provided by Caterpillar UK Engines Company Ltd. Four nozzles were arranged along the injector tip forming an angle of 90° between each nozzle and the next. As done in part of the previous analysis on the Sandia constant volume vessel, the attention was focused on mixture fraction and gas velocity.

Engine Specification		**Fuel Injection**	
***Bore* [mm]**	**105**	***Start Of Injection* - SOI [°CA aTDC]**	**-14**
***Stroke* [mm]**	**127**	***Injection Duration* [°CA]**	**29.65**
***Engine Speed* [rpm]**	**2200**	***No. Of Nozzle Holes***	**4**
***IVC* [°CA aTDC]**	**-146**	***Nozzle Hole Diameter* [mm]**	**0.152**

Table 3.3: *Engine and injection data*

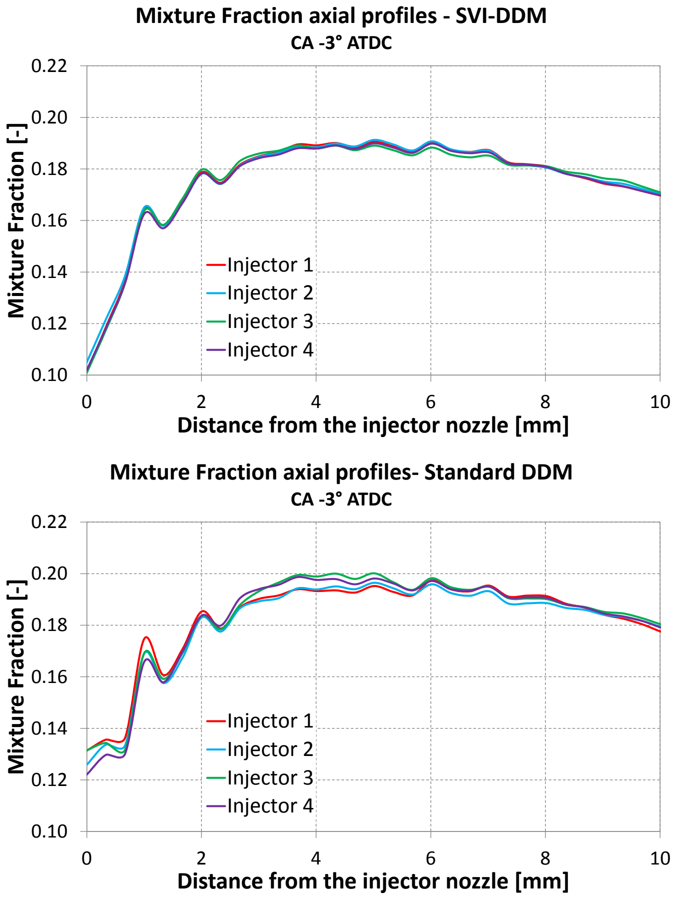

Figure 3.40: *Mixture Fraction axial profile at -3° aTDC.*

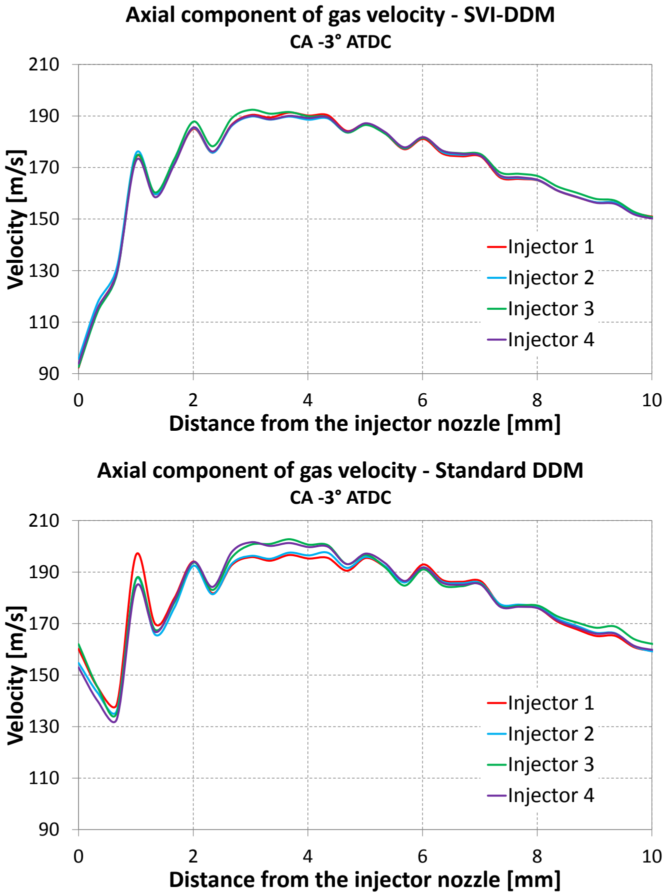

Figure 3.41: *Gas velocity along the injection axis at* -3° *aTDC.*

The graphics reported in Figs. 3.40 to 3.41 show some comparisons of the profile of evaporated fuel and axial velocity component along the centerline of every spray axis for each individual nozzle. The profiles are extracted at 3 crank angle degrees before the TDC. Due to the shape of the spray cone angle the trajectories of the liquid fuel across the domain did not follow preferential paths within the mesh. This is an advantageous condition for the standard approach for the reasons explained in Sec. 3.2 and confirmed in Sec. 3.5.7. Nevertheless Figs. 3.40 and 3.41 show how the SVI-DDM approach is able to guarantee more similar profiles in terms of mixture fraction distribution and velocity. This can be seen as a confirmation that the new model is less grid-dependent in terms of exchange of momentum and mass from the liquid to the gaseous phase. Moreover the velocity generally results a little lower in the case of the new approach as it was pointed out with the spray A results. This is probably due to the different exchange of momentum that involves more than one cell at the same time according to how the grid is intersected by the sphere. The SVI-DDM tends to diffuse momentum to the sides and consequently reduces the peak value along the injection axis. Standard DDM shows also that the predicted mixture fraction and gas velocity in the near-nozzle region strongly differs from nozzle to nozzle. This difference are almost completely canceled when the SVI-DDM is adopted.

3.7 Conclusions

A novel approach based on a spherical volume interaction between the liquid parcels and the gaseous phase was proposed and compared to the standard DDM approach for Diesel spray modeling. The main scope of the proposed contribution was to reduce the dependency of the momentum exchange between the Lagrangian and Eulerian fields on the injector location and direction with respect to the grid. Comparison with the standard approach were carried on considering both constant volume vessel experiment and a Diesel engine. Results showed a significant reduction of dependency of the liquid length penetration on the injector position in the grid cells and less evident but still appreciable improvements on the reduction of the dependency of the vapor phase morphology. For what concerns the spray/grid orientation effects, a deep investigation is required to evaluate and propose possible solutions that could allow reducing the dependency when the parcels cross the domain following a diagonal path with respect to cells alignment. The new SVI-DDM approach showed that it is able to reduce nozzle-to-nozzle dependency within the same calculation even in those cases, given that all the liquid jets are oriented in a similar fashion. Bigger differences could be surely found if different orientations should be adopted within the same calculation.

CHAPTER 4

Automatic mesh generation for full-cycle IC engines simulations

4.1 Introduction

Nowadays, multi-dimensional models are widely employed as design tools for internal combustion engines. Depending on application and objectives, different simulation types are generally performed. Steady-state conditions are modeled when new inlet port configurations have to be evaluated [63, 64] and the main interest is for flow coefficients and indexes of charge motions, like tumble or swirl numbers. When fuel-air mixing or combustion processes have to be studied, piston geometry is included in the computational domain and mesh motion is also needed [65, 66]. Depending on the engine type, a portion of the cycle or the entire one are simulated. For example, in Diesel engines with axi-symmetric piston bowl only compression, combustion and expansion phases are considered with flow field imposed at intake valve closure (IVC) time from measured or computed swirl ratio at steady-state conditions [48]. To simulate combustion or fuel-air mixture formation processes in SI engines, the full-cycle or, at least, the intake stroke needs to be included due to the higher complexity of the in-cylinder charge motions that are generated by the interaction between the incoming air jet and cylinder walls [67–69]. Currently, most of the simulations are carried out by using the RANS method with the standard $k-\varepsilon$ model and reliable approaches are available to describe both fuel-air mixing and combustion [58, 70–75]. Increase of CPU performance and massive parallelization makes possible to achieve results in a reasonable amount of time. In particular, full-cycle simulations are more and more necessary because most of the engine design process is focused on spray targeting and combustion optimization, due to the need to reduce both pollutant emissions and fuel consumption. While case setup and run are handled almost automatically with limited user operation, the main bottleneck is still represented by the mesh generation stage which requires a significant amount of time and experience for geometry processing/cleaning and to build a high-quality grid. This aspect is further worsened by modern engine combustion chambers due to the complex shapes of valves, piston bowl, ports and cylinder head. To generate a grid, conventional programs offer a pre-processing interface where it is possible to import the CAD geometry in surface or volume format. Afterwards, the user manually cleans the geometry, creates several volume blocks inside it and generates a proper mesh for each block. Once the first template grid is done, specific tools are available to create the entire necessary set to complete the full-cycle simulation. Due to the large involvement of manual user work in mesh generation stage, several critical issues might arise that negatively affect the quality of the results. Among them, we can mention the capability to maintain similar mesh structure, size and quality for the different configurations to be tested. Possible, fully automatic alternative solutions exist. Initially, semi-automatic methods were proposed in [76] and currently applied up to these days. Automatic tetrahedral mesh generation was employed in [77, 78] using the Delaunay algorithm. Such approach is very fast and allows to generate high-quality grids. However, it has several drawbacks related to the numerical diffusion induced by a non flow-oriented mesh structure, very high number of cells, computational efficiency and difficulty in creating boundary layers on valve wall boundaries. Recent examples of the use of fully tetrahedral grids for IC engine simulations can be found in [79, 80]. An alternative approach is represented by Cartesian, cut-cell grids as it was described in detail in [81]. Such methodology has been successfully applied over the years to simulate gas exchange, fuel-air mixing and combustion both in Diesel and GDI engines [82–84]. There, the engine mesh is generated from the surface geometry and a Cartesian mesh. Cells outside the geometry are removed and intersecting cells are cut to fit to the boundary geometry by introducing additional faces. To capture most of the geometry details of ports, valves and combustion chamber, local refinement is also included close to the boundaries of interest. Cartesian cut-cell grids are computationally very efficient and also very accurate because of their very low non-orthogonality. However, prediction of charge motions can be negatively affected by the absence of boundary layers on the valve wall boundaries and also numerical interpolation errors might arise due to the need to regenerate the computational mesh at each time-step. This last aspect also introduces a non-negligible computational overhead. In this work, a novel approach for automatic generation of engine grids was developed using the OpenFOAM technology and implemented into the LibICE code. Such technique was then incorporated in the methodology developed by the Polimi ICE group over the years for full-cycle engine simulations [67, 85, 86], where the entire cycle is simulated by using a multiple number of deforming grids, each one valid within a certain crank angle interval. In the proposed approach, the user has to provide only the combustion chamber geometry in surface file format with piston at top dead center (TDC) and valves at minimum arbitrary lift. Surface points are then moved to positions corresponding to the start time of the simulation and a Cartesian, body-fitted grid-generator creates the first mesh which is automatically moved until quality parameters are satisfied or maximum validity interval is covered. At this stage, a new grid is generated and both mesh motion and automatic mesh generation steps are sequentially performed until the entire set of grids is created. The proposed approach employs the utility available in the Open-

FOAM code, called *snappyHexMesh*, generating automatically 3D meshes containing hexahedra and split-hexahedra from triangulated surface geometries in Stereolithography (STL) format. Advantages of such utility are represented by the possibility to insert boundary layers on wall surfaces and local refinements in regions of interest. *snappyHexMesh* allows grid generation in parallel with a consequent reduction of the pre-processing time required. To test the proposed technique for mesh generation and handling, an entire engine cycle was simulated for the TCC engine. The choice of such geometry was justified by several aspects. First, geometry and experimental data are publicly available through the Engine Combustion Network database, making such experiment a common basis for comparing different CFD approaches for mesh management and turbulence modeling. Furthermore, the layout of the valves is quite critical when Cartesian-based grids are employed, since the flow enters into the cylinder with approximately a 45° orientation with respect to the mesh structure. Hence, an accurate numerical setup needs to be defined to properly predict the gas flow. Finally, a large amount of experimental data of in-cylinder velocity field and turbulence is available, making a comprehensive validation of the proposed methodology possible.

4.2 Mesh management

In the proposed approach for CFD simulation of IC engines a multiple number of meshes is employed, so that each mesh is valid in a certain crank angle interval and during it the grid points are moved and the grid topology is eventually changed. Consistent interpolation of the computed flow field from one mesh to the next one is performed by means of a second-order, *inverse distance weighting* method (with escapes for exact hit) [49].

4.2.1 Mesh Motion

An automatic mesh motion technique was developed to accommodate the displacement of internal grid points according to the prescribed boundary motion [85, 87]. The Laplace equation is solved with the Finite Volume method for the cell centers velocity field $\mathbf{U}_C$ with constant or variable diffusivity γ:

$$\nabla \cdot (\gamma \nabla \mathbf{U}_C) = 0 \tag{4.1}$$

The grid point velocity field $\mathbf{U}_P$ is computed by extrapolation from $\mathbf{U}_C$ and used to modify the point positions:

$$\mathbf{x}_{new} = \mathbf{x}_{old} + \mathbf{U}_P \Delta t, \tag{4.2}$$

Eq. 4.1 is solved with boundary conditions represented by the prescribed boundary motion. To further preserve the mesh quality during motion it is also possible to specify mesh-motion for an arbitrary number of points in pre-defined regions before solving the motion equation. The developed mesh motion technique is flexible with respect to the mesh structure, supporting unstructured polyhedral cells of arbitrary shapes. This is quite important when direct-injection engines have to be simulated, since their complex geometry usually require combination of hexahedra and tetrahedra in regions where high deformations takes place.

4.2.2 Automatic mesh generation

Figs. 4.1 - 4.2 summarize the methodology developed in this work for automatic mesh generation. The process is intended to ensure high quality grids according to the following user specified parameters:

- maximum validity interval for each mesh, to avoid excessive stretching of the cells and loss of resolution;
- maximum allowed mesh non-orthogonality and skewness values, to increase stability and simulation accuracy [50];
- Topological and geometrical validity of the mesh [88].

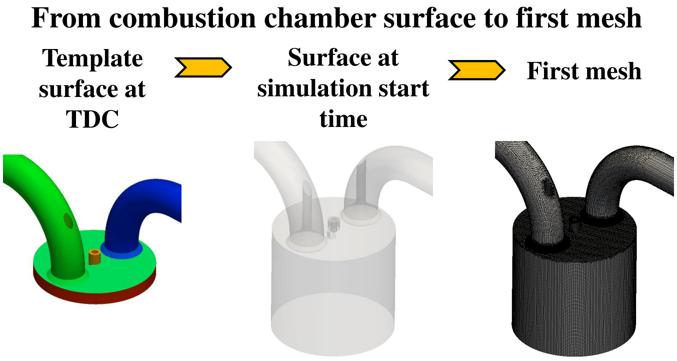

Figure 4.1: *Generation of the first mesh from surface geometry of the combustion chamber*

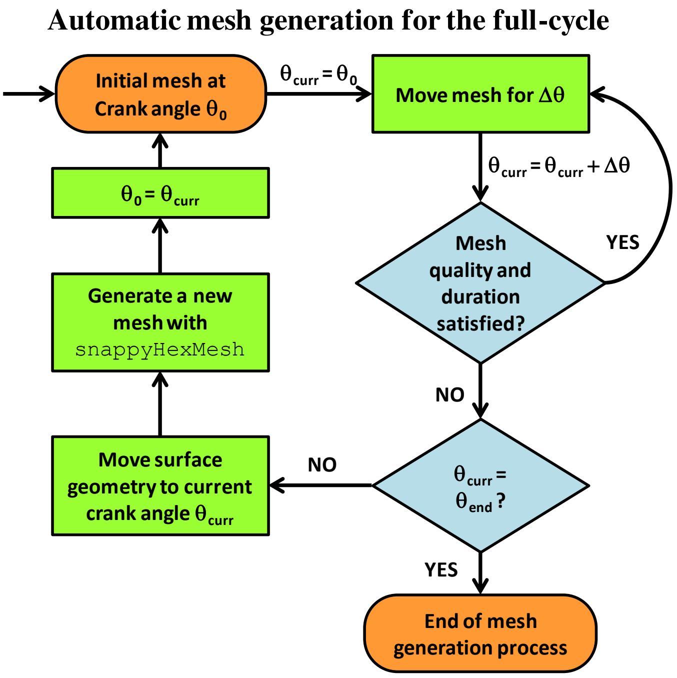

Figure 4.2: *Automatic mesh generation process*

At the end of the process, an entire set of meshes satisfying the listed criteria will be created and can be used for gas exchange, fuel-air mixing and combustion simulations.

Initially, the user has to provide a cleaned surface of the combustion chamber where all the boundaries of interest (piston, valve poppet, valve bottom, liner, cylinder head, valve stem, inlet, outlet, ...) are identified with a proper name. Only stereolithographic formats are supported. Piston must be located at TDC and valves at minimum lift, usually ranging in the 0.1 - 0.25 mm interval. A proper utility moves automatically both piston and valves at positions corresponding to the crank angle where the simulation is started. At this stage, the first mesh is automatically generated and then it is moved using the automatic mesh motion technique and solving the Laplace equation with a fixed, user-specified time-step ranging from 0.1 to 0.25 CAD. The mesh is continuously deformed until duration, quality and validity criteria are satisfied. As soon as one of these fails, the combustion chamber surface geometry is moved to the current crank angle and a new mesh is generated. This process is sequentially performed until the end of the simulation is reached.

4.2.3 Mesh generation tool

The *snappyHexMesh* method available in OpenFOAM differs from the traditional way of doing pre-processing for CFD. This method uses automatic procedure to create orthogonal hexahedral mesh either around or inside a given geometry surface, which has to be provided in stereolithographic format. In principle this method enables fast and robust meshing of complex geometries. In this work, *snappyHexMesh* was applied to generate engine meshes and here its operation is shortly described and summarized in Figs. 4.3(a) - (c).

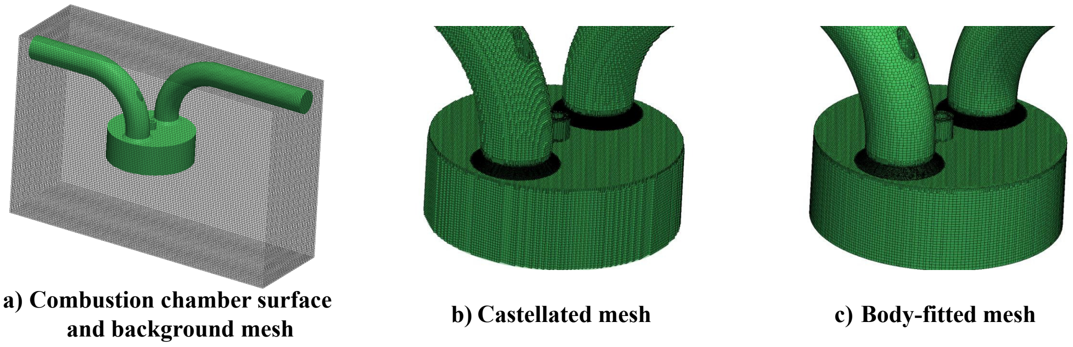
a) Combustion chamber surface and background mesh

b) Castellated mesh

c) Body-fitted mesh

Figure 4.3: *Application of the snappyHexMesh tool to engine mesh generation*

Initially, a block-structured grid has to be provided and its size represents the initial mesh density. On the basis of the geometry to be meshed and user-specified settings, the so-called *castellated mesh* is created by removing all the cells outside the combustion chamber, as it can be seen in Fig. 4.3(b). Close to boundaries or in regions of particular interest, the castellated mesh can be further refined either for a better matching of the real geometry or to properly predict phenomena of interest such as incoming gas flow, flame kernel growth or air-fuel mixture formation. An iterative procedure, controlled by maximum specified non-orthogonality and skewness values, will be then used to morph the castellated mesh to the combustion chamber surface. The final result of the procedure is shown in Fig. 4.3(c), displaying a body fitted mesh conforming to surface boundaries and properly accounting for the main geometry details including sharp edges.

The optional possibility to insert boundary layers on surfaces of interest was also exploited for the valve boundaries in order to better predict the flow entering into the cylinder. Details of the mesh generation process in the valve region, from castellated to body fitted mesh with boundary layers are illustrated in Fig. 4.4.

Since it is not possible to model the contact between valve poppet and cylinder head, the following procedure was used: the valve is considered to be closed when its lift is lower than a minimum value (range is 0.1 - 0.25 mm). At that points, a new mesh is created and baffles are automatically introduced to physically separate the cylinder and port domains.

snappyHexMesh runs in parallel and operates a load balancing step every iteration. Both these aspects make mesh generation process very fast and guarantee an optimal domain decomposition for the subsequent gas flow simulations.

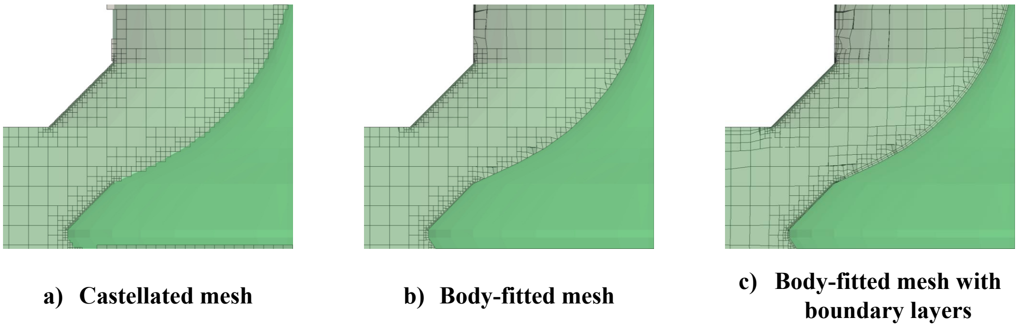
a) Castellated mesh **b) Body-fitted mesh** **c) Body-fitted mesh with boundary layers**

Figure 4.4: *Application of the snappyHexMesh tool to generate body-fitted meshes with boundary layers in the valve region*

4.2.4 Mesh quality indexes

Using a finite volume method with deforming grids, the computed solution is strongly affected by mesh size and quality, which are continuously changing due to domain volume variation induced by moving boundaries. A significant work about mesh quality metrics was performed in the past [89] where different shape and size quality indexes were defined, but they cannot be easily extended to polyhedral grids and are only valid for tetrahedral and hexahedral cells. In [50], Jasak showed that discretization accuracy of the finite volume method depends on the mesh skewness and non-orthogonality.

An example of non-orthogonal mesh is displayed in Figure 4.5a(a). The mesh *non-orthogonality* is defined for a face as the angle α between the face area vector (**S**) and the vector joining the cell centers sharing the same face (**PQ**). Non-orthogonality affects the discretization accuracy of the diffusion term in transport equations [50, 90]. In industrial CFD simulations non-orthogonal meshes are commonly used to account for complex geometry features. However, if $\alpha > 80$ the non-orthogonality is considered severe and requires to limit or discard the non-orthogonal component of the diffusion term and to increase the number of non-orthogonal correctors [50]. $\alpha \geq 90$ is an index of mesh invalidity since this happens with degenerate cells.

The grid *skewness* error reduces the accuracy of face integrals to the first order [50] when the interpolated face value does not lie in the its center as shown in Fig. 4.5a(b).

The skewness parameter for a face is defined as:

$$\text{skewness} = \frac{||\mathbf{m}||}{||\mathbf{PQ}||} \tag{4.3}$$

Where the vector **m** is the distance between the face center and the intersection between the face area and the vector **PQ**. As for non-orthogonality, skew meshes are rather common in IC engine simulations mainly when tetrahedra are used. Skewness can be considered severe when it is higher than 4. However, values lower than 10 can be still considered acceptable.

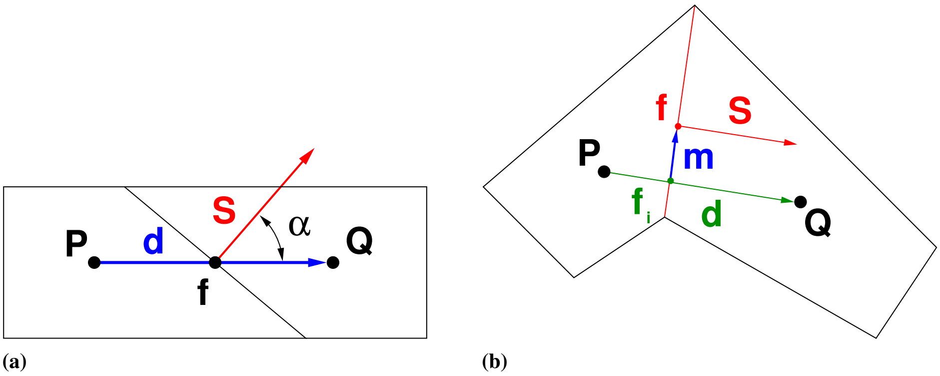

(a) (b)

Figure 4.5: *Examples of a non orthogonal (a) and a skew mesh (b)*

4.3 Results and discussion

4.3.1 Sandia TCC Engine

The proposed approach was assessed and validated by means of experiments carried out in a Transparent Combustion Chamber (TCC) engine. In it a two-valve head and a pancake combustion chamber were adopted mainly to perform experiments about the nature of stochastic flows in internal combustion engines [91–93]. This aspect justified the simplified geometry layout which was intended to generate a turbulent flow in the cylinder by means of the interaction between the incoming gas jet, piston and liner walls. Most of the studies on this engine were used to assess and develop sub-grid models for Large Eddy Simulations [94–96], while to the authors' knowledge no RANS simulations were carried out on such geometry so far. The engine layout is displayed in Figs. 4.6 (a) - (b), Table 4.1 illustrates the main geometry data and valve lift profiles and phasing are displayed in Fig. 4.7.

The overall optical access is maximized to allow acquisition of three-dimensional in-cylinder flow field for a proper investigation of near-wall, boundary layer flows. Experimental data are acquired with optical multi-dimensional high-speed diagnostics techniques. In particular, macro- and micro-PIV techniques were used for flow measurements, which can be set up to cover the full 86 mm stroke of the engine. Furthermore, zoomed-in measurements allow spatial resolutions below 50 mm. Data were recorded every 5 CAD for 70 cycles, allowing a very detailed characterization of the average in-cylinder flow-field and related fluctuations.

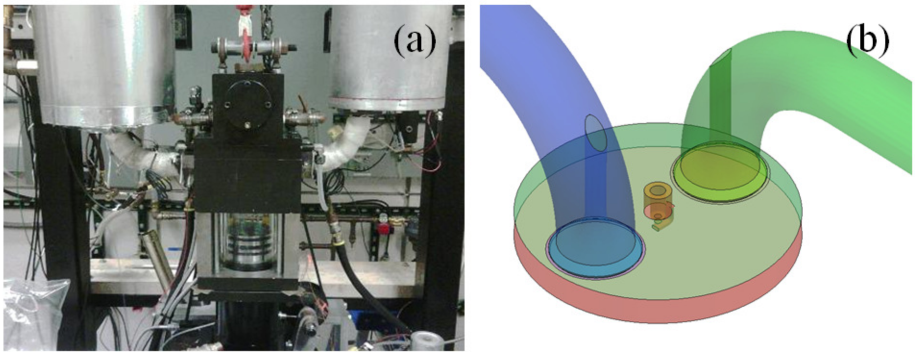

Figure 4.6: *SANDIA TCC engine layout: (a) engine at test-bench; (b) combustion chamber geometry*

Bore	92 mm
Stroke	86 mm
Connecting Rod Length	244 mm
Compression Ratio	10
IVO	359°
IVC	592°
EVC	364°
EVO	131°
Speed	800 rpm
Valve diameters	30 mm
Maximum valve lift	8.9 mm

Table 4.1: *Summary of engine geometry data and simulated operating conditions*

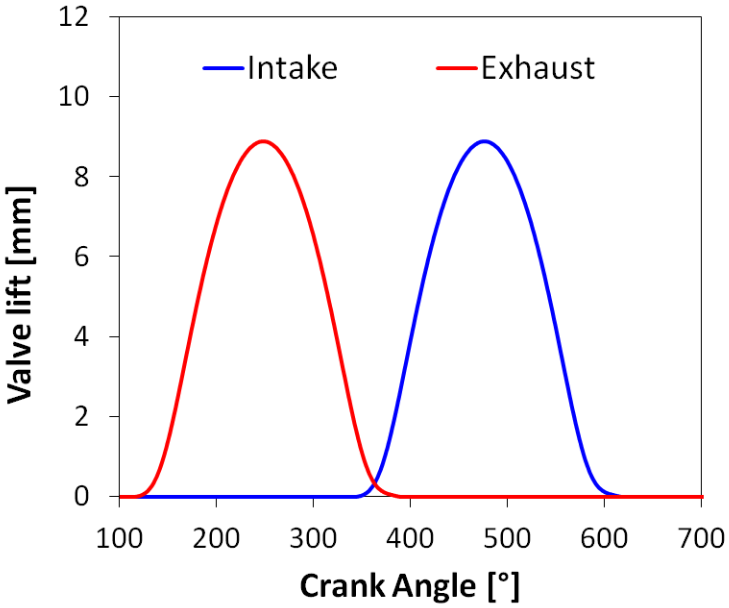

Figure 4.7: *Intake and exhaust valve lift profiles of the TCC engine.*

4.3.2 Methodology assessment

The performances of the proposed approach for automatic mesh generation were first tested in terms of number of required grids and required CPU time. Such investigation was carried out using the following parameters for the grid generation process:

- 2 mm mesh size inside cylinder and ports;
- local refinement up to 0.125 mm close to cylinder head, piston, liner and valve boundaries;
- additional refinement box below the cylinder head with a 1 mm size.

The corresponding mesh sizes are approximately 600 thousand and 1.5 million cells at TDC and BDC, respectively. More details about the mesh structure are displayed in Figs. 4.8 (a) - (b) where it is also possible to see that the spark-plug geometry was included in the computational domain.

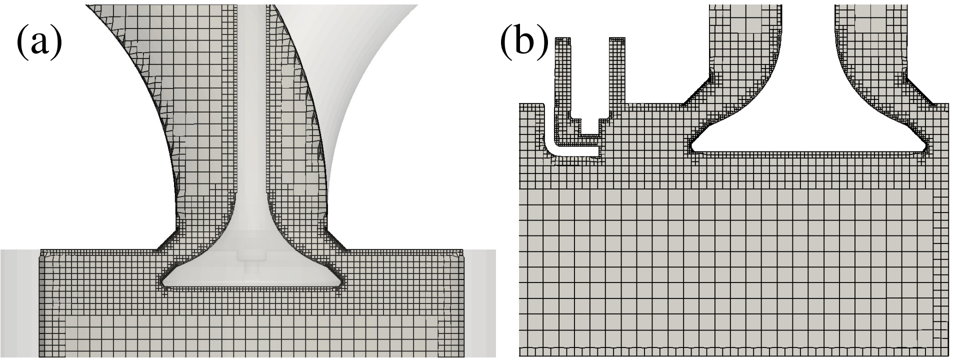

Figure 4.8: *Mesh structure used for the TCC engine simulation: (a) inlet port and valve region; (b) cylinder symmetry plane*

Grid generation process starts from EVO, where the full-cycle simulation begins. Effects of non-orthogonality on the mesh generation process were evaluated, by setting that during motion grids maintain both their topological and geometrical validity, allowing a maximum non-orthogonality of 90° and avoiding negative face areas. With such constrains, average mesh duration is approximately 10 CAD and the cumulative mesh count as function of crank-angle is reported in Fig. 4.9 where it is possible to see that mesh validity mainly depends on how the adopted finite-volume algorithm is affected by cylinder mesh deformation, valve motion and interaction between piston and valves. In particular, grid compression combined with valve motion during exhaust stroke requires a higher number of grids (33 vs 25) compared to the intake phase, where cylinder mesh is expanded. Compression stroke requires less grids, due to the absence of valve motion. Mesh count drastically increases during valve overlap around IVC since in such conditions mesh validity is strongly worsened by piston-valve interaction and high deformation of small cells on the top of the valves. Compression and expansion phases requires much lower grids, due to the absence of valve motion.

Fig. 4.10 illustrates how the cumulative mesh count is affected by maximum allowed non-orthogonality, with tested values in the 70-90° range. When generated, each mesh has an initial maximum non-orthogonality of 60 degrees. As expected, when reducing

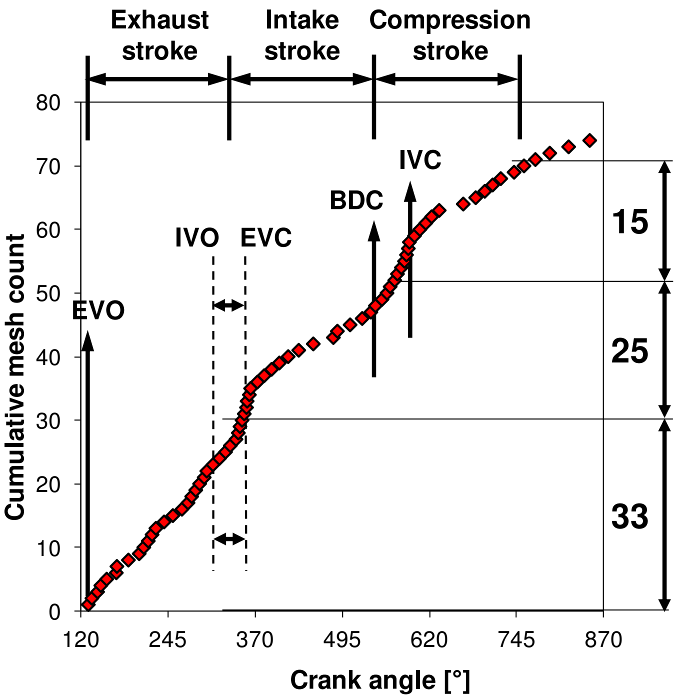

Figure 4.9: *Cumulative mesh count for the mesh generation process, limited only by topological and geometrical validity of each mesh*

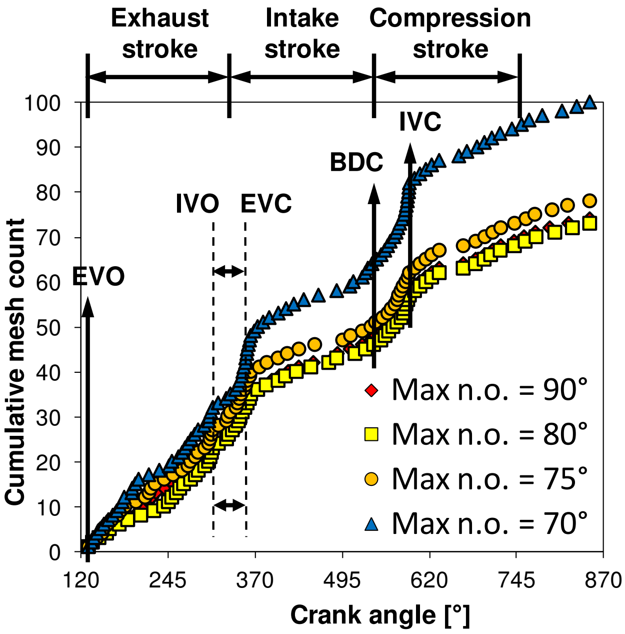

Figure 4.10: *Effect of maximum allowed non-orthogonality on the mesh generation process*

the maximum allowed non-orthogonality during motion, the total number of required meshes grows. However, such increase takes place mainly during valve overlap and IVC periods, while the number of grids required for intake, compression and exhaust phases remain almost unchanged. This aspect can be drastically seen when maximum mesh non-orthogonality is reduced from 75 to 70 degrees. Since charge motions and turbulence are mainly generated during the intake stroke, introducing more grids in the other parts of the cycle is expected to increase the computational time but not the quality of the results. For this reason, grid generation process based on maintaining topological and geometrical validity of the mesh was adopted in this work.

Finally, Fig. 4.11 illustrates performance of the grid generation process when run on multiple CPU. The single processor case was not considered due to the large size of the meshes involved. Mesh generation and simulations were run on an AMD 64 cores machine, with 4 processors and 4 GB RAM for each core. For what concerns the scalability of the process, it is possible to see that a good speed-up factor is achieved until 12 cores are used. With a higher number of them, overheads introduced by the continuous need to redistribute the meshed domain across the different processors compensates the increase of available computational resources. On 16 cores the entire mesh generation process takes approximately 8 hours (including the required pre-processing) which is significantly less than what is generally needed to create manually just the first template mesh.

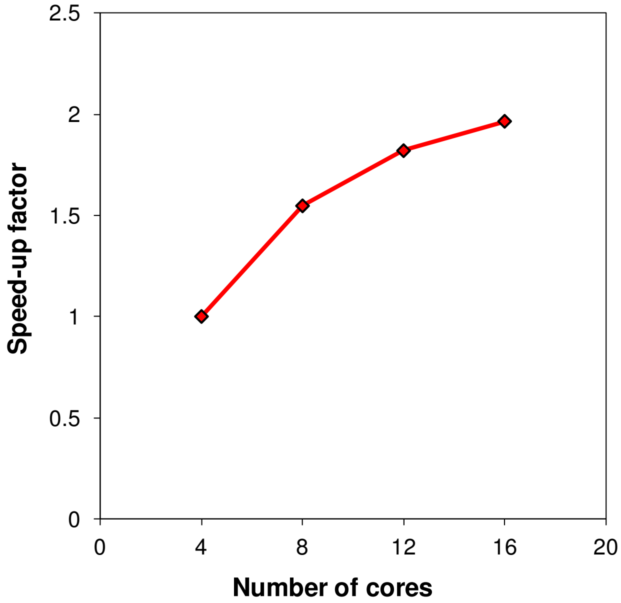

Figure 4.11: *Parallel performance of the mesh generation process*

4.3.3 Experimental Validation

Full-cycle simulations of the TCC engine were carried out to validate the proposed approach. The simulated domain is shown in Fig. 4.12 where it is possible to see that the entire combustion chamber (including spark-plug) and part of intake and exhaust manifolds were included in the computational mesh. On the inlet and outlet boundaries, experimental time-varying total pressure and temperature profiles were imposed. In Fig. 4.13 it is possible to see the typical behavior of pressure waves in a single cylinder engine operating at non-fired conditions. The standard turbulence $k - \varepsilon$ model was used with 5% turbulence intensity at the inlet and the integral length equal to 10% of the manifold diameter. Coefficients used for the turbulence model are listed in Tab. 4.2.

Validation was mainly carried out to understand the validity of the proposed setup

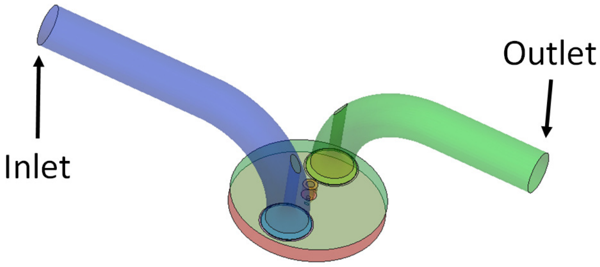

Figure 4.12: *Simulated computational domain*

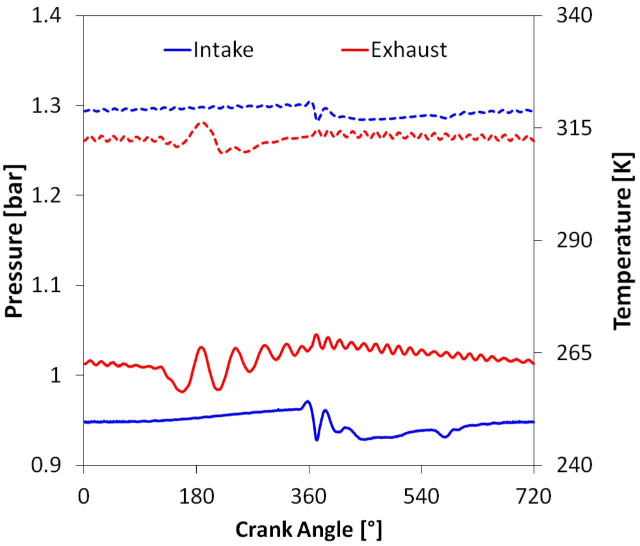

Figure 4.13: *Evolution of pressure (solid) and temperature (dashed) on the inlet (blue) and outlet (red) boundaries for an engine cycle*

C_μ	C_1	C_2	C_3	α_h	α_k	α_ε	Pr_t
0.09	1.44	1.92	-0.33	1	1	0.769	0.85

Table 4.2: *$k - \varepsilon$ model coefficients used in this work*

in terms of boundary conditions and number of used meshes and to see if the Cartesian grid orientation could be used to properly reproduce the in-cylinder flow field. This aspect is rather critical for the simulated engine, since the flow enters the cylinder with approximately a 45° orientation with respect to the mesh structure. Under such conditions, numerical diffusivity plays a big role and might lead to a wrong prediction of flow field, charge motions and turbulence. To this end, three different simulation setups were considered as displayed in Tab. 4.3, representing a combination of mesh sizes and numerical methods. Two different grids were used which mainly differ in the mesh structure close to the valves, as illustrated in Fig. 4.14 (a) - (b): the second mesh has an additional refinement region close to the valves with a 0.25 mm size. This increases the number of cells, up to 1.3 at TDC and 1.7 millions at BDC. Numerical diffusivity is expected to have a much higher influence on the results with the coarser meshes than the fine meshes. To understand how numerical methods influence the computed flow-field and if the meshes are all robust enough to support high-order methods, both first and second-order schemes for space discretization were tested on the fine mesh.

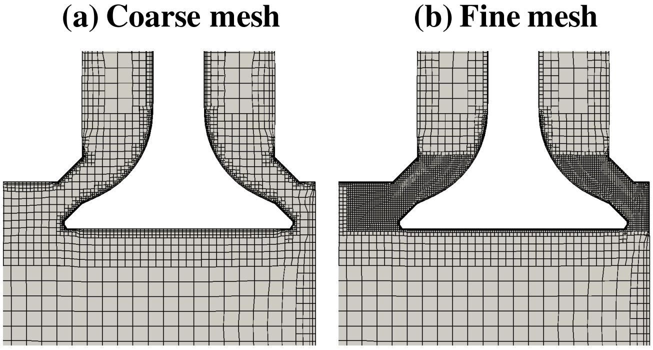

Figure 4.14: *Comparison between the structures adopted for the two tested mesh configurations: (a) coarse mesh; (b) fine mesh*

Case	Mesh	Numerical Method
1	Coarse	First order
2	Fine	First order
3	Fine	Second order

Table 4.3: *Simulation setup in terms of mesh size and numerical schemes adopted for the TCC engine*

In order to achieve the convergence of results in terms of computed velocity field in both manifolds and cylinder for each crank angle, two engine cycles were simulated. The validity of the proposed setup in terms of mesh to mesh interpolation, geometry discretization and imposed boundary conditions was verified by comparing in Fig. 4.15 computed and experimental data of in-cylinder pressure profiles.

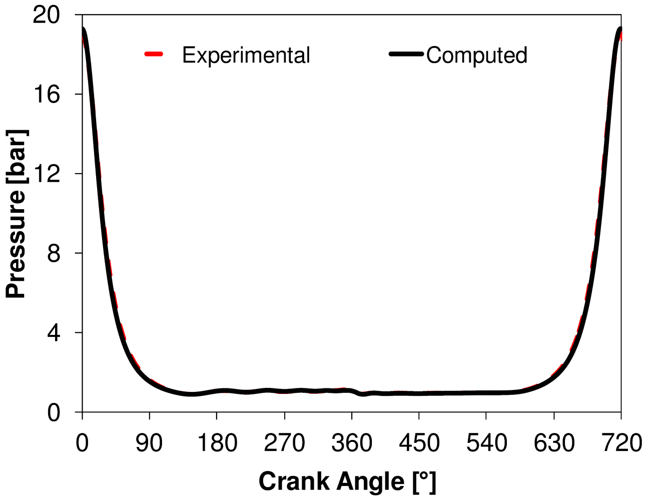

Figure 4.15: *Comparison between computed and experimental cylinder pressure profiles for the full cycle under motored conditions*

A proper matching was achieved, showing that trapped cylinder mass is correctly predicted at the end of the gas-exchange process. Furthermore, a rather good agreement between experimental and computed pressure values was achieved during the intake stroke, meaning that losses in both inlet manifold and valves are properly reproduced.

Once the setup was verified, comparisons between computed and experimental data of in-cylinder flow fields were carried out. In particular, measured data were available in a 26 mm width x variable height window, located in a plane passing through the inlet valve axis and parallel to the cylinder symmetry plane. Both measured velocity vectors and magnitude were available as well as the distribution of the turbulence intensity. Fig. 4.16 shows the exact location of the measurement window inside the cylinder.

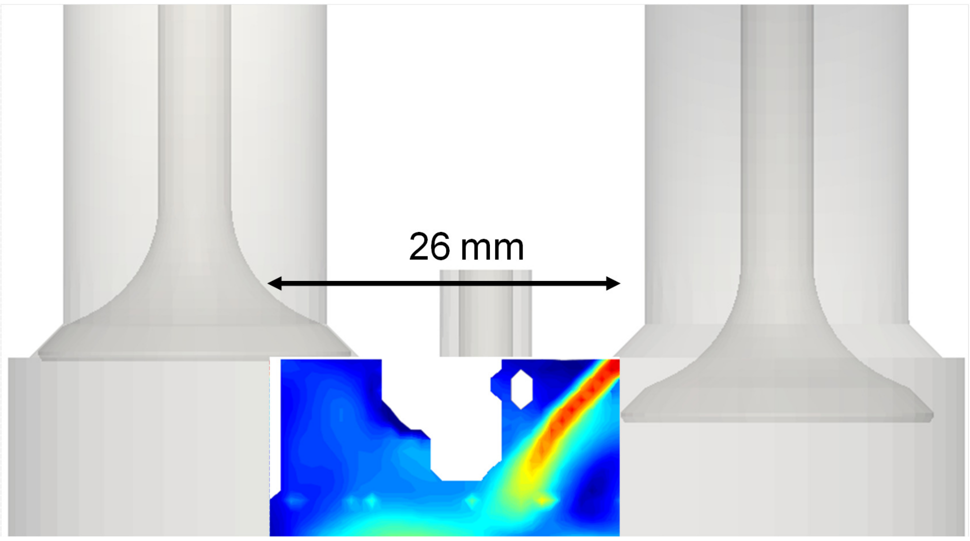

Figure 4.16: *Location of the optical window used for flow field and turbulence measurements*

Effects of mesh size and numerical accuracy were evaluated at different times during intake and compression stroke and flow field results were then compared with experimental data. For what concerns the intake phase, the following instants were considered:

- 370 CAD: beginning of intake phase where high velocities are expected because of small valve lift ($\sim$ 1.5 mm);
- 410 CAD: inlet valve at mean lift ($\sim$ 4.9 mm) and piston at maximum acceleration;
- 450 CAD: inlet valve at almost lift and piston at maximum velocity;
- 490 CAD: inlet valve at mean lift ($\sim$ 4.9 mm) and piston at maximum deceleration;
- 540 CAD: inlet valve at mean lift ($\sim$ 4.9 mm) and piston at bottom dead center (zero velocity);
- 590 CAD: inlet valve closure time.

To validate the proposed methodology, a detailed comparison between computed and experimental data of in-cylinder velocity and turbulence intensity distributions was carried out for the selected crank angles. Experimental instantaneous velocities were recorded on two different windows, parallel to both cylinder and valve axes. The first window provides detailed information about the incoming flow in the cylinder. It has a 40.6 x 62.8 mm size, with a corresponding grid of 52 x 80 points equally spaced. The second measurement window is larger (74 x 115.7 mm) than the first one, but it has a lower resolution (same number of points: 52 x 80) and provides an overview of the overall cylinder flow field. Interpolating computed data at exact measurement locations and accounting only for projected values on the optical windows ensure a consistent validation with experimental data. Here, some details about the post-processing technique are briefly described. Experimental velocity magnitude in each point of the measurement plane is computed from the average of its horizontal and vertical components as follows:

$$\overline{U}\left(x,y,\theta\right)=\frac{1}{N_c}\sqrt{\left(\sum_{i=1}^{N_c}U_{x,i}\left(\theta\right)\right)^2+\left(\sum_{i=1}^{N_c}U_{y,i}\left(\theta\right)\right)^2} \tag{4.4}$$

where N_c is the total number of cycles where velocity data were recorded. For each experimental velocity component, corresponding turbulence intensities are estimated as:

$$u'_x\left(x,y,\theta\right)=\frac{1}{N_c}\sum_{i=1}^{N_c}\left(\overline{U}_x\left(x,y,\theta\right)-U_{x,i}\left(x,y,\theta\right)\right)^2 \tag{4.5}$$

$$u'_y\left(x,y,\theta\right)=\frac{1}{N_c}\sum_{i=1}^{N_c}\left(\overline{U}_y\left(x,y,\theta\right)-U_{y,i}\left(x,y,\theta\right)\right)^2 \tag{4.6}$$

where $\overline{U}_x$ and $\overline{U}_y$ are the average horizontal and vertical components of velocity, respectively. Experimental turbulence intensity is computed for u'_x, u'_y, estimating the corresponding turbulent kinetic energy first and then computing the corresponding average turbulence intensity u'_{exp} as follows:

$$k_{exp}=\frac{1}{2}u'^2_x+\frac{1}{2}u'^2_y \tag{4.7}$$

$$u'_{exp}=\sqrt{k} \tag{4.8}$$

For a consistent comparison between experimental and computed data, calculated velocity field is interpolated at measurement locations with an inverse-distance weighted interpolation technique [49], then its magnitude is computed taking only the projection of the velocity vector on the measurement plane into account. Computed turbulence intensity u'_{calc} is estimated from turbulent kinetic energy k_{calc} interpolated at measurement locations as follows:

$$u'_{calc}=\sqrt{\frac{2}{3}k_{calc}} \tag{4.9}$$

Figs. 4.17 (a) - (d) report a comparison between computed and experimental velocity distributions at 370 CAD. At the beginning of the intake stroke, there is still significant vortex located below the exhaust valve originating from the exhaust stroke as it can be seen in Fig. 4.17(a). None of the simulated configurations predicts correctly the intensity and shape of that vortex. because of the rather coarse mesh below the exhaust valve. A small vortex also appears on the left of the inlet valve and his presence is properly reproduced by all the tested configurations as it can be seen in Figs. 4.17 (b) - (d) where also no significant differences between used meshes and numerical setup were found. However, the predicted vortex size is smaller than the experimental one and this might be due to the choice of using a minimum valve lift of 0.25 mm, which might limit the air inflow to the cylinder at the beginning of the inlet stroke.

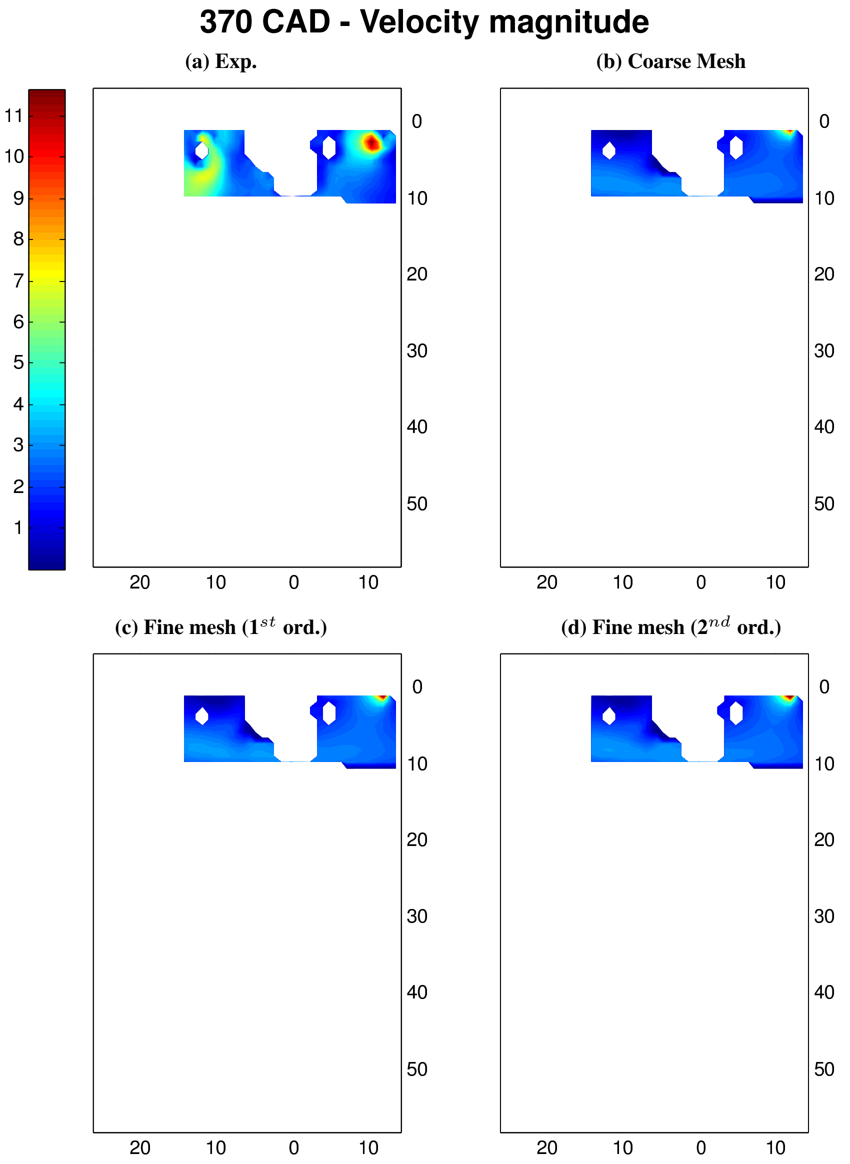

Figure 4.17: *Comparison between computed and experimental velocity magnitude distribution at 370 CAD. Units are in [m/s], scale is 0 (blue) - 11 m/s (red)*

During the first part of the intake stroke, the typical gas jet structure is established at the valve entrance, in particular Fig. 4.18 illustrates that experimentally there is still not interaction between gas flow and piston. The shape of jet is correctly predicted when the fine mesh is used, either with first or second order schemes as it can be seen in Figs. 4.18(c) - (d). Instead, Fig. 4.18(b) shows that numerical diffusion due to either first order schemes or coarse mesh induces a non-physical deviation of the jet towards the cylinder liner in the horizontal direction. However, accurate numerical schemes are necessary to properly predict jet penetration, while first order schemes makes the jet larger and shorter.

410 CAD - Velocity magnitude

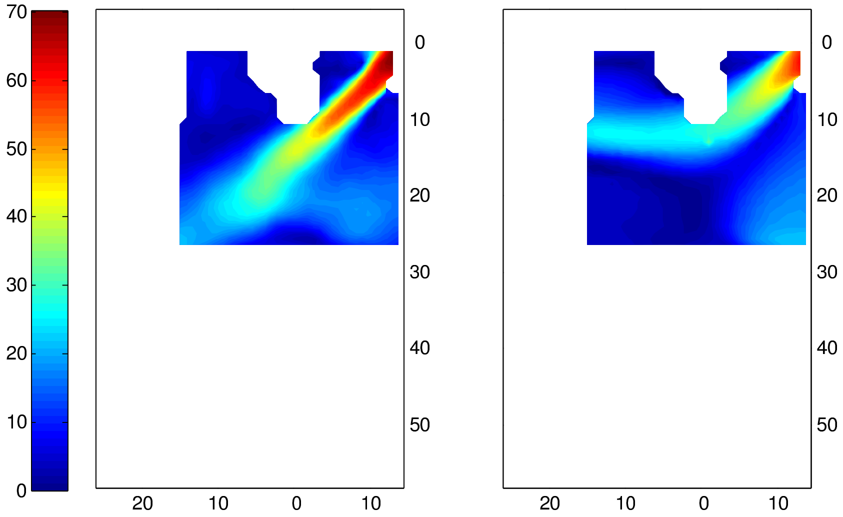

(a) Exp.

(b) Coarse Mesh

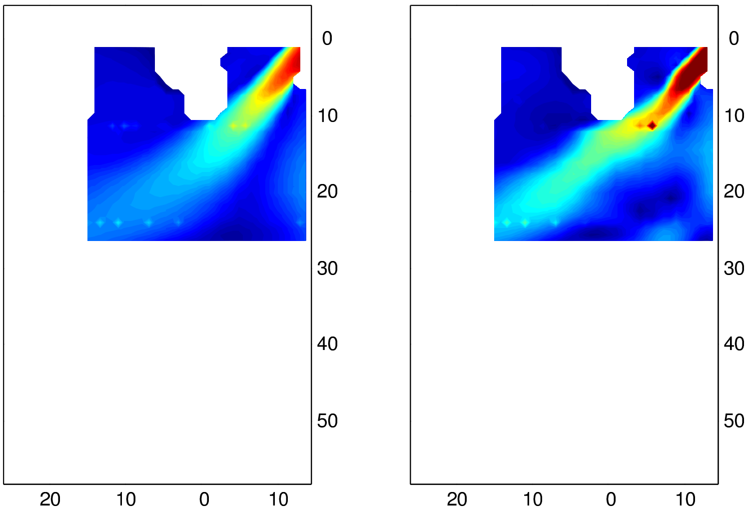

(c) Fine mesh (1^{st} ord.)

(d) Fine mesh (2^{nd} ord.)

Figure 4.18: *Comparison between computed and experimental velocity magnitude distribution at 410 CAD. Units are in [m/s], scale is 0 (blue) - 70 m/s (red)*

A comparison between velocity vector distribution in the measurement plane is shown in Fig. 4.19(a) - (d). In particular, when comparing Figs. 4.19(a) and (d) it is possible to see that also the slight deviation of the jet due to interaction between the incoming flow and the spark-plug is properly described and this demonstrates the need to include such detail in the computational mesh.

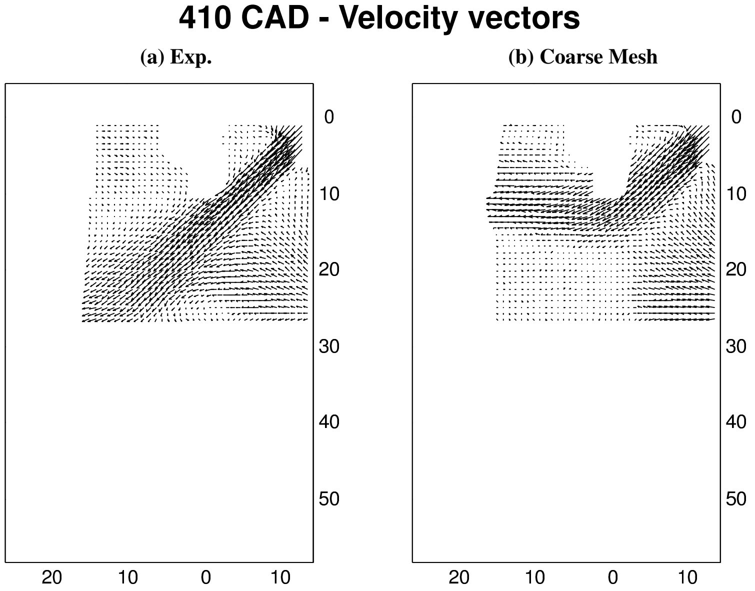

(a) Exp.

(b) Coarse Mesh

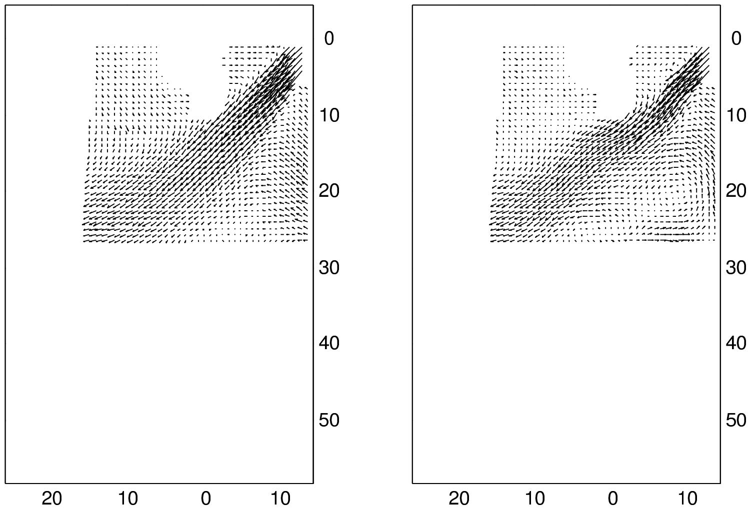

(c) Fine mesh (1^{st} ord.)

(d) Fine mesh (2^{nd} ord.)

Figure 4.19: *Comparison between computed and experimental velocity vectors at 410 CAD*

For what concerns the turbulence levels inside the cylinder, in Fig. 4.20 experimental intensity looks at this time much higher than computed data. Only the fine mesh with second order schemes seems to be able to predict non negligible turbulence levels inside the cylinder with a distribution similar to experimental data. However, at 410 CAD predicted in-cylinder turbulence might be also affected by the residual flow originated during the exhaust phase where a coarse mesh was used.

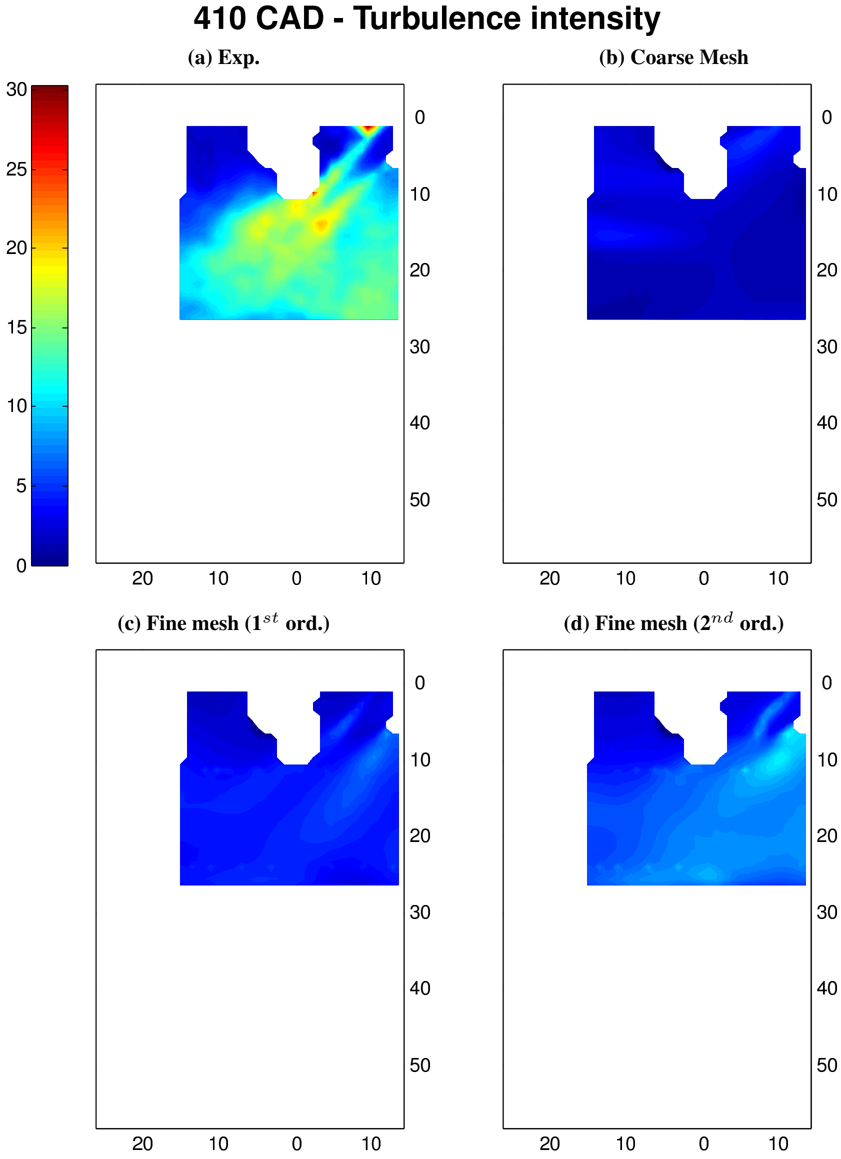

Figure 4.20: *Comparison between computed and experimental turbulence intensity distribution at 410 CAD. Units are in [m^2/s^2], scale is 0 (blue) - 30 m^2/s^2 (red)*

Figs. 4.21(a) - (d) report a comparison between computed and experimental velocity magnitude at 450 CAD, where piston velocity is maximum and for this reason a significant amount of air is sucked inside the cylinder. Jet penetration is rather well predicted by fine meshes, with second order schemes being also able to better reproduce the velocity distribution inside the jet. For what concerns the jet shape, experimental data show a slight vertical deviation at his periphery which is not properly estimated during the simulations.

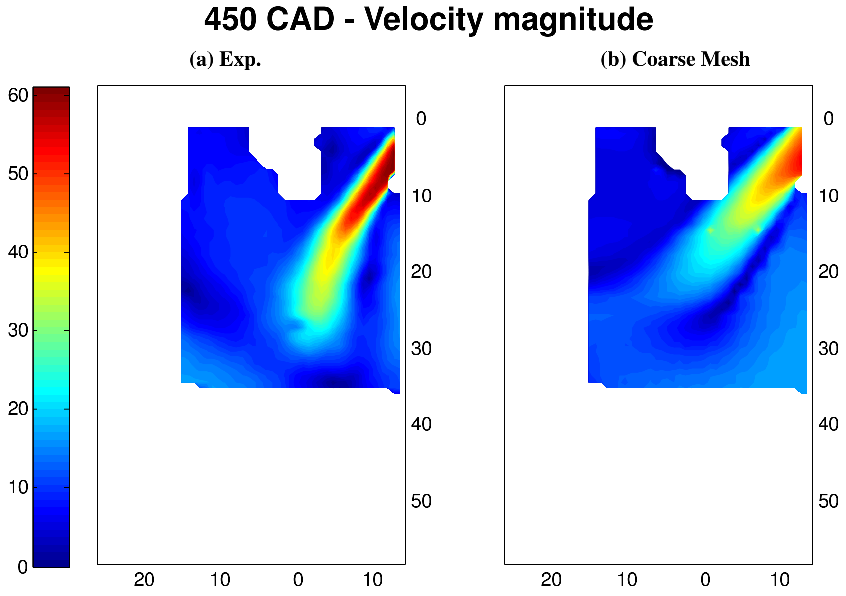

(a) Exp.

(b) Coarse Mesh

(c) Fine mesh (1^{st} ord.)

(d) Fine mesh (2^{nd} ord.)

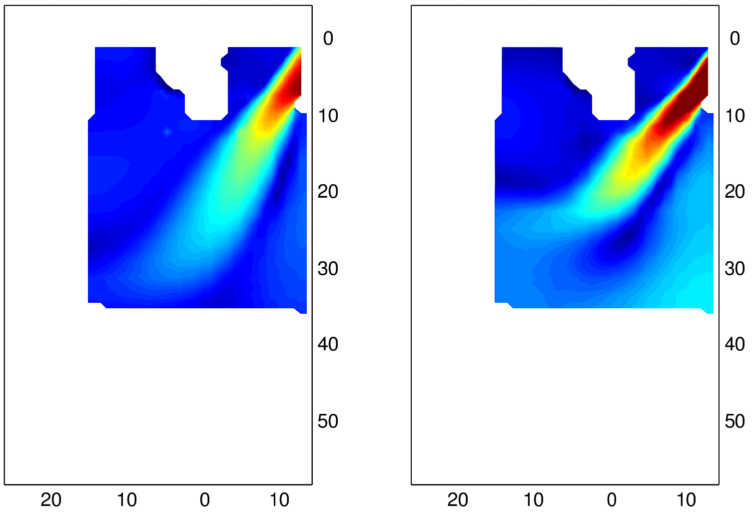

Figure 4.21: *Comparison between computed and experimental velocity magnitude distribution at 450 CAD. Units are in [m/s], scale is 0 (blue) - 60 m/s (red)*

To better understand such difference, Fig. 4.22 compares experimental and computed velocity vectors with second order schemes and fine mesh.

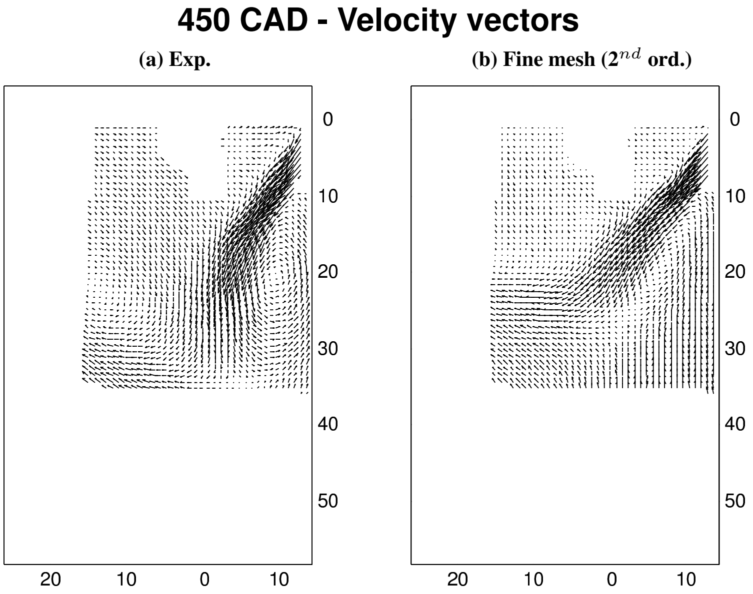

Figure 4.22: *Comparison between computed and experimental velocity vectors at 450 CAD: (a) Experimental data, (b) Fine mesh with second order schemes*

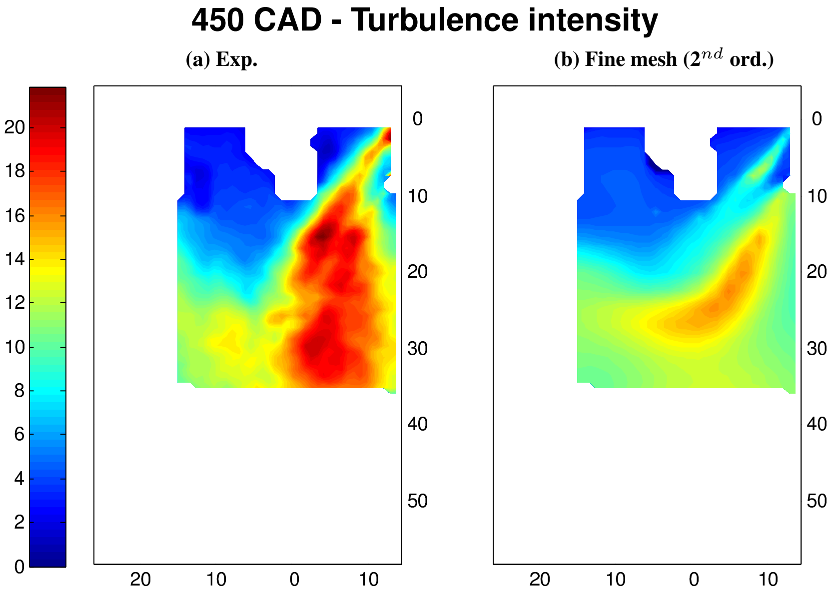

Figure 4.23: *Comparison between computed and experimental turbulence intensity distribution at 450 CAD: (a) Experimental data, (b) Fine mesh with second order schemes. Units are in [m^2/s^2], scale is 0 (blue) - 20 m^2/s^2 (red)*

From Fig. 4.22(a) it is possible to see that, experimentally, the gas jet deviation is mainly due to the circular vortex originated at the bottom of the valve and moving downwards. Such vortex also exists in simulations, but it is more elongated and for this reason it is not able to properly deviate the incoming cylinder flow. It is possible that this discrepancy can be affected by two different aspects: the first is the grid size below the valve, being 1 mm and probably not refined enough to reproduce the development of the vortex originated by the shear flow at valve exit. Turbulence model might also play a role, producing a limited viscosity that makes the jet more straight than what effectively it is. However, when looking to predicted turbulence levels in Fig. 4.23, they are comparable with experimental values and for this reason mesh structure below the valve might be the reason for the differences between experimental and predicted shapes of the gas jets at 450 CAD.

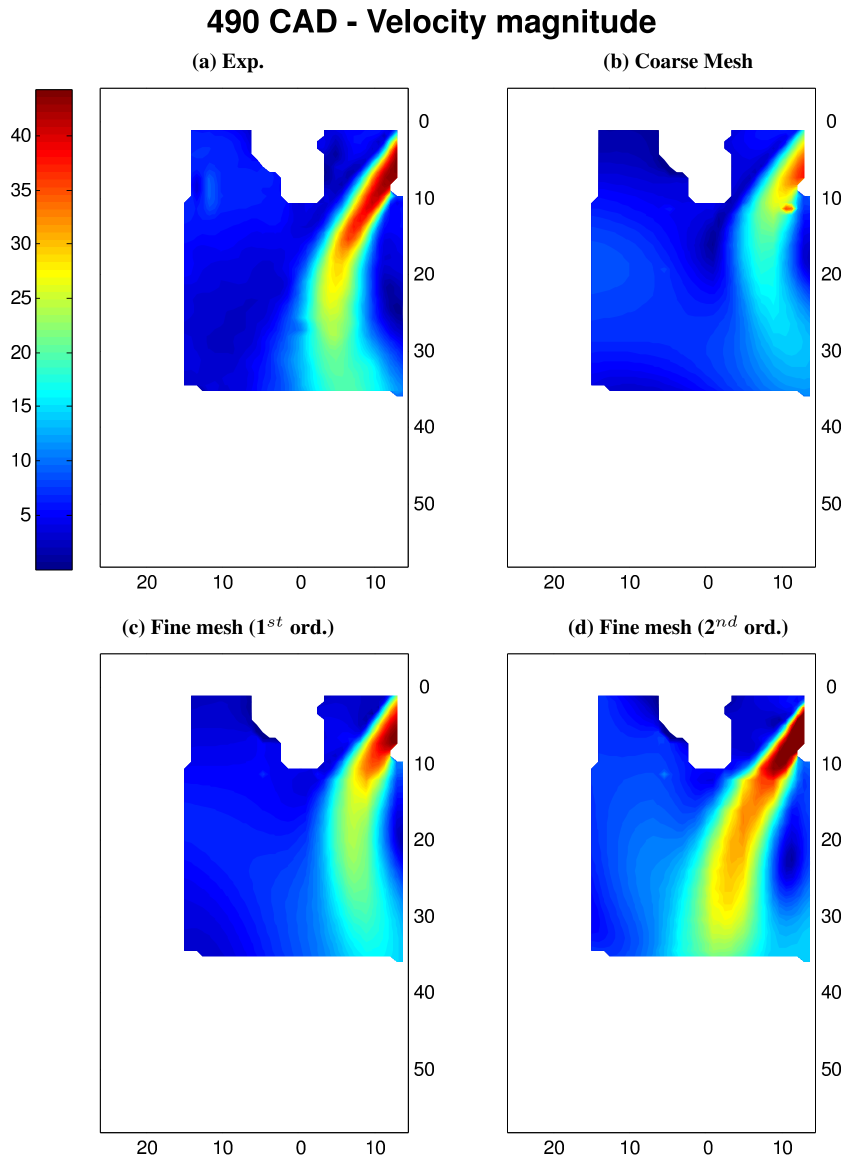

Figure 4.24: *Comparison between computed and experimental velocity magnitude distribution at 490 CAD. Units are in [m/s], scale is 0 (blue) - 40 m/s (red)*

When moving towards the second part of the intake stroke at 490 CAD, it is possible to see in Fig. 4.24(a) that the jet enlarges due to air entrainment. Due to interaction with the vortex created below the valve, the jet maintains its round distortion. All the tested setup were able to qualitatively describe the shape of the jet but the coarse grid predicts a very low penetration, while the fine mesh with first order schemes estimates a reduced jet enlargement downwards. Results with fine mesh and second order schemes shown in Fig. 4.24(d) are in acceptable agreement with experimental data. When looking at Fig. 4.25, comparing experimental velocity vectors and computed ones with second-order schemes it is possible to see that now the round vortex located the bottom-right part of the window is well-established in simulations while it starts to decay in measured data.

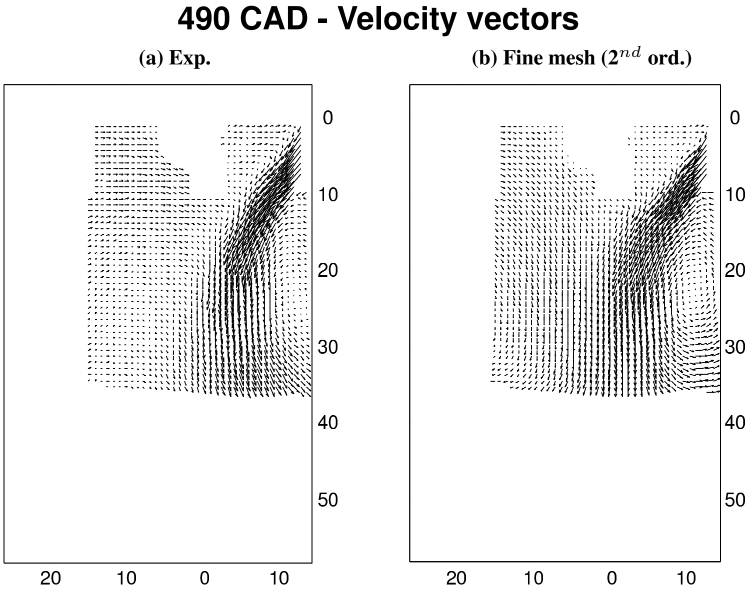

Figure 4.25: *Comparison between computed and experimental velocity vectors at 490 CAD: (a) Experimental data, (b) Fine mesh with second order schemes*

For what concerns the turbulence distribution inside the cylinder, an interesting aspect is shown in Fig. 4.26(a). The large amount of turbulence found in the bulk of the cylinder seems to be mainly originated by the shear flow that exists the valve outlet. Turbulent kinetic energy originates at the cylinder head and valve edges, diffuses into the air jet so that a large region of high turbulence intensity is created. In simulations, again mesh structure seems to be responsible for a not correct prediction of the turbulence distribution as it can be seen in Fig. 4.26(b). In particular, a fine mesh in the top of the valve generates a significant amount of turbulence while coarse mesh in the bottom of the valve is not able to properly capture velocity gradients there and the related turbulence generation.

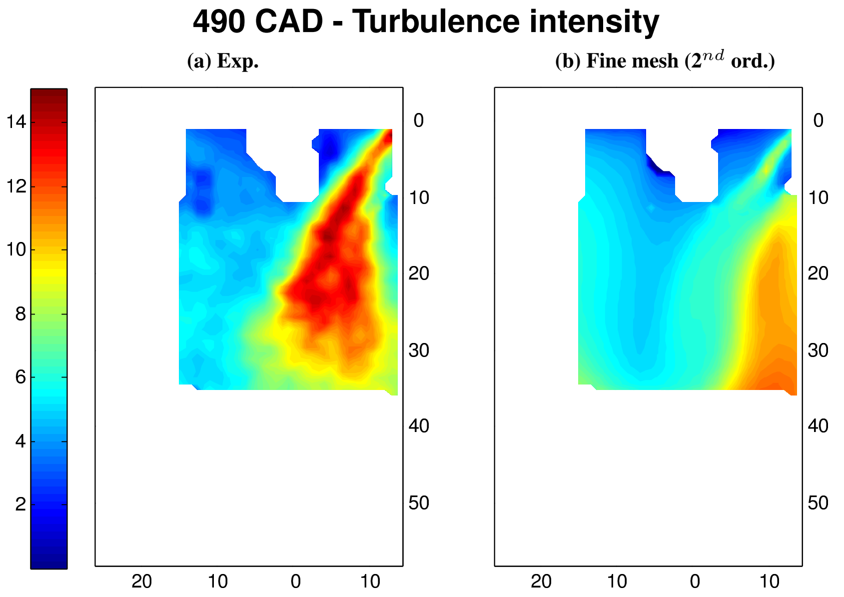

Figure 4.26: *Comparison between computed and experimental turbulence intensity distribution at 490 CAD: (a) Experimental data, (b) Fine mesh with second order schemes. Units are in [m^2/s^2], scale is 0 (blue) - 14 m^2/s^2 (red)*

To better understand experimental results at BDC, Figs. 4.27 and 4.28 display the measured velocity field evolution during the second part of the intake stroke, in the 450-540 CAD range.

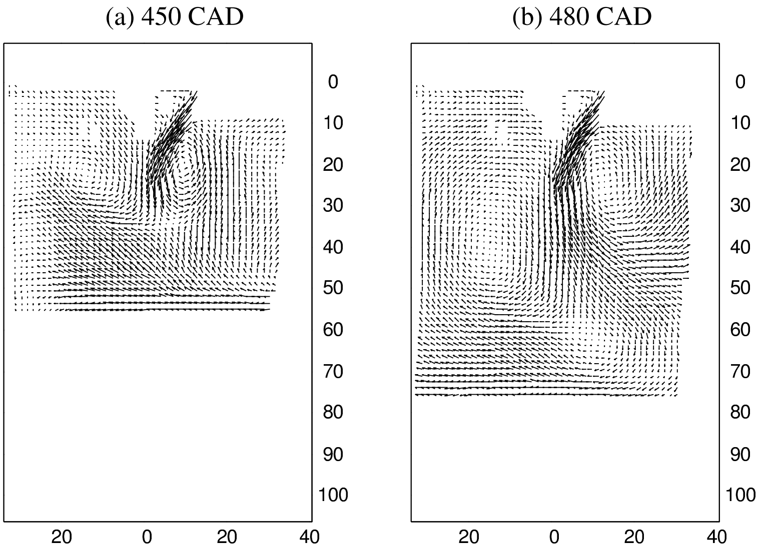

Figure 4.27: *Experimental evolution of in-cylinder velocity field in the 450-480 CAD interval*

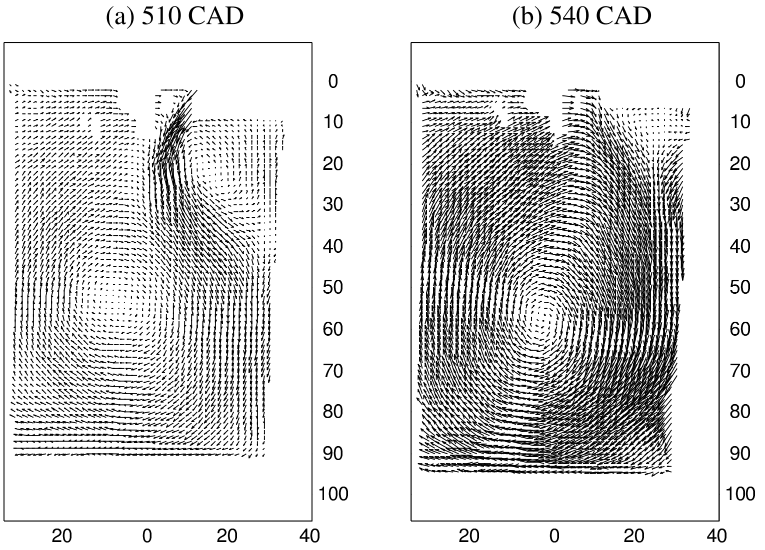

Figure 4.28: *Experimental evolution of in-cylinder velocity field in the 510-540 CAD interval*

Despite not completely visible in the images, the jet that enters from the other side of the intake valve has a significant influence on the in-cylinder flow. It strongly interacts with the cylinder liner and then it moves towards the piston and flows over it already at 450 CAD (Fig. 4.27(a)). This is the condition for the creation of a sort of vortex which remains located in the bottom part of the cylinder and it is also enhanced by the incoming air jet. At BDC, Fig. 4.28(b) shows that such vortex is almost located in the center of the cylinder and it has a major influence in the velocity distribution.

Mesh size and turbulence model are expected to play a big role in the prediction of the in-cylinder flow at BDC due to the presence of the large vortex inside the cylinder. To this end, a comparison between computed and experimental velocity magnitude contours is displayed in Fig. 4.29. Care is necessary for a detailed analysis of the computed data since misleading conclusions can be drawn: at a first sight results achieved using a coarse grid with 1^{st} schemes look much better than the others. To better understand the differences between the numerical setup used, the development of the in-cylinder flow on a larger window is illustrated in Figs. 4.30 4.31 in the 450-540 CAD range. In particular, velocity contours are shown for the coarse mesh with first order schemes and the fine mesh with second order schemes.

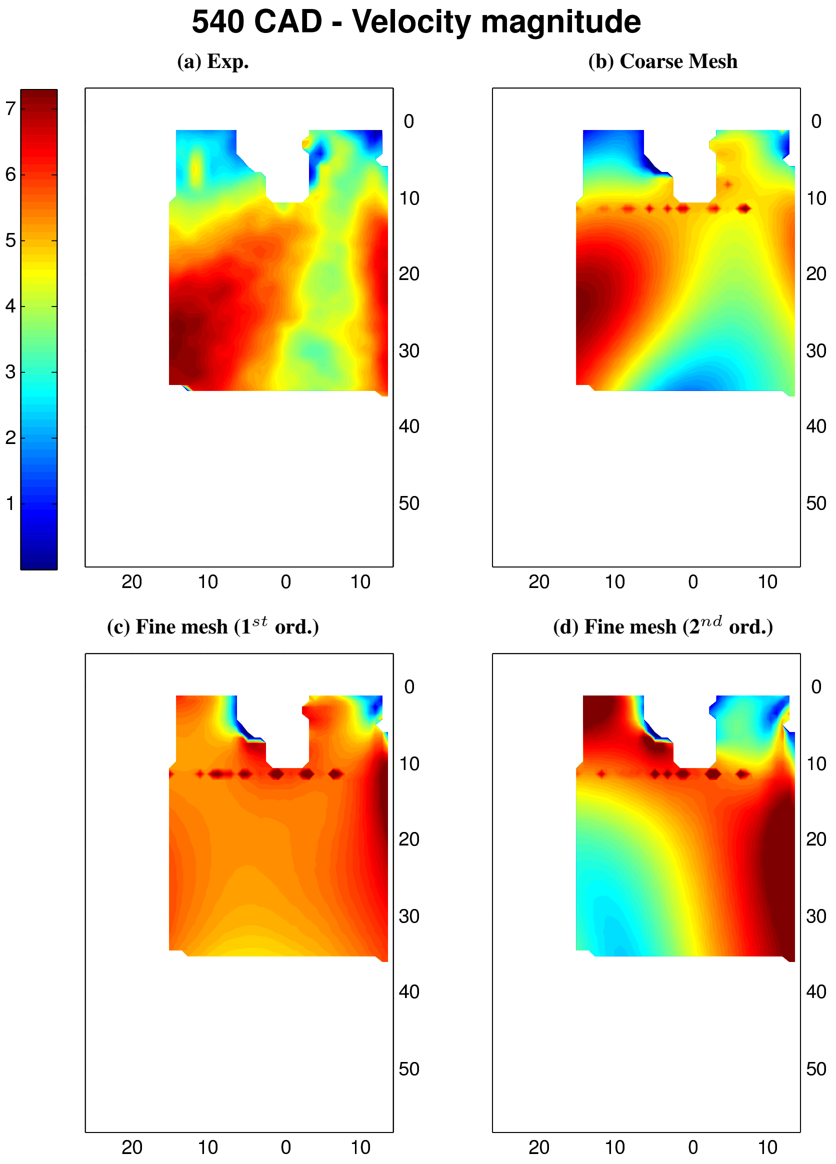

Figure 4.29: *Comparison between computed and experimental velocity magnitude distribution at 540 CAD. Units are in [m/s], scale is 0 (blue) - 7 m/s (red)*

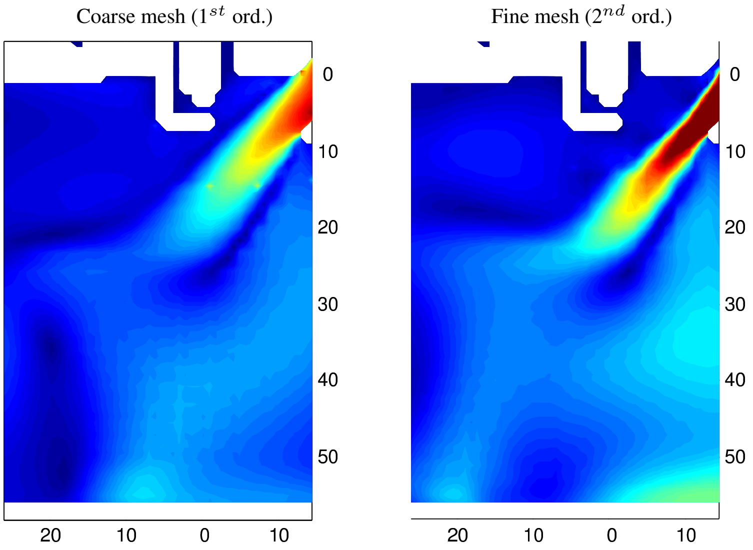
(a) 450 CAD

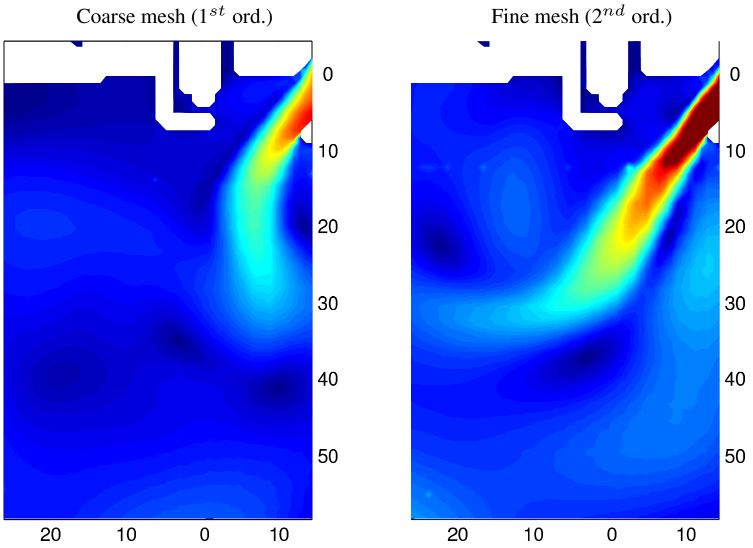
(b) 480 CAD

Figure 4.30: *Comparison between computed velocity contours using coarse mesh with 1st order schemes (left) and fine mesh with 2nd order schemes during the second part of the intake stroke (450-480 CAD)*

(a) 510 CAD

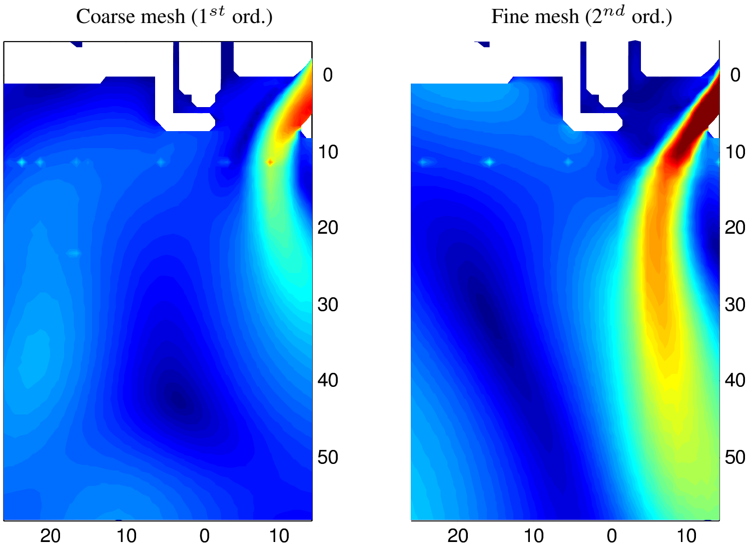

(b) 540 CAD

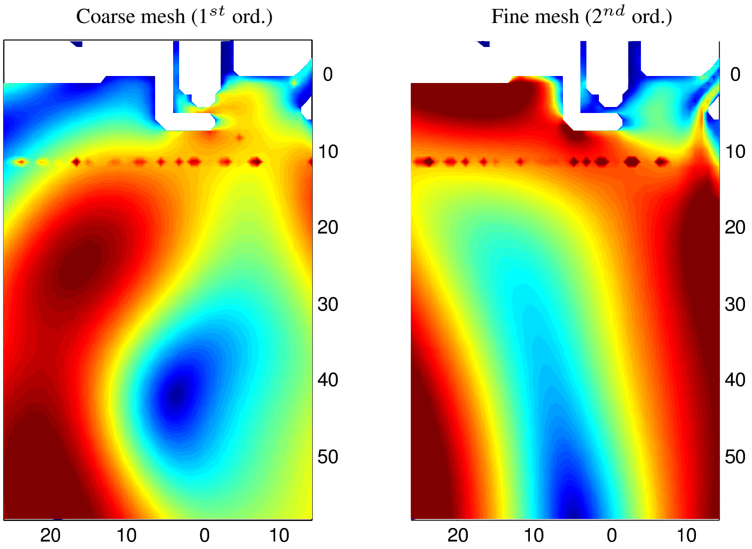

Figure 4.31: *Comparison between computed velocity contours using coarse mesh with 1^{st} order schemes (left) and fine mesh with 2^{nd} order schemes during the second part of the intake stroke (510-540 CAD)*

Compared to the fine mesh, the coarse mesh has lower levels of turbulence and higher numerical diffusivity. This last aspect is in principle responsible for a reduced jet penetration as it is clear from Figs. 4.30(a)-(b). At 510 CAD, there is a high difference in terms of velocity distribution on the piston. In particular, the flow in the fine mesh has a higher penetration and moves fast towards the cylinder head, producing a larger vortex. In the coarse mesh, instead, a vortex is created in the bottom part of the cylinder and its shape at BDC is very similar to the experimental one. However, its generation and evolution is mainly affected by numerical diffusivity and reduced jet penetration that increases the vortex strength. In particular, the first one diffuses the velocity from the piston and the liner to the cylinder bulk. For what concerns the second order grid, again the main reason for a non correct estimation of the velocity field seems to be only due to the wrong distribution of the in-cylinder turbulence intensity and related diffusivity because of the coarse resolution adopted below the inlet valve. For sake of completeness and to further clarify what was found so far, Fig. 4.32(a)-(d) finally compares experimental and computed turbulence intensity distributions for the three different simulation setup used.

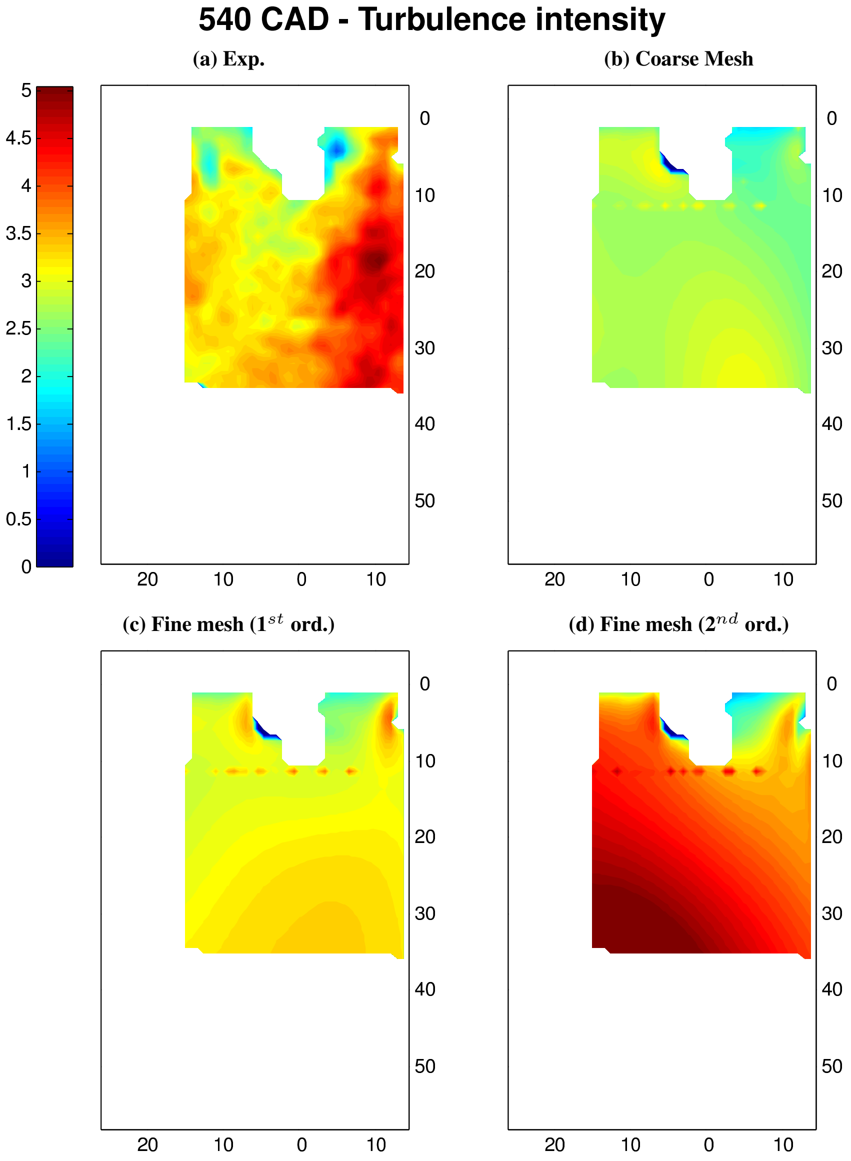

Figure 4.32: *Comparison between computed and experimental turbulence intensity distribution at 540 CAD. Units are in [m^2/s^2], scale is 0 (blue) - 5 m^2/s^2 (red)*

Fig. 4.32(d) shows that only the fine mesh with second order schemes is able to properly reproduce the same levels of turbulence which were experimentally found, even if with a wrong distribution due to the non correct position of the predicted vortex at BDC. First order methods instead underestimate the turbulence intensity and this further explain how numerical diffusivity can lead to acceptable results but with the wrong physics.

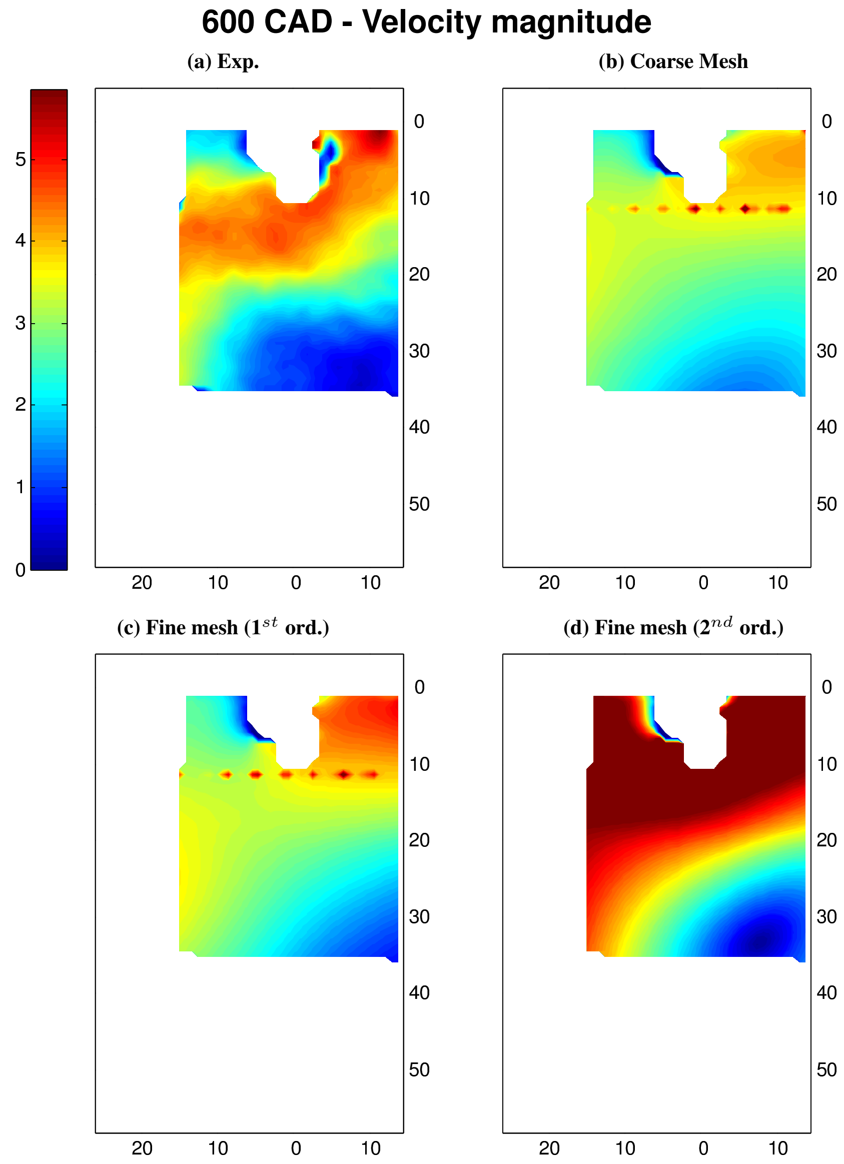

Figure 4.33: *Comparison between computed and experimental velocity magnitude distribution at 600 CAD. Units are in [m/s], scale is 0 (blue) - 5 m/s (red)*

From BDC to IVC time the main vortex inside the cylinder evolves and, in Fig. 4.33 the computed flow field immediately after the valve closure time is illustrated. The vortex is still intense and fine mesh with 2nd order schemes produces the best agreement with experimental data. This is mainly due to the better capability of such grid to reproduce flow and turbulence details in combination, predicted velocity magnitudes are higher than experimental ones. The coarse grid with first order schemes, producing the best flow agreement at BDC, predicts a new weaker vortex due to numerical diffusivity that also affects the results of the fine mesh in Fig. 4.33(c). For a proper prediction of both fuel-air mixing and combustion processes, a good estimation of both flow field and turbulence at IVC time is fundamental. Within this context, it is quite clear from computed results that the fine mesh with second order schemes produces the best agreement with experimental data. For this reason, from now, only results obtained with such mesh will be analyzed and compared to experimental measurements.

Fig. 4.34 provides a comparison between experimental and computed velocity fields with the best setup (fine mesh and second order schemes). A rather good agreement was achieved at this point: the location of the vortex is correctly placed in the bottom-right part of the window. Furthermore, the simulation correctly predicts an almost horizontal gas flow in the region immediately below the cylinder head. Finally, also the vortex intensity is properly described when looking at the size of the velocity vectors. However, Fig. 4.35 illustrates that turbulence levels remain rather high compared to the experimental data. Still turbulence distribution is affected by what happened during the intake stroke. Now that compression stroke starts, turbulence levels are expected to increase due to the breakdown of the vortex. Hence, it is expected that predicted turbulence levels inside the cylinder will remain higher than the computed ones.

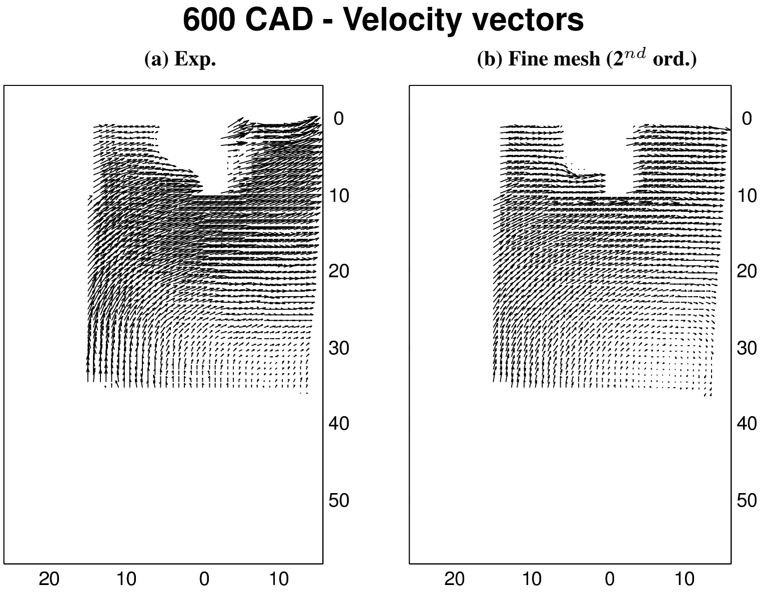

Figure 4.34: *Comparison between computed and experimental velocity vectors at 600 CAD: (a) Experimental data, (b) Fine mesh with second order schemes*

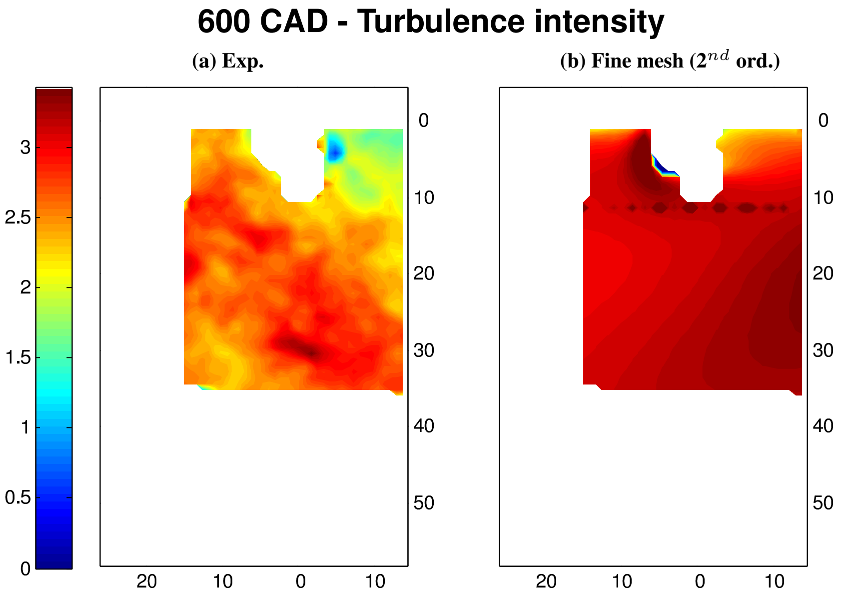

Figure 4.35: *Comparison between computed and experimental turbulence intensity distribution at 600 CAD: (a) Experimental data, (b) Fine mesh with second order schemes. Units are in [m^2/s^2], scale is 0 (blue) - 3 m^2/s^2 (red)*

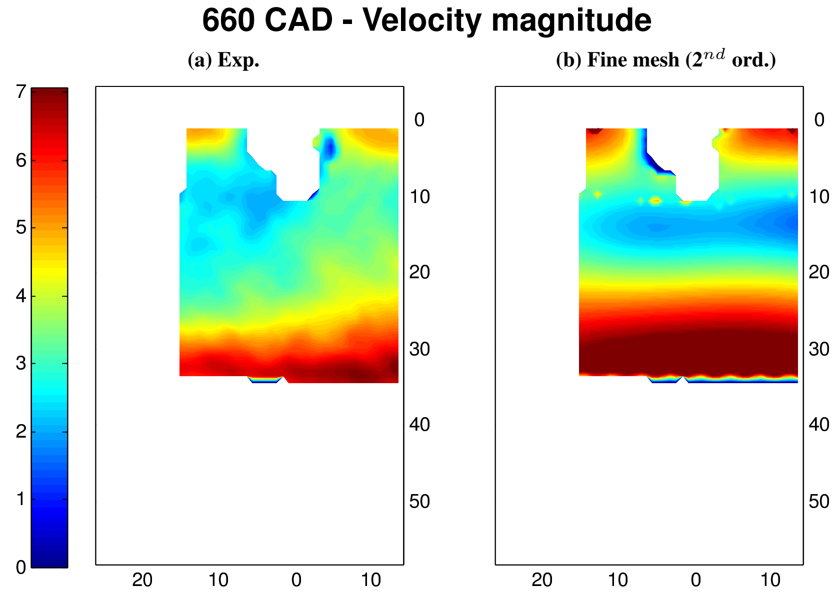

Figure 4.36: *Comparison between computed and experimental velocity magnitude distribution at 660 CAD. Units are in [m/s], scale is 0 (blue) - 7 m/s (red)*

Halfway during compression, at 660 CAD, the flow is still characterized by a strong vortex as it can be seen in Fig. 4.36. However, simulations present a stronger vortex compared to experimental data.

This is much clear from Fig. 4.37, where computed data show a stronger horizontal component of the velocity vectors compared to the measured ones.

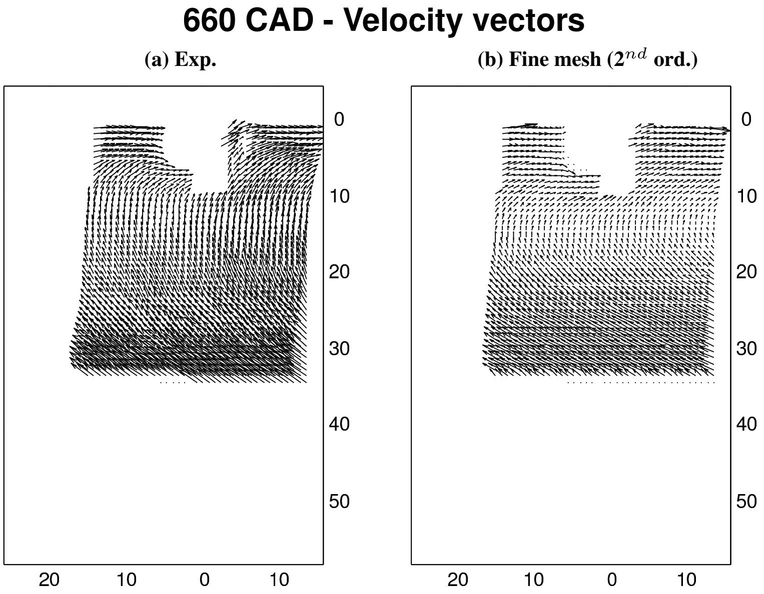

Figure 4.37: *Comparison between computed and experimental velocity vectors at 660 CAD: (a) Experimental data, (b) Fine mesh with second order schemes*

Fig. 4.38 shows that both experiments and simulations predict an increase of turbulence intensity due to dissipation of the vortex kinetic energy into turbulence.

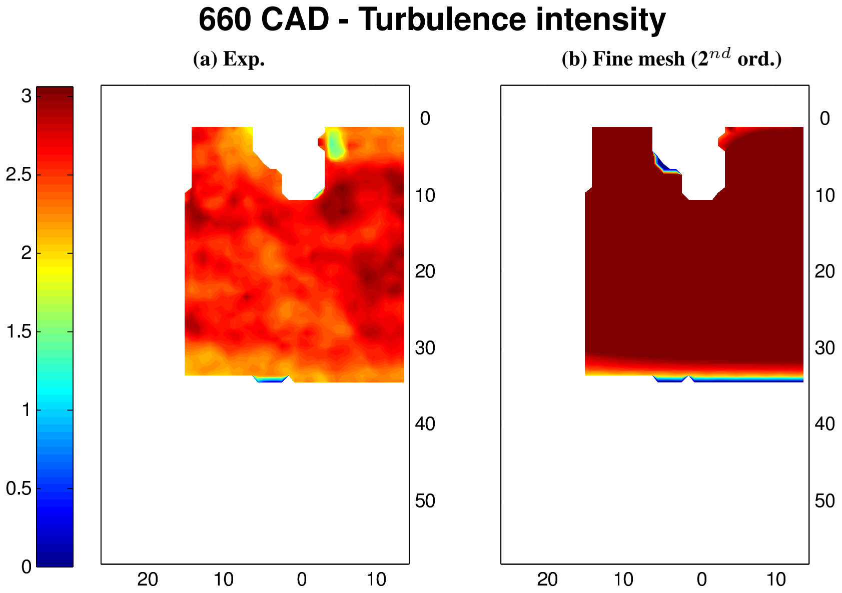

Figure 4.38: *Comparison between computed and experimental turbulence intensity distribution at 660 CAD: (a) Experimental data, (b) Fine mesh with second order schemes. Units are in [m^2/s^2], scale is 0 (blue) - 3 m^2/s^2 (red)*

Close to TDC, the agreement between experimental and computed data is still acceptable, mainly close to the spark-plug and above the piston. Fig. 4.39(a) displays that the high velocity region is experimentally found just on left of the spark-plug in experiments while, in Fig. 4.39(b), predicted charge motions involve also the right part. Here, due to very small gas speed, velocity vector comparison for this condition is omitted.

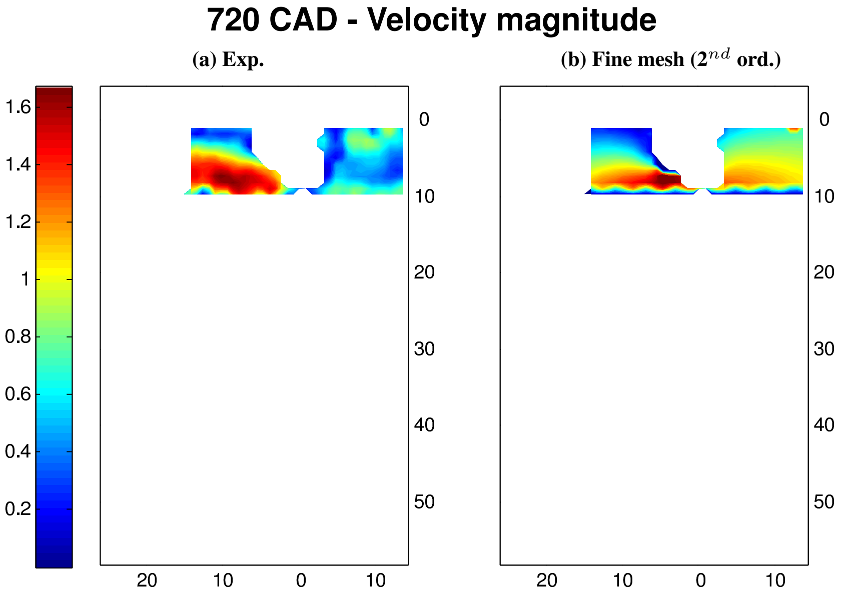

Figure 4.39: *Comparison between computed and experimental velocity magnitude distribution at 720 CAD. Units are in [m/s], scale is 0 (blue) - 3 m/s (red)*

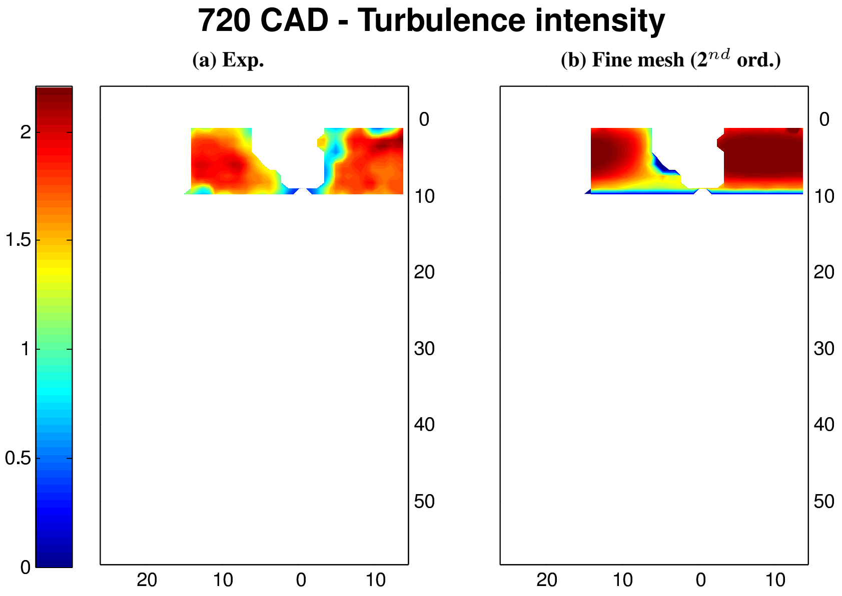

Figure 4.40: *Comparison between computed and experimental turb. intensity distrib. at 700 CAD: (a) Exp. data, (b) Fine mesh with 2^{nd} or. schemes. Units in [m^2/s^2], scale: 0 (blue) - 2 m^2/s^2 (red)*

Fig. 4.40 shows levels of turbulence intensity at TDC. Predicted distribution is similar to experimental data, even if turbulence levels are higher because of the highest intensity of the predicted vortex. However, the agreement is satisfactory for considering the proposed setup (fine mesh and second order schemes) suitable also for running combustion simulations on the same engine.

To summarize the computed results and further understand the predictive capability of the proposed approach, a comparison between computed and experimental kinetic energy and its rms was performed. Such quantities are computed on the two experimental grids were velocity field data were acquired, and they are defined as:

$$K_{mean} = \sum_{i=1}^{n_g} \frac{1}{2} U_i^2 \tag{4.10}$$

$$rms_K = \sum_{i=1}^{n_g} \frac{1}{2} u_i^2 \tag{4.11}$$

where n_g is the number of grid points in the measurement window, U the velocity and u' the turbulence intensity. The same procedure was carried out for computed data, which were interpolated at experimental grid point positions. Two different windows were considered: the high resolution one, 26 mm large, which was extensively used to validate the result and the so-called low resolution grid having approximately twice the size of the first one and was used in this work in Fig. 4.27. Results on the high resolution windows are displayed in Fig. 4.41 (a) - (b).

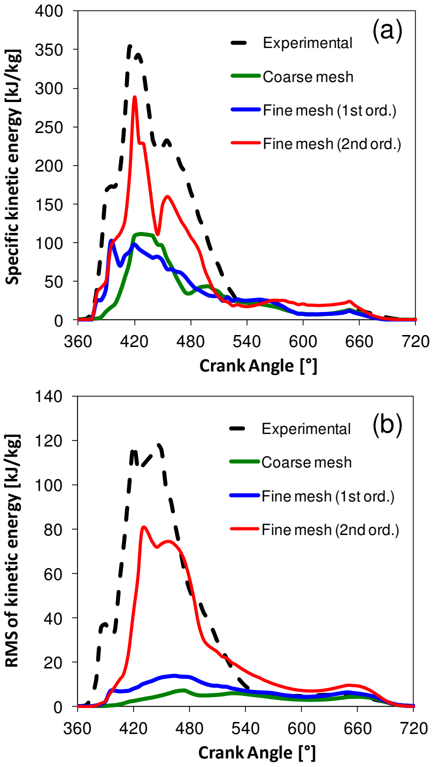

Figure 4.41: *Comparison between computed and experimental evolution of specific kinetic energy (a) and rms of the specific kinetic energy (b) on the high-resolution measurement window*

As expected, results from the fine mesh with second order grid are the ones that better agree with experimental data. The different way the vortex below the valve is predicted is responsible for an underestimation of the kinetic energy during the intake stroke and an overestimation during the compression stroke due to the higher vortex strength during that phase. Under-prediction of the incoming jet penetration is mainly responsible for the bad agreement with experimental data provided by both the coarse mesh and fine mesh with first order schemes. For what concerns the RMS of turbulent kinetic energy, satisfactory results were provided by the fine mesh with second order schemes, even if during the compression stroke the higher vortex strength produces more turbulence than what was experimentally expected.

The comparison shown on the low-resolution window, shown in Figs. 4.42(a) - (b) provides a better idea of the way simulations predict the main details of the flow field. Results are very similar to Fig. 4.41, with the fine mesh with second-order schemes to be the one providing the best agreement with experimental data. Here, the capability to reproduce the turbulence decay during compression is remarkable.

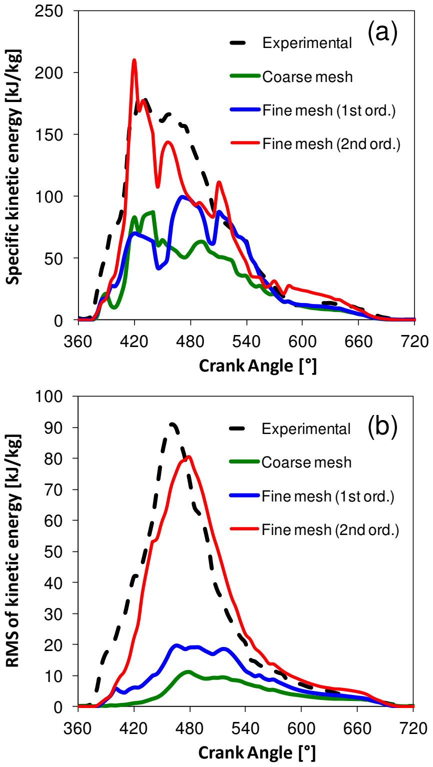

Figure 4.42: *Comparison between computed and experimental evolution of specific kinetic energy (a) and rms of the specific kinetic energy (b) on the low-resolution measurement window*

4.4 Conclusions

This work presented a comprehensive methodology for full-cycle simulations in IC engines. To this end, multiple deforming grids were used and created by a Cartesian, body-fitted mesh generator, *snappyHexMesh*, available in the OpenFOAM code. The portion of cycle covered by each mesh is mainly limited by prescribed quality parameters (skewness, non-orthogonality), its topological or geometrical validity. Grid points are displaced by means of a finite-volume based automatic mesh motion technique. The possibility to employ an automatic mesh generator significantly reduces the required amount of user pre-processing time, since only a cleaned template geometry has to be provided at a prescribed initial position. The grid generator tool supports boundary layer creation and local refinement, allowing a better prediction of incoming cylinder flow and other relevant physical phenomena. Finally, the Cartesian mesh structure strongly reduces the mesh non-orthogonality, making possible to employ high-order schemes.

The proposed approach was validated by performing RANS simulations at non-combusting conditions for an optical engine whose data were available in the ECN database. In particular, effects of mesh structure and numerical schemes were evaluated by testing different configurations. Accurate, full-cycle simulations are possible, however mesh structure and in particular size close to the valves play a big role in computed results, probably even more than the approach used for turbulence. To this end, the possibility to incorporate adaptive local mesh refinement in the proposed methodology appears to be of great importance to improve the quality of results.

CHAPTER 5

Automatic mesh generation applied to an engine sector case

5.1 Introduction

The last section of this work presents an extension of the automatic mesh generation process, discussed in the previous chapter, to sector engine cases. Referring to general literature, CFD simulations of Diesel engines have been traditionally performed using a sector model corresponding to one hole of the fuel injector. Only recently some interest has grown towards the analysis of the entire cylinder domain in order to investigate the spray-to-spray interaction or perform a full cycle simulation. Though, when these aspects are considered of second order interest, sector simulations are the common practice. Furthermore many commercial software are lately adopting unstructured Cartesian grids instead of the classic structured polar meshes. This gives the possibility to define a grid that is independent of spray direction and domain geometry, and for which cell tangential size is not a function of the distance from the cylinder axis.

In this chapter a sensitivity analysis on mesh size is presented. RANS simulations of three different grid structures were carried out with the aim of evaluating and validating the mesh generation process. To give completeness and general applicability to the analysis, a closed cycle including fuel injection and combustion was simulated. Global quantities such as heat release and in cylinder pressure were compared with experimental measurements taken on a CAT 3512 engine as well as a qualitative analysis was carried out in terms of spray related quantities and flame structure evolution in time.

5.2 Peculiarities of sector cases

As already seen in Chap. 4, the methodology previously presented was developed with the aim to simulate full-cycle simulations under "cold flow" conditions. In order to extend the same concepts to sector cases involving fuel injection and combustion, some additions were necessarily needed. In particular, the use of sector meshes implies the adoption of cyclic boundary conditions on the two correspondent sides of the grid. This feature is not immediately applicable to meshes generated with the *snappyHexMesh* utility unless Arbitrary Mesh Interface (AMI) [97] is involved. As explained in Sec. 4.2.3, the output of the mesh generation process is a consequence of the intersection of a block made of hexahedral elements with the surface of the desired geometry provided in stereolithography file format. This intersection results in a body fitted mesh conforming to surface boundaries and properly accounting for the main geometry details including sharp edges. Even if the generation process is well controllable through a multitude of parameters, it is not to the point the user can control or know the actual position of cell vertexes a priori. They are calculated by means of an iterative process which results in a locally random positioning. Hence it is practically impossible to obtain a symmetrical mesh structure, especially for what concerns the side boundaries. Indeed they could be generated, not only with non-matching vertexes, but even with a different number of cell faces.

An attempt to employ AMI was made, motivated by the possibility of using the code as it was, with only minor changes. Nevertheless, the available implementation of this boundary condition in OpenFOAM is thought for simulations across disconnected, but adjacent, mesh domains where the latter can be stationary or move relative to one another. The application to sector meshes resulted in wrong estimations of gradients across the side boundaries and consequent instabilities because of the not perfect matching of the two sides due to the mesh generation process.

To overcome this problem, the best solution was to perform the implementation of a new methodology for symmetrical mesh generation in which both geometrical and topological correspondence between the two sides was achieved.

5.3 Generation of symmetrical meshes

In this section a brief description of the generation process of a single sector mesh is given. A new sub-algorithm was added to the main process in order to guarantee a symmetrical structure of the grids and the flowchart in Fig. 5.1 summarizes the different steps that are necessary for obtaining the desired output.

The algorithm starts with a perfectly symmetrical template (in the *stl* format) that has been previously created at TDC and then moved by the main algorithm to the target crank angle using the *createEngineStl* utility. Here, symmetry on the *stl* file needs to be guaranteed because it will be crucial for the correct generation of the central plane of the mesh.

Then, one of the two side patches of the surface file is extracted, copied and rotated to match the symmetry plane of the sector. This operation individuates a reference plane that will be used during the *snappyHexMesh* phase to create the symmetry plane of the final mesh.

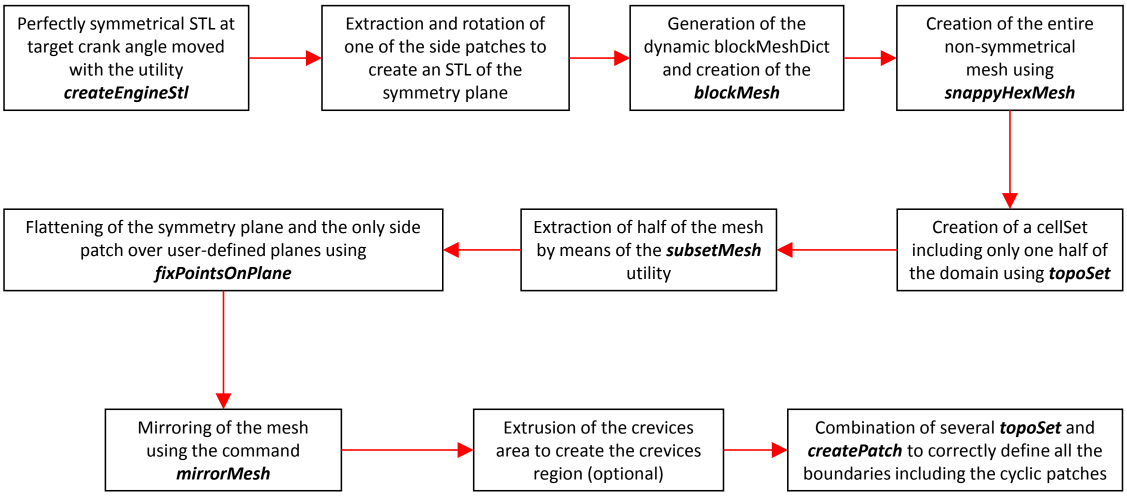

Figure 5.1: *Step-by-step procedure for symmetrical grids generation.*

The next step is the generation of an optimized dictionary (*blockMeshDict*) that contains all the necessary information for the creation of the block to be used for the *snappyHexMesh* phase. Fig. 5.2 shows the structure of a block for a full 3D case. The application on a sector mesh is completely equivalent and three main zones and one interface are identified.

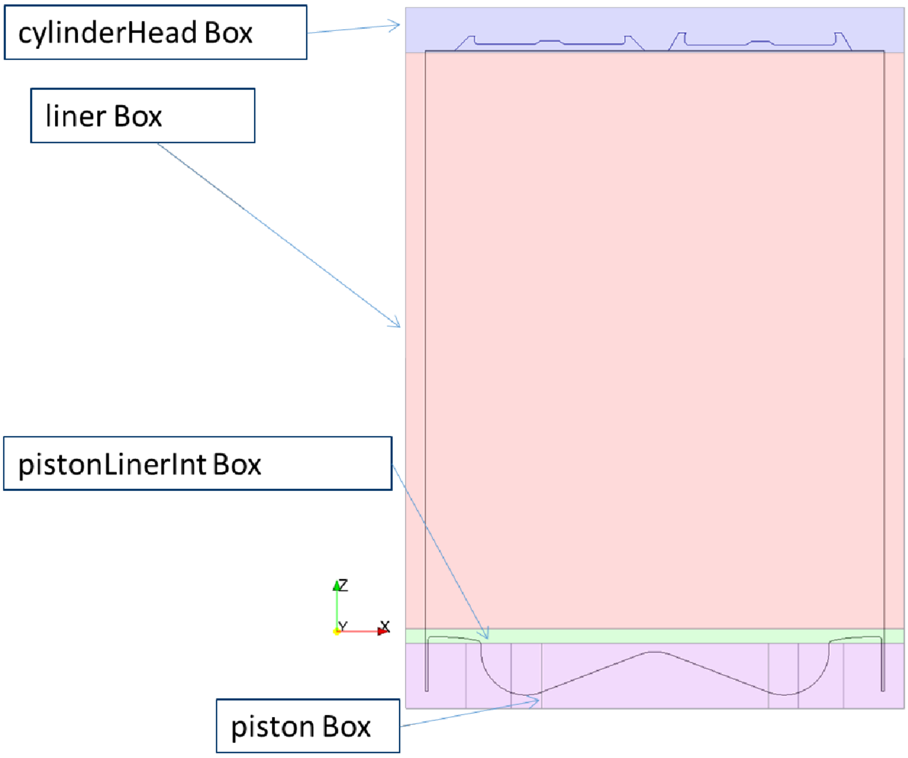

Figure 5.2: *Optimized dynamic blockMesh for a full geometry engine case.*

The *cylinderHead* block is fixed in space and the *piston* one moves rigidly with the piston so that the respective intersections with the cylinder head and the piston are always the same. This allows to keep the same mesh structure in those regions for every grid. The two central blocks are those intersecting the cylinder and the large one is the only one that sees a variable number of elements during the engine cycle. The *pistonLinerInt* block is a one cell layer interface and helps having a predefined mesh size when the piston approaches the TDC and the *liner* block gets removed.

Once the *blockMeshDict* is defined and the starting block is created, an entire non-symmetrical mesh is generated by means of the *snappyHexMesh* utility. Using the *stl* of the symmetry plane previously created, a baffle is introduced on the middle plane of the sector. This allows *snappyHexMesh* to preserve details of the edges in that area so that the next phases can be performed properly.

After the mesh creation, a set of cells belonging to only one half of the domain is identified and subsequently isolated from the other half which gets removed using the *subsetMesh* utility. The result of this operation is one half of the final mesh that before being duplicated needs some additional pre-processing. In particular the side and the symmetry plane need to be flattened on the plane they belong, each one for its own reason. Every face on the side patch needs to have the same normal as the geometric plane they belong, so that the gradients on the cyclic boundaries can be correctly calculated. For what concerns the symmetry plane, it has to be flat and lie perfectly on the xz plane for the mirroring phase to be carried out correctly.

Once the half mesh is ready, the *mirrorMesh* utility generates the second half of the grid that results perfectly symmetrical with respect to the other side. Here, an optional task can be performed if the user needs to generate the crevices volume for the eventual compression ratio compensation. Last operation is the correct identification of all the boundaries including the cyclic patches.

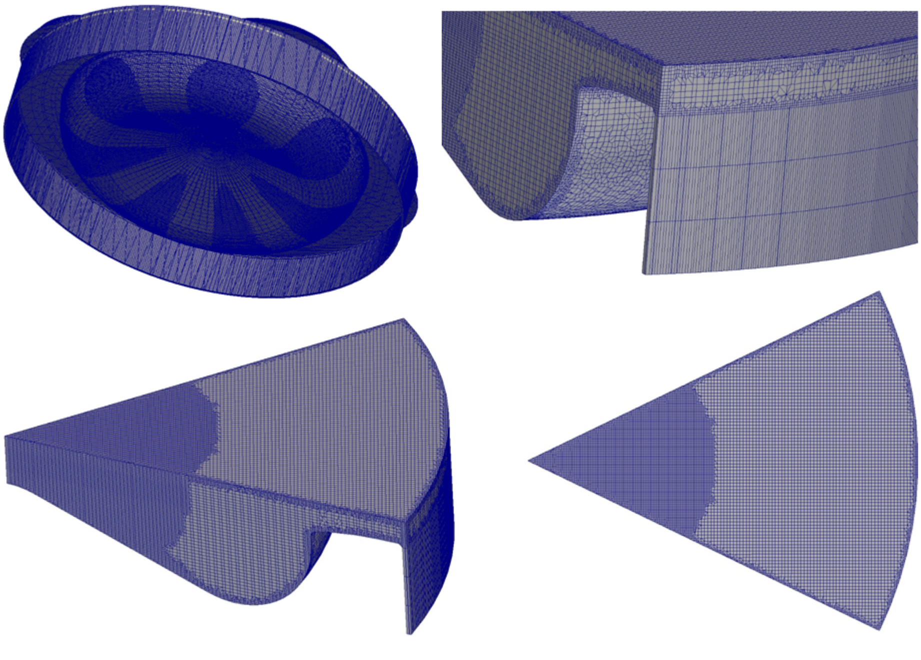

Figure 5.3: *Some of the possible obtainable outputs*

5.4 Application to an industrial case

5.4.1 CAT3512 engine data

A CAT engine was selected to test and validate the mesh generation methodology. Experimental measurements of global quantities were available for the CAT 3512 engine and the following tables summarize the main data relative to geometry, injection system and operative conditions.

Engine Specifications	
Bore [mm]	170
Stroke [mm]	215
Connecting Rod Length [mm]	392.5
Engine Speed [rpm]	1800
IVC [°CA aTDC]	-141.38
EVO [°CA aTDC]	123

Fuel Injection	
Fuel type	$C_{14}H_{30}$
Start Of Injection - SOI [°CA aTDC]	-7
Injection Duration [°CA]	34
Total Injected Mass [mg/cyl/stroke]	67.102
No. Of Nozzle Holes	7
Nozzle Hole Diameter [mm]	0.296
Spray Cone Angle [°]	140

Table 5.1: *Geometrical data and injection characteristics of the CAT 3512 engine*

Domain Initialization	
Pressure [bar]	8.36
Cylinder temperature [K]	469.36
Turbulent Kinetic Energy [m^2/s^2]	62.4
Turbulent Kinetic Energy Dissipation Rate [m^2/s^3]	47650
Chemical composition [% mass]	CO_2 = 2.28 - H_2O = 1.89 N_2 = 75.51 - O_2 = 20.32

Wall cycle-averaged temperatures	
Head [K]	500
Liner [K]	500
Piston [K]	656

Table 5.2: *Initial and boundary conditions at 90° before TDC*

5.4.2 The solver: *CCMDieselEngineDyMFoam*

The solver selected for the validation phase allows the user to perform engine calculations involving moving meshes: add/removal layering and cells deformation (compression and expansion) are supported. Detailed chemical kinetic is included and coupled with multidimensional *Chemistry Coordinate Mapping* (CCM) discretization [98] and *In Situ Adaptive Tabulation* (ISAT) (see [99]). Mixture fraction, temperature and species concentration are used to map the CFD domain and reduce the computational resources dedicated chemistry calculation. Similar cells with close values of the three variables are grouped together according to user-defined spans that discretize the whole range in which the variables are defined. The reaction rate is computed only once for each group of cells and then returned to the CFD domain as a source term for the energy equation.

5.4.3 Mesh generation strategy and case setup

Defining with 360° the TDC corresponding to the fuel injection and combustion, the simulation starting point was fixed at 270°. The reason for this decision relates to the lack of information about the flow field at the Inlet Valve Closing (IVC) and the impossibility to run a full open cycle simulation to create it. The only available information is the estimation of the swirl profile, so having to start from a situation in which the fluid is almost still, the best option is to place the piston in a position in which acceleration is zero, hence the choice to start from 270° was made to reduce possible instabilities at the beginning of the simulation.

For what concerns the initial conditions estimate, a 0-D model was employed to match the experimental pressure during the compression phase. The inputs for the model were the initial chemical species composition, the total average cylinder mass (derived from air total flow rate) and the EGR percentage. An estimate of the polytropic curve exponent was made to match the pressure trace and finally a couple of plausible values for initial pressure and temperature were computed.

Three different mesh series were created in order to run a sensitivity analysis on minimum mesh size of the nozzle region. Typical engines CFD applications are lately adopting minimum sizes around 0.25 mm. Due to the injection nozzle size (diameter of 0.296 mm) a minimum size of 0.35 mm was chosen for the reference case. 0.5 mm and 0.25 mm were chosen respectively to test the possibility of using a coarser mesh and to evaluate the robustness of the Eulerian-Lagrangian approach when void fraction values are very high in the vicinity of the injector nozzle (causing the invalidation of the diluted spray assumption). Fig. 5.4 shows the cell count along the whole simulation for the three different mesh sizes.

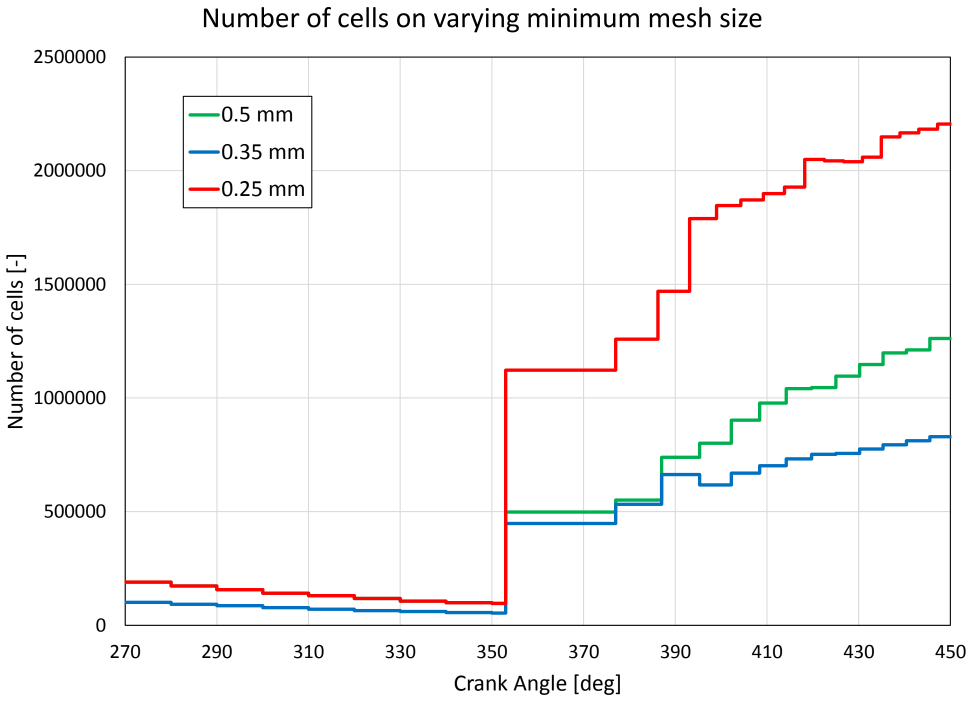

Figure 5.4: *Cell count vs Crank Angle on varying mesh size*

In Fig. 5.4, cell counts for the 0.25 mm and the 0.5 mm coincide up to the start of injection (SOI) at 353°. Also, cell count of the 0.5 mm has a counterintuitive trend, being always greater than the 0.35 mm case. This is related to the choice of the base mesh size, done when the initial block was defined. 0.5 mm and 0.25 mm cases shared the same block with a base size of 4 mm, while the 0.35 case had a 5.6 mm base size. The only difference between the two 4 mm cases was in the near nozzle area where the finest size case, as done in the reference one, had a spherical refinement region that was missing in the 0.5 mm (see Fig. 5.5).

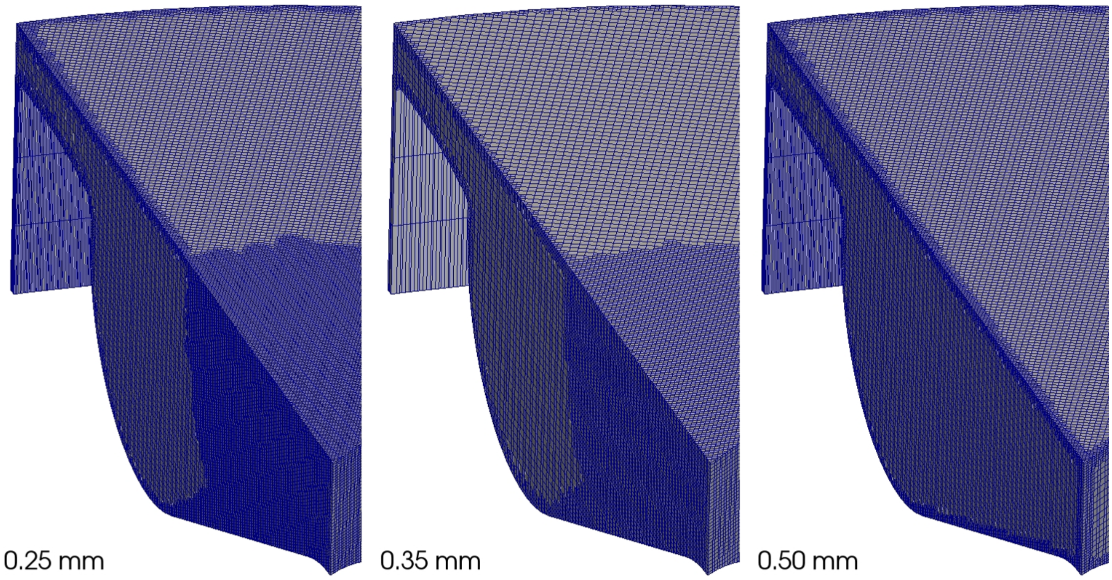

Figure 5.5: *Comparison of the three different mesh structures*

This strategy is motivated by two different reasons. If the same approach used for the 0.25 and the 0.35 mm cases was extended to the 0.5 mm one, a base mesh size of 8 mm would have been necessary, leading to too large cells in the far nozzle region (especially around the squish area) and to a poor description of the flame structure from the final moments of the injection on (when the flame reaches the above-mentioned area). Furthermore, the missing refinement in the nozzle area gave the opportunity to evaluate the behavior of both spray and jet whether a mesh size jump was present or not.

The whole mesh generation process required 3 to 5 hours for creating the grids on a 12 processor machine. Another hour should be added for the pre-processing related to the *stl* creation and to the setting of the *snappyHexMesh* dictionary leading to a total pre-processing user time contained within a working day.

Among all the employed submodels, *k-epsilon* was selected to model turbulence while Blob model and KHRT for injection and spray breakup. All the submodels were tuned according to the values adopted for the study shown in Chap. 3. Same choices of Chap. 3 were made for collision and dispersion model as well, and therefore were not included.

To model fuel, n-tetradecane was chosen for physical properties and n-heptane for chemistry as done by Krishnasamy et al. in [100]. Reduced chemical kinetic mechanism for n-heptane was provided by CAT and was characterized by 42 species and 168 reactions.

5.5 Validation of the methodology

5.5.1 Heat release and in-cylinder pressure

As already pointed out in the introduction to this chapter, the new methodology for automatic cartesian grids generation for sector engine cases was tested and validated by means of a sensitivity analysis. Both minimum mesh size in the near nozzle region and general mesh size all over the whole domain were varied to test goodness and robustness of the approach. Here, instantaneous and integral apparent heat release as well as in cylinder pressure are compared with available experimental data and, together with a qualitative analysis of global spray quantities, some conclusion will be drawn at the end of the chapter.

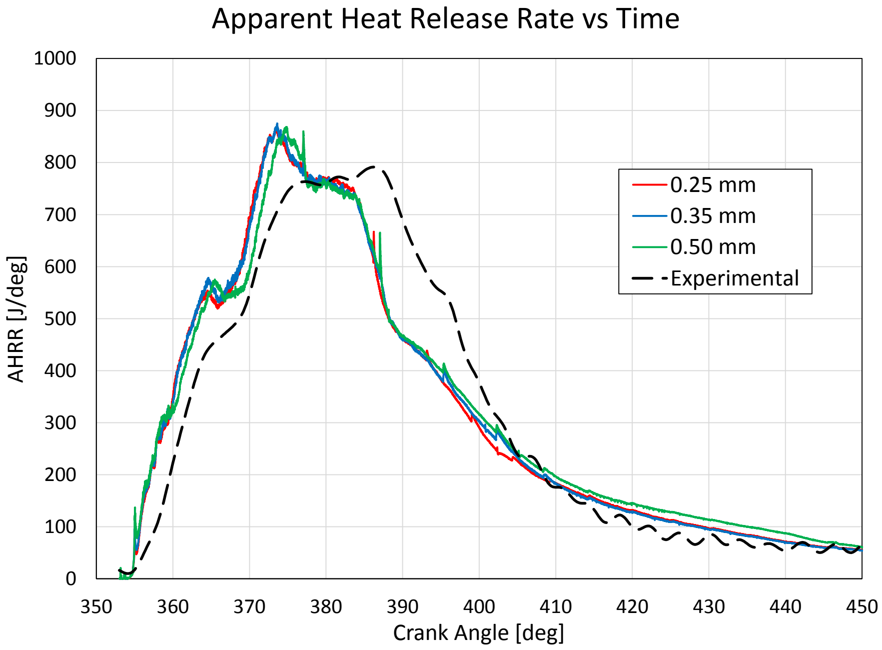

Figure 5.6: *Apparent rate of heat release rate vs time*

Figs. 5.6 and 5.7 show respectively instantaneous and integral apparent heat release. Looking at the latter it can be seen that the final value of total heat release is well computed for all the three cases. This gives confidence that the chemical kinetic mechanism and the chemistry model are able to model correctly the Lower Heating Value (LHV) associated to the fuel. Some differences can be seen in the first 50 degrees after the SOI, and this is confirmed in Fig. 5.6 which shows how apparent heat release rate is overestimated during the injection phase. The explanation behind this behavior is probably connected to different reasons that can be either acting at the same time or not.

The input injection law used for the simulations could be probably anticipated with respect to the real one. There were no available information about hydraulic delay and a shift of 1.5 crank angle degrees toward TDC could lead to a better matching of experimental heat release rate. Also, the lack of information about an experimental analysis of spray morphology lead to the choice of using the same setup adopted in Chap. 3. In the CAT 3512 engine, injector nozzle is three times larger than the Spray A one, so a better tuning of the breakup model constants could possibly help improving spray atomization and delaying ignition of the fuel. There are some doubts concerning also the total injected mass. The used value is the mere division of the total mass per cycle used by the whole engine. No data are available for the single cylinders, so there is no guarantee the employed value is correctly estimated. Finally, the choice of using a surrogate fuel to model Diesel and the use of a reduced mechanism for n-heptane could play a role in the prediction of ignition delay. However, for the purposes of this work and because of the very high computational resources involved, this approximation was considered of second order interest.

Aside from the discrepancies with experimental measurements, it is possible to state that mesh size did not influence heavily the results. Minimum mesh size around the nozzle affected vapor diffusion in the 0.5 mm case during early stages of injection (see Figs. 5.12 and 5.13). It is believed that the lower jet penetration caused a slower heat release in the 365-380 CA-deg interval and lead also to some small differences in the in-cylinder pressure plot.

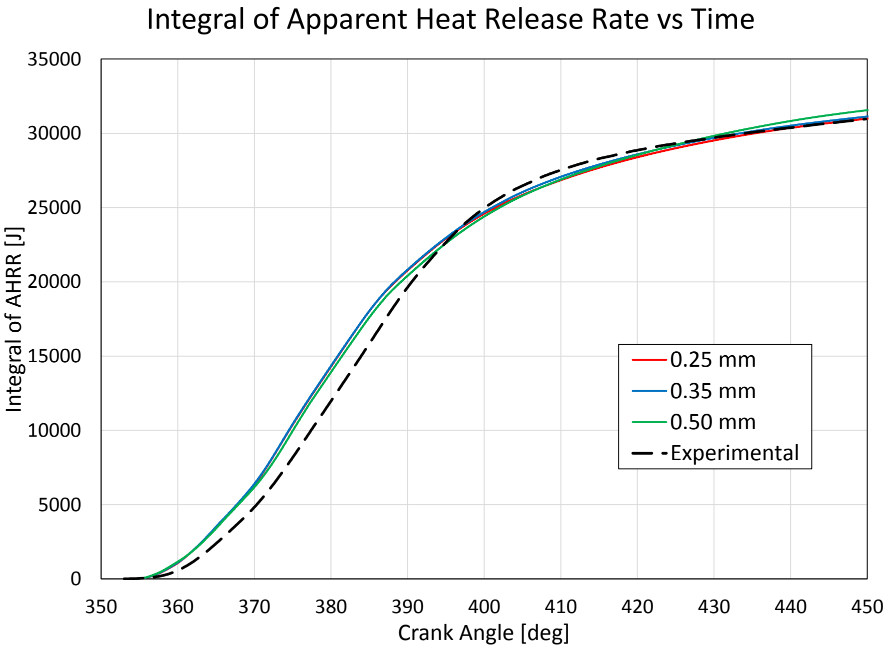

Figure 5.7: *Integral of the apparent heat release rate vs time*

The unphysical peaks visible on the heat release rate plot (at 377, 387, 395 CA-deg and so on) were due to the mapping process from one mesh to the next one. When detailed mechanisms are involved, a lot of intermediate chemical species are created during the calculations. A mapping process involving up to 30-40 species inevitably introduces an error in the local conservation of the species themselves. Among the available methods the *mapNearest* was chosen. It gave the chance to map each specie by copying the exact value stored in the cell having the closest cell center compared to the one in the new mesh. The smaller is the cell deformation during compression and expansion, the more accurate will be the meshing process. Indeed it was found that reducing the validity range of a mesh helped smoothing down the peaks in correspondence of the mapping operations.

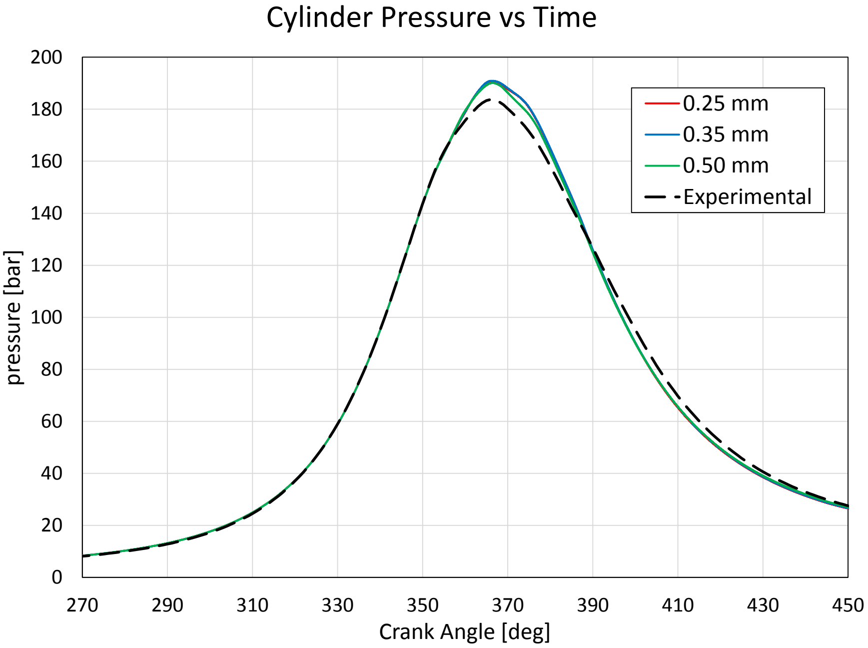

Figure 5.8: *In-cylinder pressure*

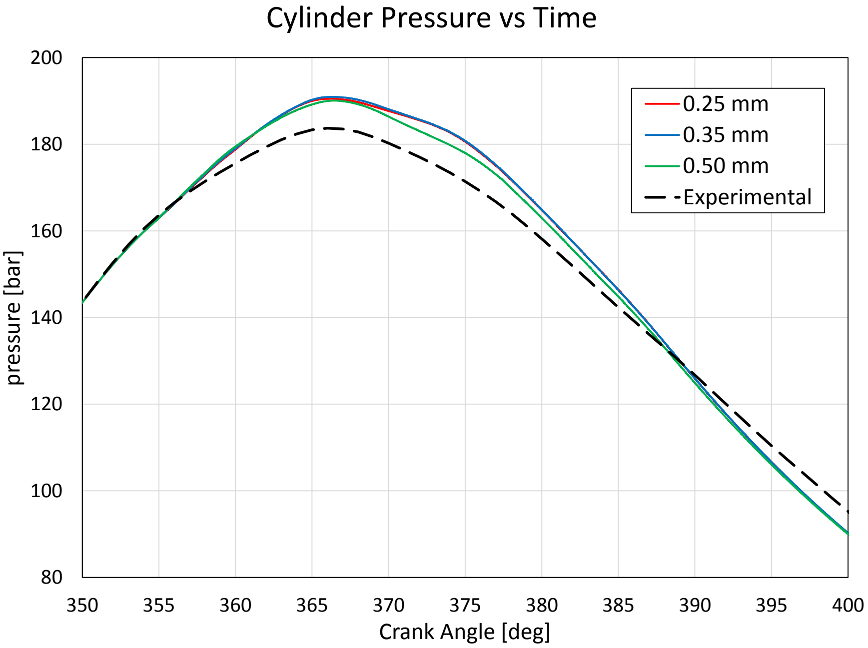

Figure 5.9: *Detail of the in-cylinder pressure around TDC and first part of expansion*

Figs. 5.8 and 5.9 show in-cylinder pressure during the whole simulated time range. Pressure is generally overestimated and consistent with heat release rate. The pressure peak position is well predicted, confirming that total injected mass could be the possible reason for the overestimation of pressure and heat release. No difference was found between the 0.35 mm and the 0.25 mm cases, showing the possibility of good grid convergence on varying minimum mesh size.

5.5.2 Analysis of the spray

Figs. 5.10 to 5.15 show a qualitative analysis on spray global parameters. The unavailability of experimental data makes this analysis weak on the quantitative side, so this part of the validation will focus only on the assessment of mesh size influence on spray behavior.

Fig. 5.10 displays temporal evolution of liquid length, whose definition is the same adopted in Chap. 3 (i.e., based on 99% of liquid mass in system). Steady state value of liquid penetration was practically the same for all cases, quantified in 28-30 mm from the injector nozzle. Small differences were found in the settling in period that becomes larger on increasing mesh size. Nevertheless, differences were contained within one crank angle degree and seemed to converge to the value calculated for the 0.25 mm case. Also 0.35 mm and 0.25 mm cases are more similar to each other than how they are compared to the 0.5 mm one, possibly confirming the convergence trend.

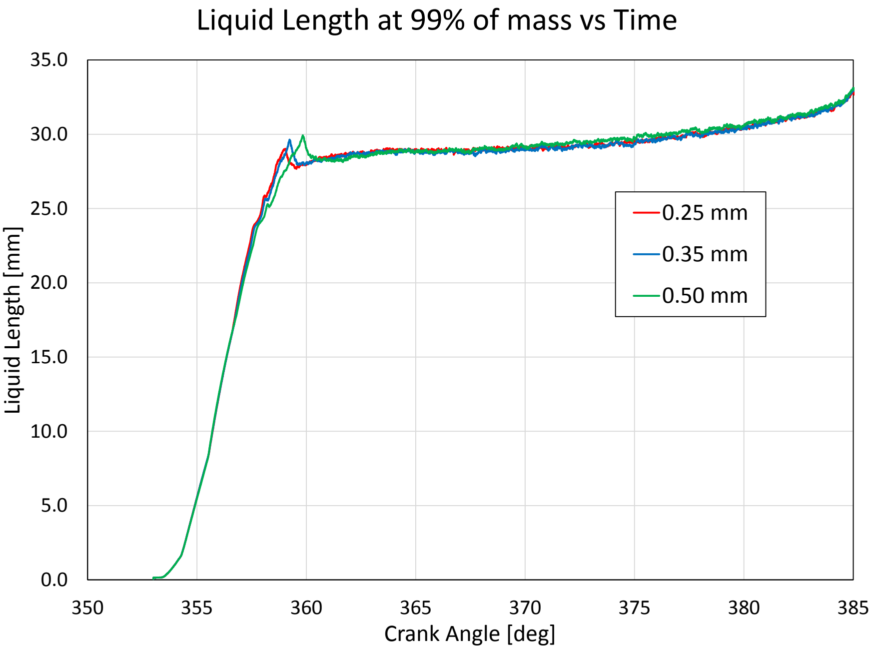

Figure 5.10: *Calculated liquid length vs time*

The same behavior was found for vapor penetration through the chamber. Results tended to converge to those of the 0.25 mm case. Differently than liquid length, jet penetration showed higher differences due to the choice of mesh size: the 0.5 mm case tended to predict a lower penetration during the early stages of the injection phase and until it reached the piston bowl (367 CA-deg). The reason behind this behavior could be related to a different way the momentum exchange between liquid and gas phases happened on varying mesh size. Indeed, when a finer mesh is used, momentum is given

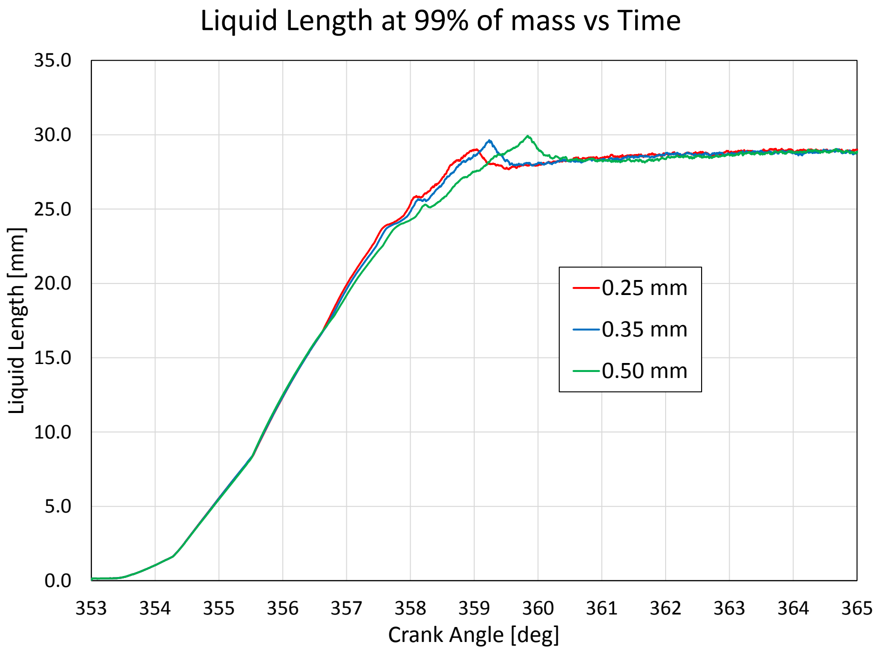

Figure 5.11: *Detail of calculated liquid length around TDC*

to a smaller volume and hence mass of gas. Therefore this led to a higher increase in gas velocity and to a deeper and faster penetration of the fuel vapor jet. The fact that some convergence is shown does not mean that the obtained results are accurate. Only a quantitative comparison with experimental data could help drawing some conclusions on the goodness of the shown grid convergence.

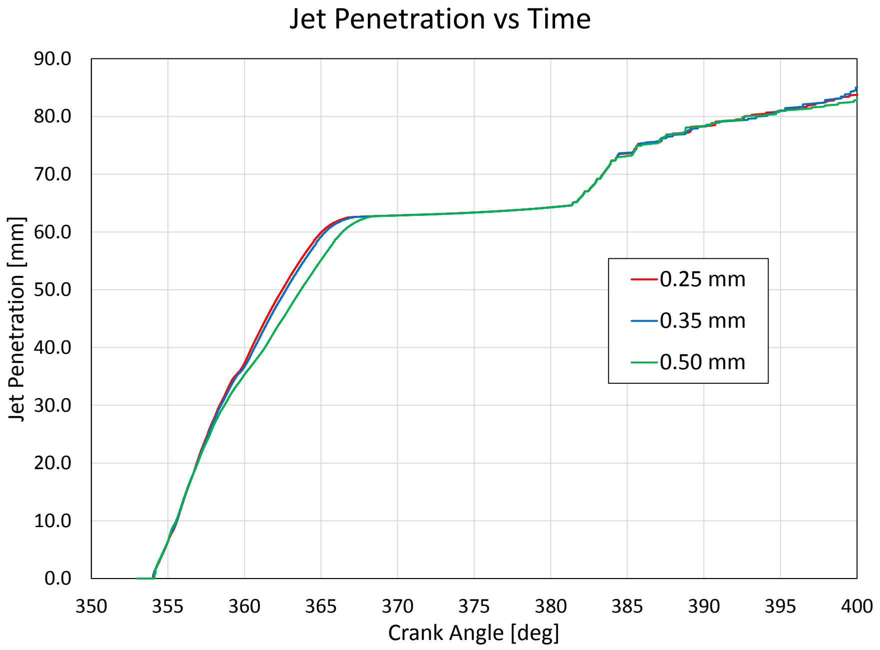

Figure 5.12: *Calculated vapor penetration vs time*

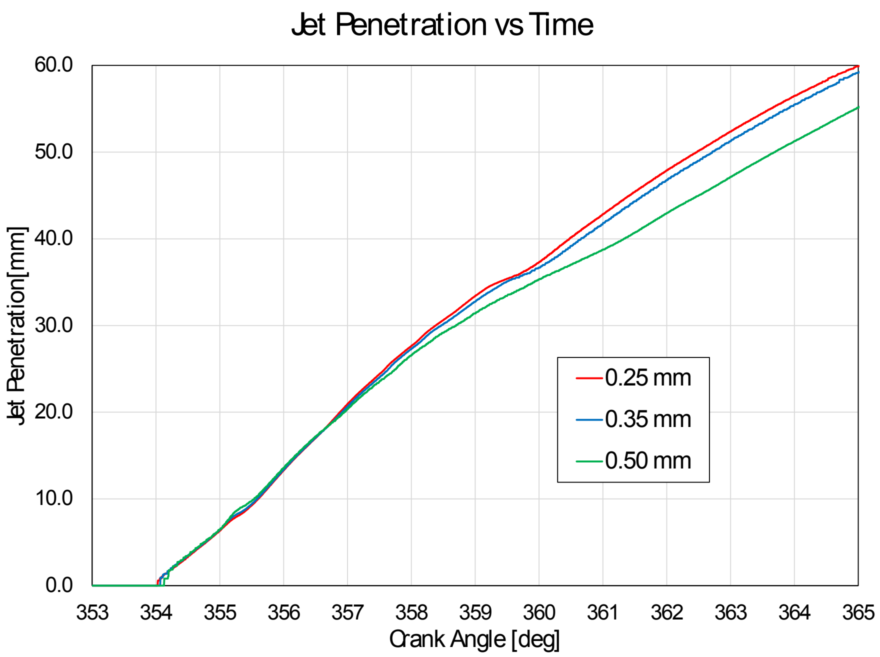

Figure 5.13: *Detail of calculated vapor penetration around TDC*

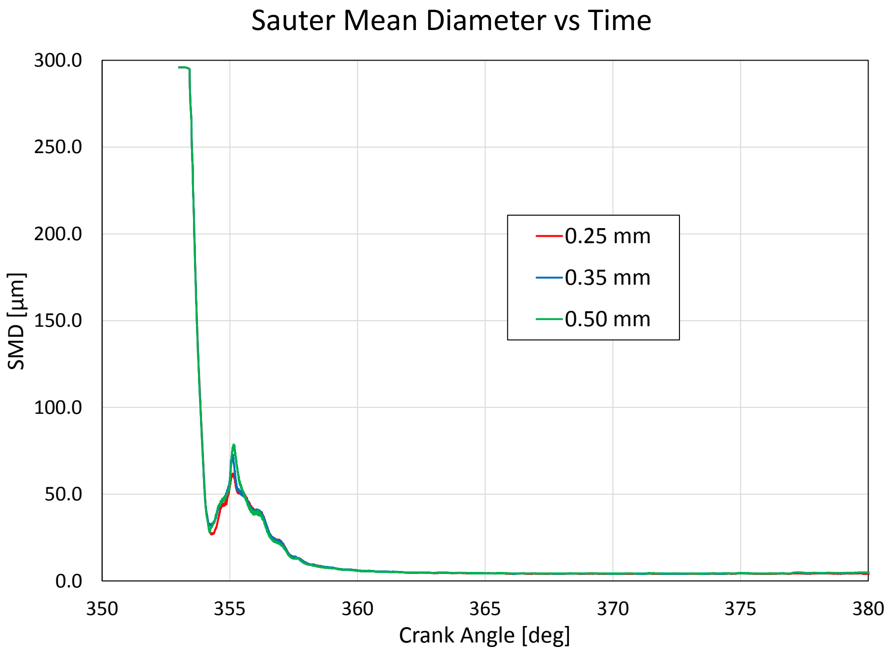

Figure 5.14: *Calculated Sauter Mean Diameter vs time*

The last spray global quantity to be analyzed is Sauter Mean Diameter. As already pointed out, the calculated value is only an indication of the measure of the SMD, but without experimental measurement nothing could be said in quantitative terms. Nevertheless, the qualitative assessment of this parameter confirms what already stressed previously in this section: a good agreement between the three cases was reached, showing some differences in the early stages of the injection phase where the spray of the 0.25 mm case tended to atomize more and faster than the other two cases. Starting from 355.2 CA-deg, 0.25 mm and 0.35 mm cases gave the same results, while the 0.5 mm needed more time to adjust to the other two. The steady state value of the SMD is probably more driven by the evaporation of smaller droplets due to the happening combustion than to spray breakup. A better way to asses possible differences between the three grids could be to run the same simulations in non-reacting conditions.

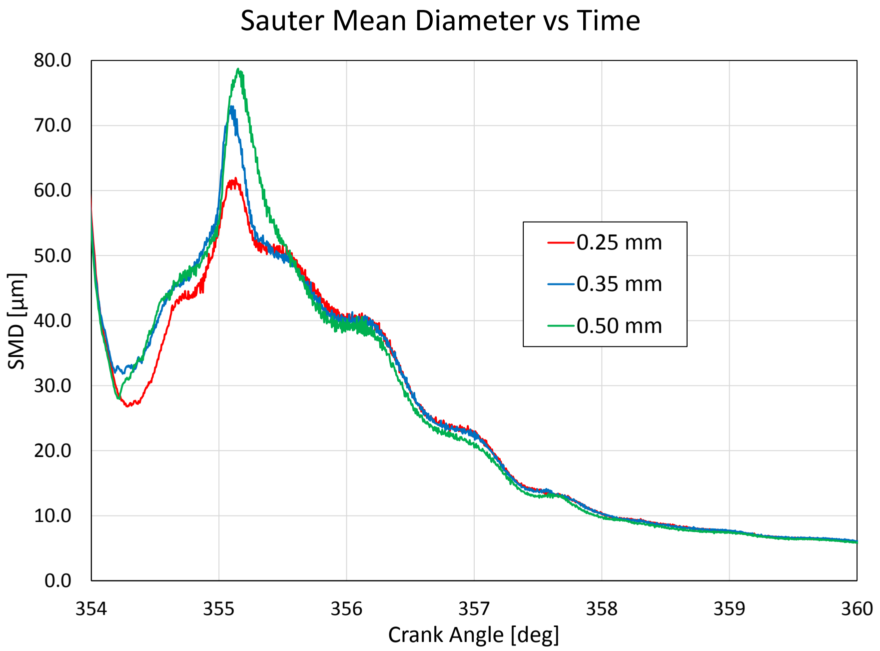

Figure 5.15: *Detail of calculated Sauter Mean Diameter around TDC*

5.5.3 Flame structure analysis

This section presents an analysis of flame structure carried out in both CFD and mixture fraction domains. The Z-T graphics have been plotted for the first stages of combustion and then every 5 CA-deg up to 375°. Ignition of fuel happens around 354.75° and it is faster for the 0.25 mm and the 0.35 mm cases than for the 0.5 mm one. Peak values and position are consistent among the three cases and located around the stoichiometric value of mixture fraction (0.05). One difference that can be seen along the CA-deg span is related to the tail values on the Z coordinate. The finer is the mesh, the higher is the maximum Z: this is intrinsic to minimum mesh size; indeed using a finer mesh it is possible to describe better peak values of any quantity, while on growing size these peaks are smoothed down.

Looking at the Z-T plots evolution in time, it could be noticed how the thickness grows with crank position. Because of the nature of these plots, no information in the physical space could be extracted, but some conclusions could still be drawn. Because of volume variation due to piston movement, thermodynamic condition of the fresh mixture varied with time as a consequence of compression and expansion. Different points with similar mixture fraction and reacting in successive moments, lead to different final temperatures. In particular, especially during expansion, fresh mixture temperature decreased causing lower flame temperatures, hence the thickening of the plots towards lower values of T.

Last analysis of this section concentrated on the contours of temperature and in general on flame structure in the physical domain. First detail that is immediately noticeable is that flame growth was faster when finer mesh were used. Indeed, following the flame attachment point on the piston bowl it easy to notice that the 0.5 mm case had a slower development of the flame in accordance to the slower and lower penetration of the vapor discussed in Sec.5.5.2 (see Figs. 5.12 and 5.13). In general the three flames were very similar to each other and the most appreciable difference was in the contour of equivalence ratio. Especially at 375 CA-deg, the 0.5 mm case showed a wider contour, possibly related to a different estimation of the flow field.

One detail that could be seen in all meshes and especially in the 0.35 mm case is the size of the elements in the squish area. Probably a further refinement in that area would have given the opportunity to describe better the flame structure in a region whose interaction with walls is very important. At the same time this would have increased heavily the number of cells, consequently affecting computational time demands.

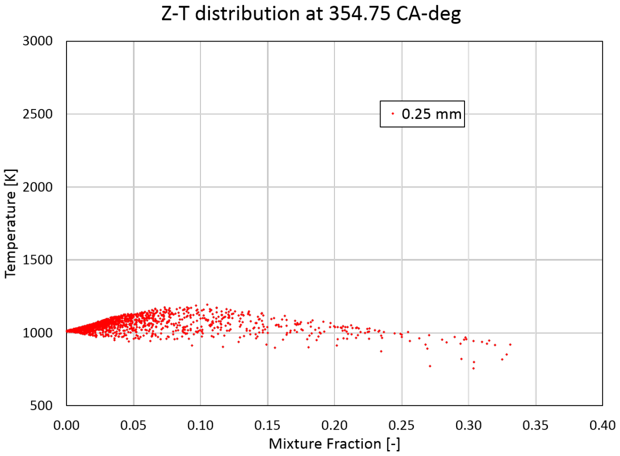

Figure 5.16: *Z-T distribution at 354.75 CA-deg. Minimum mesh size 0.25 mm*

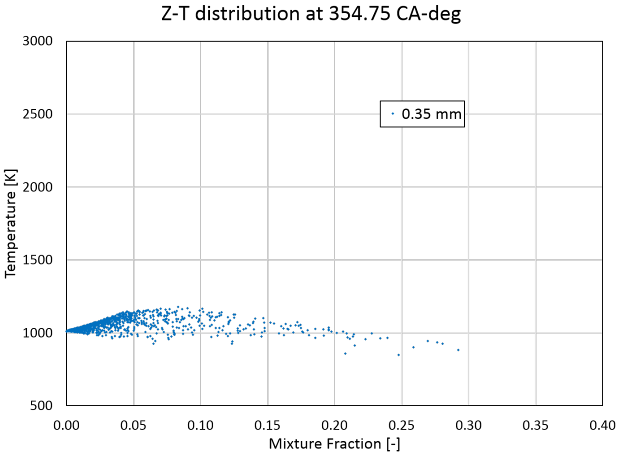

Figure 5.17: *Z-T distribution at 354.75 CA-deg. Minimum mesh size 0.35 mm*

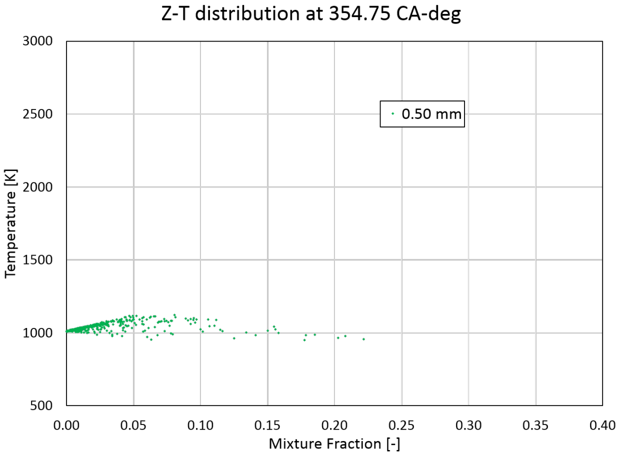

Figure 5.18: *Z-T distribution at 354.75 CA-deg. Minimum mesh size 0.50 mm*

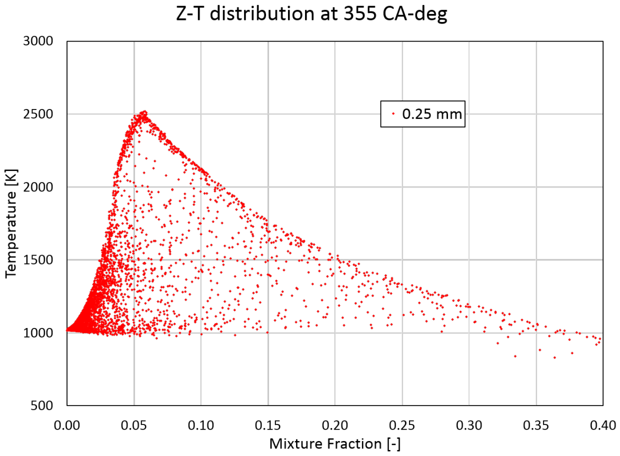

Figure 5.19: *Z-T distribution at 355 CA-deg. Minimum mesh size 0.25 mm*

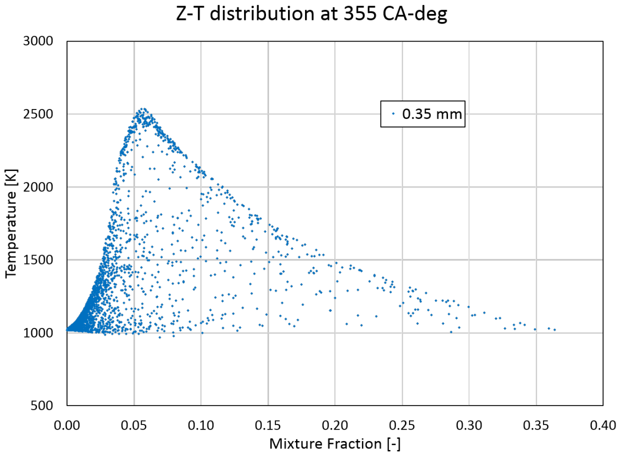

Figure 5.20: *Z-T distribution at 355 CA-deg. Minimum mesh size 0.35 mm*

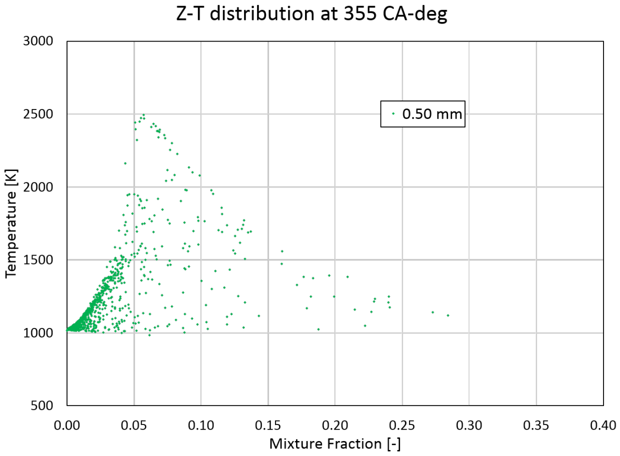

Figure 5.21: *Z-T distribution at 355 CA-deg. Minimum mesh size 0.50 mm*

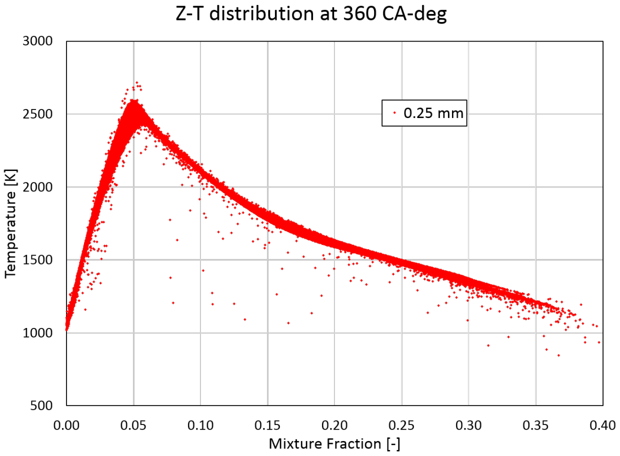

Figure 5.22: *Z-T distribution at 360 CA-deg. Minimum mesh size 0.25 mm*

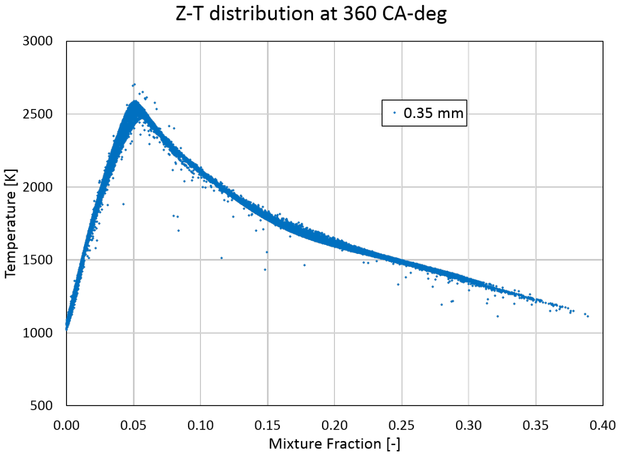

Figure 5.23: *Z-T distribution at 360 CA-deg. Minimum mesh size 0.35 mm*

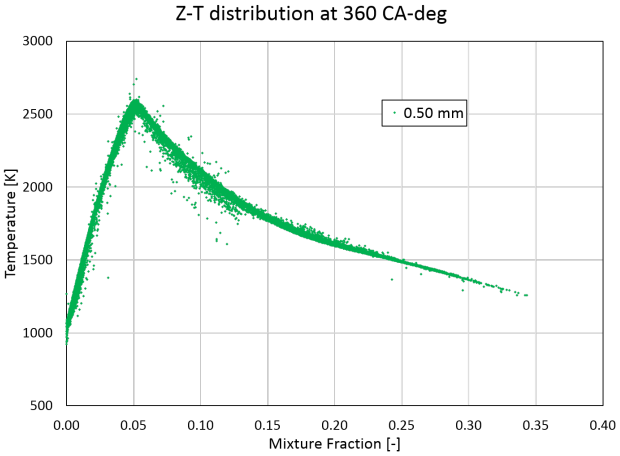

Figure 5.24: *Z-T distribution at 360 CA-deg. Minimum mesh size 0.50 mm*

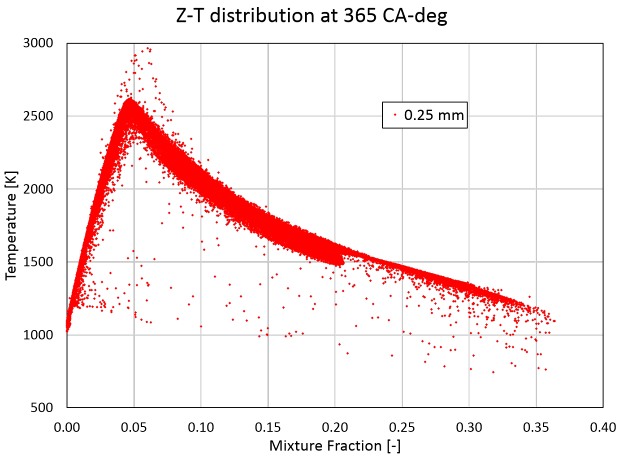

Figure 5.25: *Z-T distribution at 365 CA-deg. Minimum mesh size 0.25 mm*

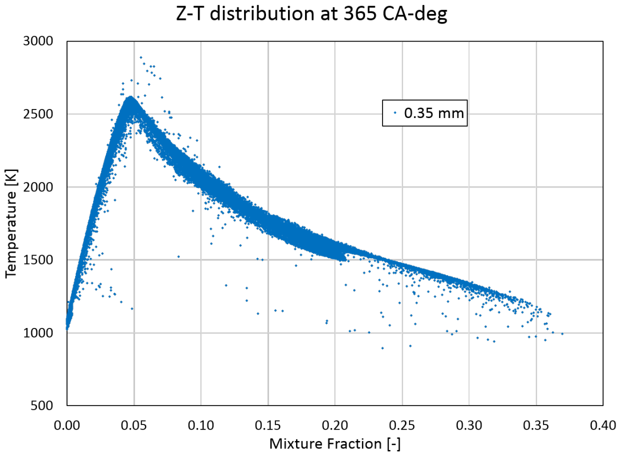

Figure 5.26: *Z-T distribution at 365 CA-deg. Minimum mesh size 0.35 mm*

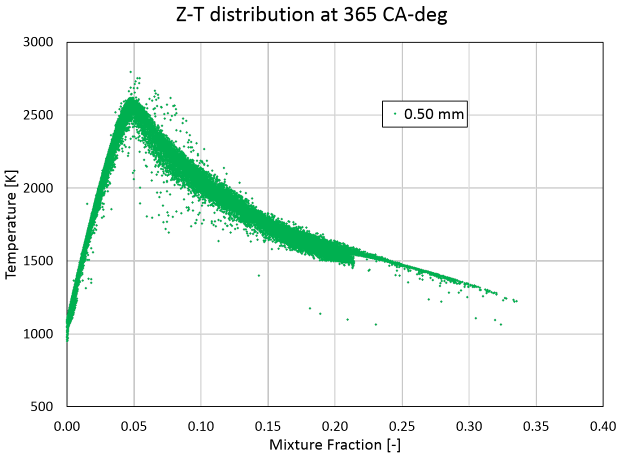

Figure 5.27: *Z-T distribution at 365 CA-deg. Minimum mesh size 0.50 mm*

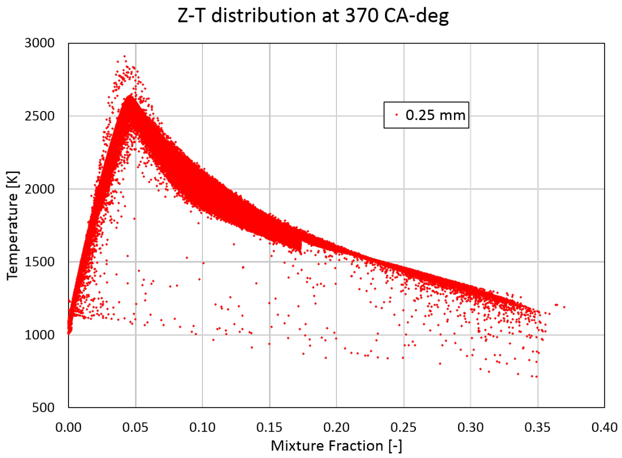

Figure 5.28: *Z-T distribution at 370 CA-deg. Minimum mesh size 0.25 mm*

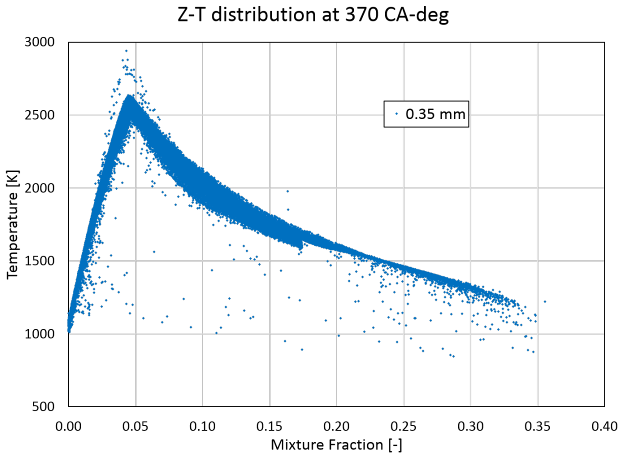

Figure 5.29: *Z-T distribution at 370 CA-deg. Minimum mesh size 0.35 mm*

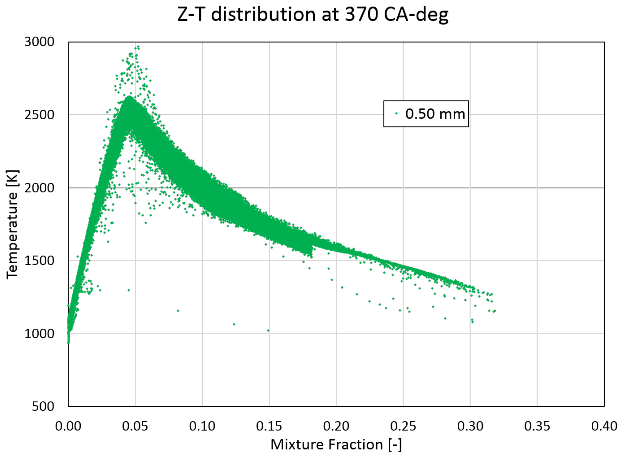

Figure 5.30: *Z-T distribution at 370 CA-deg. Minimum mesh size 0.50 mm*

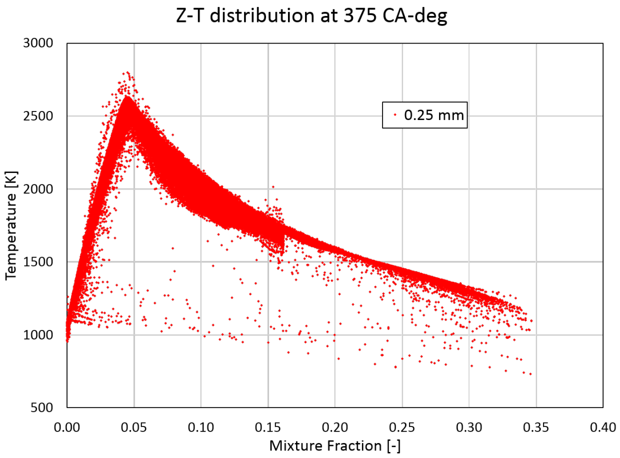

Figure 5.31: *Z-T distribution at 375 CA-deg. Minimum mesh size 0.25 mm*

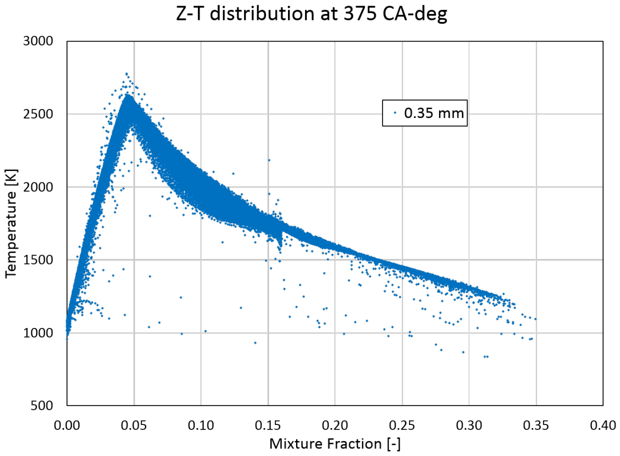

Figure 5.32: *Z-T distribution at 375 CA-deg. Minimum mesh size 0.35 mm*

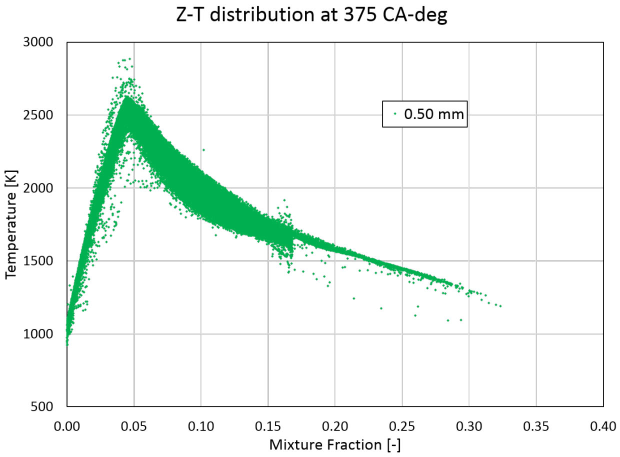

Figure 5.33: *Z-T distribution at 375 CA-deg. Minimum mesh size 0.50 mm*

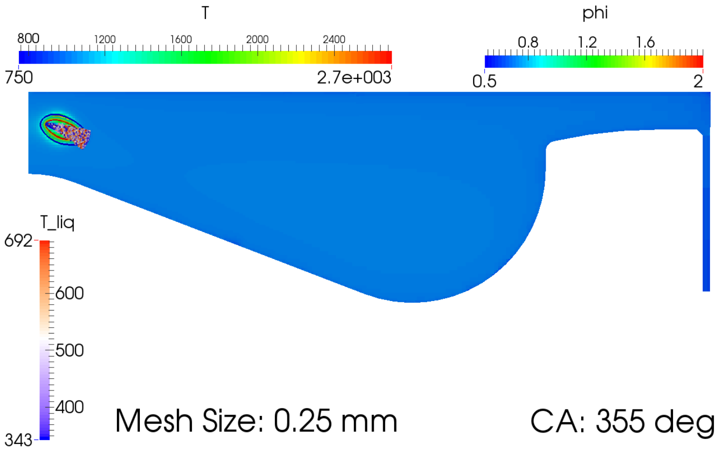

Figure 5.34: *Flame structure at 355 CA-deg. Minimum mesh size 0.25 mm*

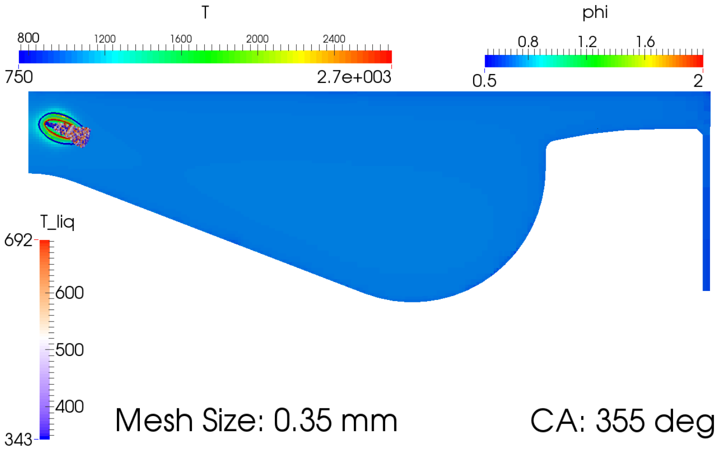

Figure 5.35: *Flame structure at 355 CA-deg. Minimum mesh size 0.35 mm*

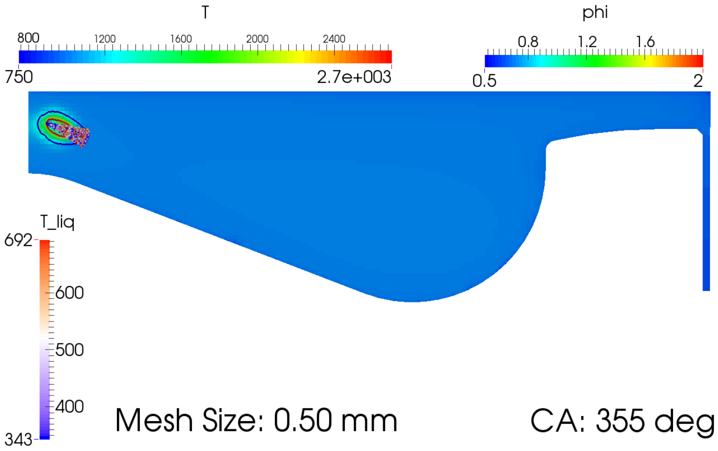

Figure 5.36: *Flame structure at 355 CA-deg. Minimum mesh size 0.50 mm*

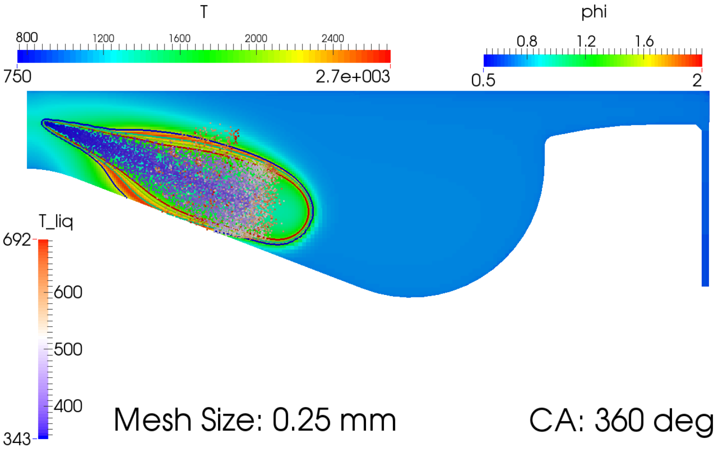

Figure 5.37: *Flame structure at 360 CA-deg. Minimum mesh size 0.25 mm*

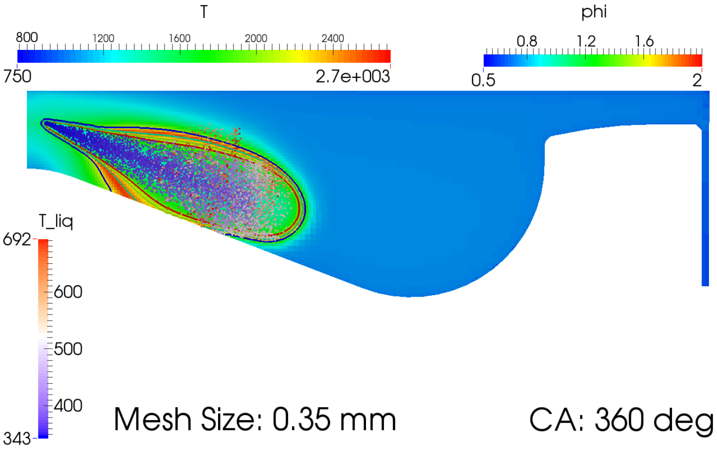

Figure 5.38: *Flame structure at 360 CA-deg. Minimum mesh size 0.35 mm*

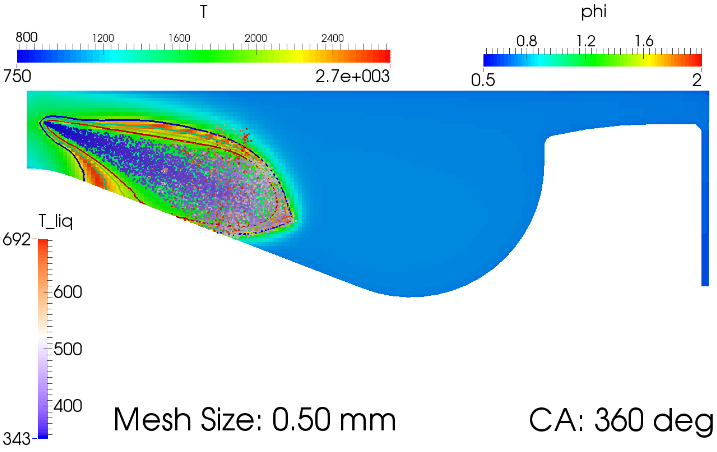

Figure 5.39: *Flame structure at 360 CA-deg. Minimum mesh size 0.50 mm*

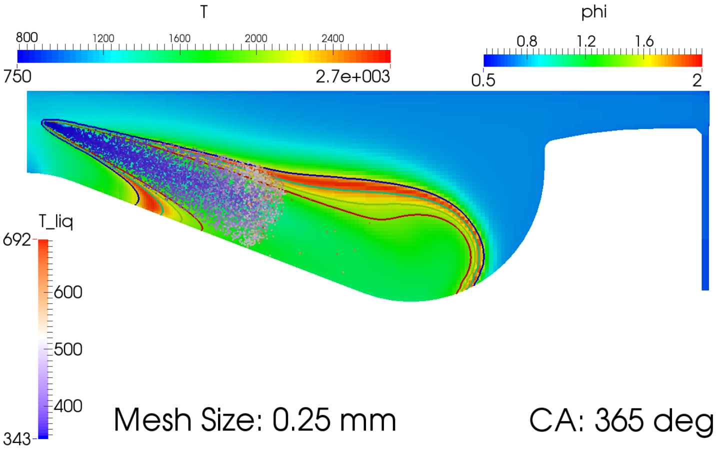

Figure 5.40: *Flame structure at 365 CA-deg. Minimum mesh size 0.25 mm*

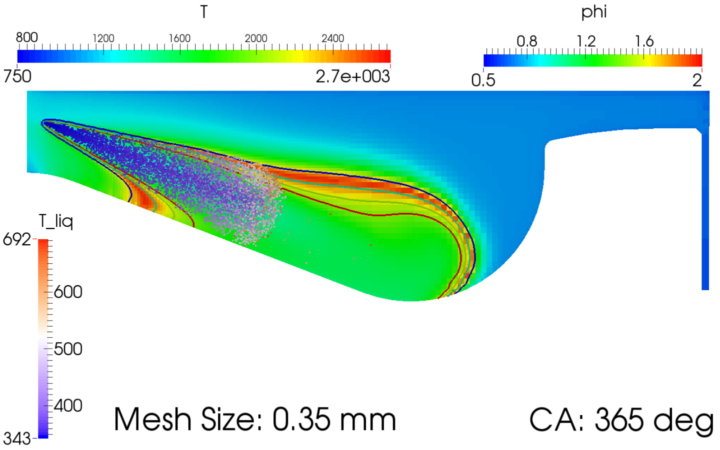

Figure 5.41: *Flame structure at 365 CA-deg. Minimum mesh size 0.35 mm*

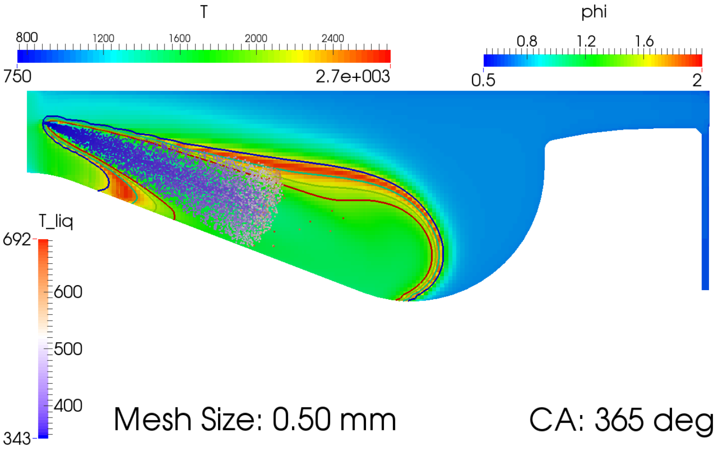

Figure 5.42: *Flame structure at 365 CA-deg. Minimum mesh size 0.50 mm*

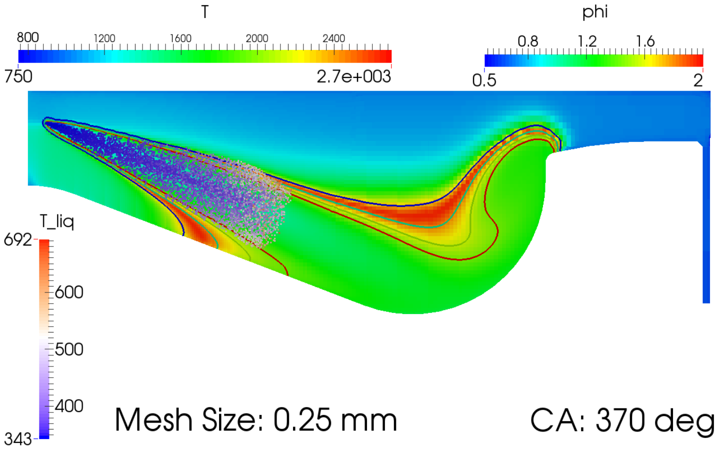

Figure 5.43: *Flame structure at 370 CA-deg. Minimum mesh size 0.25 mm*

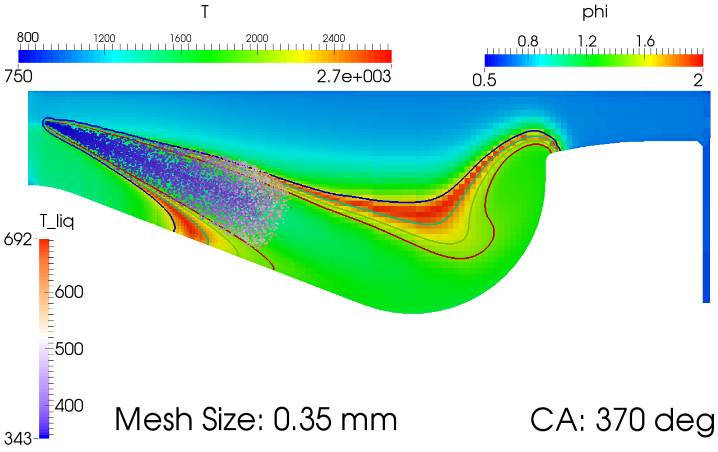

Figure 5.44: *Flame structure at 370 CA-deg. Minimum mesh size 0.35 mm*

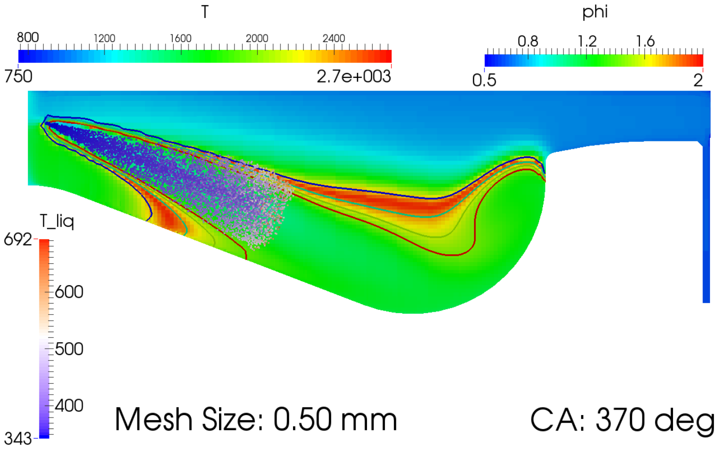

Figure 5.45: *Flame structure at 370 CA-deg. Minimum mesh size 0.50 mm*

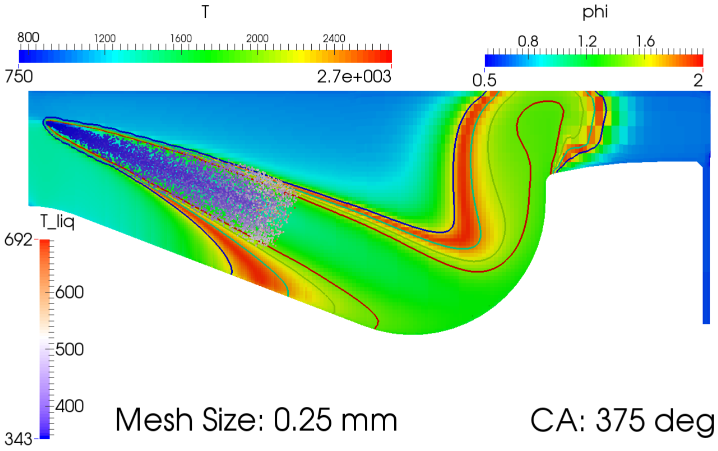

Figure 5.46: *Flame structure at 375 CA-deg. Minimum mesh size 0.25 mm*

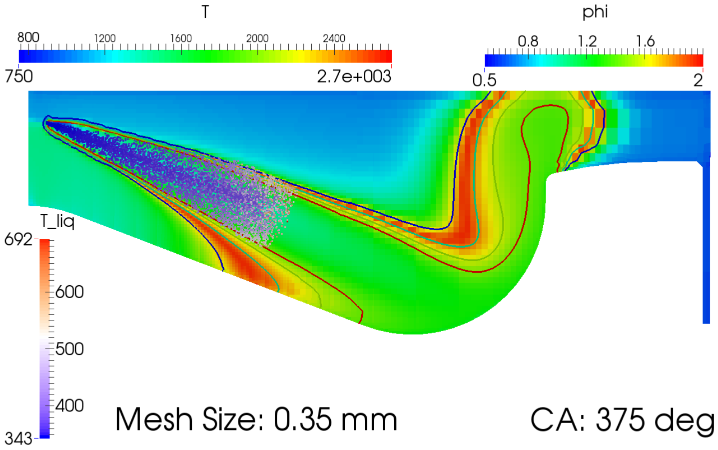

Figure 5.47: *Flame structure at 375 CA-deg. Minimum mesh size 0.35 mm*

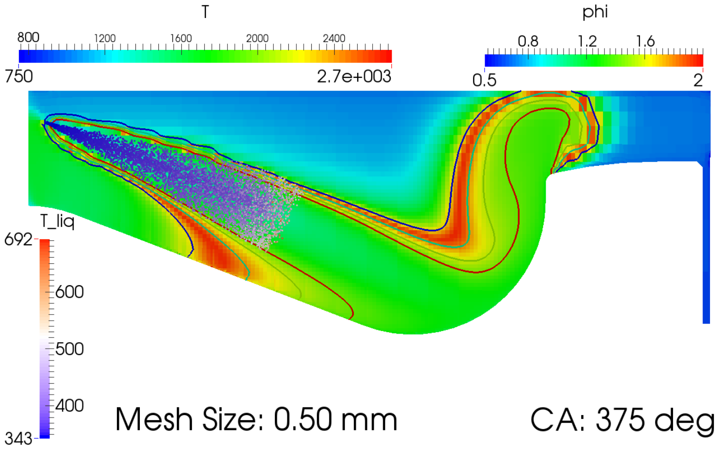

Figure 5.48: *Flame structure at 375 CA-deg. Minimum mesh size 0.50 mm*

5.6 Conclusions

This chapter presented an improved and extended version of the methodology explained in Chap. 4. The possibility to employ automatically generation of Cartesian meshes for sector engine cases with OpenFOAM was shown to be feasible. The new implementation was tested on a CAT Engine by means of RANS simulations and sensitivity analysis on varying minimum mesh size. Three different structures were evaluated with the aim of investigating eventual spray-grid dependency and ability to predict global quantities like heat release and in-cylinder pressure.

The adoption of three different minimum mesh sizes (0.25, 0.35 and 0.5 mm) globally led to similar results. The two finer grids resulted to be very consistent with each other in terms of heat release and pressure, while the coarser one showed a slight overestimation of cumulated heat release. However, all of them were able to catch the general trend, even if some differences were found in terms of instantaneous heat release and, consequently, in-cylinder pressure.

Good grid convergence was found in all the analyzed quantities. In particular, the 0.35 and 0.25 mm cases gave very similar results in terms of liquid spray behavior: both steady state values and transient trends were caught similarly in a monotonic trend that included also the 0.5 mm case. Nothing could be said in terms of accuracy of these results. Only new studies including further experimental measurements would help understanding the goodness of the spray setup.

Finally, an analysis in terms of flame structure in both CFD and mixture fraction domain was carried out. The three meshes were able to describe a plausible flame and good qualitative convergence was obtained on decreasing minimum mesh size. Again, nothing could be said in terms of accuracy for which a comparison with experimental measurements run on an engine with optical access would be needed.

CHAPTER 6

Final conclusions

Preliminary conclusions have been drawn already at the end of each chapter. These last part will discuss the thesis as a whole trying to give an overview of the achieved results.

Every effort made during the PhD course was in the direction of improvement and innovation. The approaches here discussed represented an attempt of reducing variability in engine simulations involving Eulerian-Lagrangian modeling of Diesel sprays and adoption of Cartesian meshes. Everything was made in order to make these methodologies applicable to industrial cases, especially heavy-duty applications.

Chap. 3 discussed a new approach for Eulerian-Lagrangian interaction based on the DDM by Dukowicz [13]. The way parcels and mesh interact was changed by placing a spherical volume around each parcel. This led to a strong reduction of results dependence on the injector position within the hosting cell, i.e., on the path followed by the parcel within the Eulerian domain.

The new approach was successfully validated by comparing numerical result with experimental measurement of the ECN Spray A. A sensitivity analysis was carried out on varying initial and boundary conditions and also on varying spray-grid mutual orientation. Results showed a good ability of the employed submodels to predict trends and numerical values on varying ambient density and injection pressure. Spray morphology was shown to be practically independent of nozzle position and both global and local parameters analysis were performed. When applied to a full 3D engine case, the SVI approach was able to reduce appreciably nozzle-to-nozzle differences in terms of mixture fraction and axial velocity profiles.

Chap. 4 and Chap. 5 introduced a novel approach for automatic mesh generation of Cartesian grids for engine simulations. Both an open cycle and a closed one were simulated to assess the validity of the new methodology. Chap. 4 focused on the comparison of RANS simulations with a large set of experimental data available for the

Sandia TCC engine. Different mesh structures and discretization orders were tested showing that accurate, full-cycle simulations are possible. However mesh structure and in particular size close to the valves played a big role in computed results, probably even more than the approach used for turbulence. Last chapter showed that this methodology could be extended to sector cases. An industrial engine was simulated and results were compared to available experimental data. Where experimental measurement were not available a qualitative analysis was performed on global spray related quantities and on flame structure. Results showed a good ability of catching the trends of experimental apparent heat release and in-cylinder pressure. Nevertheless, there is much space for improvement and the possibility of simulating an optical engine for which experimental data involving combustion are available could give the chance to assess better the capabilities of the new methodology.

Appendices

APPENDIX A

KHRT break-up model

The implementation of the KHRT model adopted in this work combines two models in a competing manner: the Kelvin-Helmoltz (KH) and the Rayleigh-Taylor (RT). The first model applied by the algorithm is the RT. If the conditions to apply it are not satisfied, the algorithm proceeds to apply the KH routine.

In the near nozzle region the governing breakup mechanism is the one modeled by the Kelvin-Helmoltz theory. Reitz [7] showed that the wave-breakup theory describing the development of KH instabilities on a jet surface can be applied to model both primary and secondary atomization of droplets. In KH model the breakup time is computed as follows:

$$\tau_{\mathrm{KH}} = 3.788 B_1 \frac{r_p}{\Lambda_{\mathrm{KH}} \Omega_{\mathrm{KH}}} \tag{A.1}$$

where Λ_{KH} and Ω_{KH} are respectively wavelength and maximum growth rate of the liquid surface perturbations usually caused by effects of the inner nozzle flow, e.g. by turbulence within the liquid phase. The full analytical formulation can be found in the work of Reitz [7] who proposed also the curve-fits of numerical solutions that are reported here:

$$\Lambda_{\mathrm{KH}} = 9.02\, r_p \, \frac{(1 + 0.45\sqrt{\mathrm{Oh}})(1 + 0.4\mathrm{Ta}^{0.7})}{(1 + 0.865\mathrm{We}_g^{1.67})^{0.6}} \tag{A.2}$$

$$\Omega_{\mathrm{KH}} = \frac{(0.34 + 0.38\mathrm{We}_g^{1.5})}{(1 + \mathrm{Oh})(1 + 1.4\mathrm{Ta}^{0.6})} \sqrt{\frac{\sigma}{\rho_l r_p^3}} \tag{A.3}$$

During the KH routine the parent parcel can undergo two different mechanisms. The first is the enlargement of the droplet that can only occur if simultaneously τ_{KH} is larger than the perturbations lifetime and the wavelength satisfies the relation $r_p < B_0 \lambda_{\mathrm{KH}}$

(whit B_0 constant of the KH model usually equal to 0.61). This mechanism can occur only once for each parcel and only if the other mechanisms have not occurred yet.

$$r_{p,new} = \min \begin{cases} \sqrt[3]{3\pi r_p^2 \dfrac{\mathrm{U}_{rel}}{2\Omega_{\mathrm{KH}}}} \\ \sqrt[3]{3 r_p^2 \dfrac{\Lambda_{\mathrm{KH}}}{4}} \end{cases} \tag{A.4}$$

The second mechanism in KH is also the main one. If the child droplets radius $r_c = B_0\lambda_{\mathrm{KH}}$ is smaller than the parent droplet radius the KH algorithm checks if stripping breakup can occur. Due to the breakup and generation of new small droplets, the size of the original droplet is reduced. The temporal change in diameter of the parent droplet is given by:

$$\frac{dr_p}{dt} = -\frac{r_{p,new} - r_c}{\tau_{\mathrm{KH}}} \tag{A.5}$$

from which through an implicit integration it is possible to obtain the updated radius of the parent droplet:

$$r_{p,new} = \frac{f r_c + r_p}{1 + f} \tag{A.6}$$

with $f = \Delta t/\tau_{\mathrm{KH}}$.
The stripped mass is calculated as:

$$m_s = m_p \left(1 - \frac{d_{p,new}^3}{d_p^3}\right) \tag{A.7}$$

whit which it is possible to calculate the number of droplets in the child parcel:

$$N_c = \frac{6 m_s}{\rho_l \pi d_c^3} \tag{A.8}$$

If the number of child droplets, N_c, is larger than the number of droplets contained in the parent parcel, N_p, the breakup occurs and a new parcel of mass m_s is generated.
To save computational resources the stripped mass is accumulated till it reaches the 3% of the parent parcel mass [29], when the breakup occurs. During and after this phase the total number of droplets in the parent parcel is conserved. This means that a parcel that undergoes only KH breakup will have always the same number of droplets assigned at the moment of the injection. This is done because the idea is to describe the stripping breakup as a detachment of mass from the parent droplet to create new droplets. Since in a parcel the included droplets are all equal and they undergo the same mechanisms, the behavior has to be the same and they have to generate at least one child droplet each. Once a new parcel is generated it is given the same temperature and physical location as the parent and the radius is given $r_c = B_0\lambda_{\mathrm{KH}}$. It is given the same velocity in terms of magnitude but it is also introduced a small deviation from the original direction by means of casual generation of the two components in the plane orthogonal to the parent parcel direction.
Downstream of the nozzle Rayleigh-Taylor breakup takes place. The RT breakup model is based on the theoretical considerations of Taylor [30] who investigated the stability of liquid-gas interfaces when accelerated in a normal direction with respect to the plane

that contains them. If the directions of acceleration and density gradient are concordant the interface will result stable, otherwise Rayleigh-Taylor instabilities can develop. In the case of a liquid droplet decelerated by drag forces in a gas phase, these instabilities may grow at the trailing edge of the droplet.The droplet acceleration is expressed as:

$$\mathbf{a}_d = \frac{3}{8} C_d \frac{\rho_g}{\rho_l} \frac{|\mathbf{u}_{rel}|^2}{r} \tag{A.9}$$

where C_d is the drag coefficient and $\mathbf{u}_{rel}$ is the relative velocity between liquid and gas. The gas velocity is interpolated at the parcel position using the technique explained in Sec. 3.2.7. By means of the droplet acceleration it is possible to calculate the frequency and wavelength of the fastest growing waves:

$$\Omega_{\mathrm{RT}} = \sqrt{\frac{2}{3\sqrt{3\sigma}} \frac{\left[|\mathbf{a}_d|(\rho_l - \rho_g)\right]^{3/2}}{\rho_l + \rho_g}} \tag{A.10}$$

$$\Lambda_{\mathrm{RT}} = C_{\mathrm{RT}} 2\pi \sqrt{\frac{3\sigma}{|\mathbf{a}_d|(\rho_l - \rho_g)}} \tag{A.11}$$

In the Eqs. A.10 and A.11 σ is the surface tension and C_{RT} is a tunable constant to allow a modification of the effective wavelength. It accounts for unknown effects of initial conditions like turbulence and cavitation inside the nozzle on the secondary breakup. RT breakup occurs only if the wavelength Λ_{RT} is smaller than the the droplet diameter and if the lifetime of the instabilities is greater than a breakup time calculated as:

$$\tau_{\mathrm{RT}} = \frac{C_\tau}{\Omega_{\mathrm{RT}}} \tag{A.12}$$

with C_τ as a tunable constant for reducing or increasing the break-up time to match experimental results. Furthermore in this implementation of the KHRT, the use of a breakup length was made. RT breakup is completely excluded if the distance between the parcel and the injector nozzle is smaller than a certain threshold calculated as follow:

$$L_{bu} = C_{bu} d_{noz} \sqrt{\frac{\rho_l(T_{inj})}{\rho_g}} \tag{A.13}$$

Here C_{bu} is a tunable constant and the liquid density value is taken at the injection temperature. The use of a breakup length is justified in [33], [101] and [102]: experimental results have shown that diesel spray penetration has different rates within and beyond a breakup length near the nozzle exit and this may be attributed to the existence of an intact liquid core close to the nozzle. The used threshold allows to catch better this behavior. Tab. A.1 summarizes the values adopted for each constants present in the KHRT breakup model:

B_0	B_1	C_{RT}	C_τ	C_{bu}
0.61	25	0.2	0.2	25

Table A.1: *KHRT breakup model constants*

Bibliography

[1] G. Stiesch. *Modeling engine spray and combustion processes*. Springer-Verlag BerlinHeidelberg GmbH, 2nd edition, 2003.

[2] C. Baumgarten, Y. Shi, R. Busch, and G. P. Merker. Numerical and experimental investigations of cavitating flow in high pressure diesel nozzles. In *Proceeding of 17th ILASS-Europe Conference*, pages 593–599, Zurich, Switzerland, September 2-6, 2001.

[3] C. C. Miesse. Correlation of experimental data on the disintegration of liquid jets. *Journal of Industrial & Engineering chemistry*, 47:1690, 1955.

[4] W. Ohnesorge. Die bildung von tropfen an düsen und auflösung flüssiger strahlen (formation of drops by nozzles and breakup of liquid jets). *Zeitschrift für Angewandte Mathematik und Mechanik*, 16:355, 1936.

[5] R. D. Reitz. *Atomization and Other Breakup Regimes of a Liquid Jet*. PhD thesis, Princeton University, 1978.

[6] R. D. Reitz. *Computer modeling of sprays. Spray Technology short course*. Pittsburgh, PA, May 7, 1996.

[7] R. D. Reitz. Modeling atomization processes in high-pressure vaporizing sprays. *Atomization and Spray Technology*, 3:309–337, 1987.

[8] A. Wierzba. Deformation and breakup of liquid drops in agas stream at nearly critical weber numbers. *Experiments in Fluids*, 9:59–64, 1993.

[9] P. J. O'Rourke. *Collective Drop Effects on Vaporizing Liquid Sprays*. PhD thesis, Princeton University, 1981.

[10] F. A. Williams. *Combustion Theory*. The Benjamin/Cummings Publishing Company, Inc., 2727 Sand Hill Road - Menlo Park, CA 94025 USA, 2nd edition, 1985.

[11] H. C. Gupta and F. V. Bracco. Numerical computations of two-dimensional unsteady sprays for application to engines. *AIAA Journal*, 16(10):1053–1061, 1978.

[12] J. B. Heywood. *Internal Combustion Engine Fundamentals*. McGraw-Hill, New York, NY, 1988.

[13] J. K. Dukowicz. A particle-fluid numerical model for liquid sprays. *Journal of Computational Physics*, 35:229–253, 1980.

[14] F. V. Bracco. Modeling of engine sprays. *SAE Technical Paper 850394*, 1985.

[15] C. T. Crowe, M. P. Sharma, and D. E. Stock. The particle-source-in cell method for gas droplet flow. *ASME Journals of Fluids Engineering*, 99:325–332, 1977.

[16] P. J. O'Rourke and F. V. Bracco. Modeling of drop interactions in thick sprays and a comparison with experiments. In *Conference on Stratified Charge Automotive Engines*, volume 9, pages 101–116. Institution of Mechanical Engineers (IMechE), November 1980.

[17] A. B. Liu, D. Mather, and R. D. Reitz. Modeling the effects of drop drag and breakup on fuel sprays. *SAE Technical Paper 930072*, 1993.

[18] B. E. Launder and B. I. Sharma. Application of the energy dissipation model of turbulence to the calculation of flow near a spinning disc. *Letters in heat and mass transfer*, 1:131–138, 1974.

[19] C. T. Crowe, J. N. Chung, and T. R. Troutt. Particle mixing in free shear flows. *Progress in Energy and Combustion Science*, 14:171–194, January 1988.

[20] D. Modarress, J. Wuerer, and S. Elghobashi. An experimental study of a turbulent round two-phase jet. *Paper AIAA-82-0964*, 1982.

[21] R. Tatschl, C. Künsberg Sarre, and E. Berg. Ic-engine spray modeling - status and outlook. In *Proceeding of 12th International Multidimensional Engine Modeling User's Group Meeting*, Detroit, MI, 2002. SAE Congress 2002.

[22] C.Arcoumanis, M. Gavaises, and B. French. Effect of fuel injection process on the structure of diesel sprays. *SAE Technical Paper 970799*, 1997.

[23] R. D. Reitz and F. V. Bracco. Mechanisms of breakup of round liquid jets. In Cheremisinoff NP, editor, *The Encyclopedia of Fluid Mechanics*, volume 3, pages 233–249, Houston, TX, 1986. Gulf Publishing.

[24] T. P. Torda. Evaporation of drops and the breakup of sprays. *Astronautica Acta*, 18:383, 1973.

[25] W. E. Ranz. *On Sprays and Spraying: A Survey of Spray Technology for Research and Development Engineers*. Department Of Engineering Research, Bulletin No. 65, Penn State University, 1956.

[26] R. D. Reitz and F. V. Bracco. Mechanism of atomization of liquid jets. *The Physics of Fluids*, 25, 1982.

[27] Z. Liu, T. Obokata, and R. D. Reitz. Modeling drop drag effects on fuel spray impingement in direct injection diesel engines. *SAE Technical Paper 970879*, 1997.

[28] P. J. O'Rourke and A. A. Amsden. The tab method far numerical calculation of spray droplet breakup. *SAE Technical Paper 872089*, 1987.

[29] M. A. Patterson and R.D. Reitz. Modeling the effects of fuel spray characteristics on diesel engine combustion and emission. *SAE Technical Paper 980131*, 1998.

[30] G. I. Taylor. The instability of liquid surfaces when accelerated in a direction perpendicular to their planes. *Batchelor GK, The scientific paper of G. I. Taylor*, 3:532–536, 1963.

[31] R. Bellman and R. H. Pennington. Effects of surface tension and viscosity on taylor instability. *Quarterly of Applied Mathematics*, 12:151–162, 1954.

[32] T. F. Su, M. A. Patterson, and R.D. Reitz. Experimental and numerical studies of high pressure multiple injection sprays. *SAE Technical Paper 960861*, 1996.

[33] M. Chan, S. Das, and R.D. Reitz. Modeling multiple injection and egr effects on diesel engine emissions. *SAE Technical Paper 972864*, 1997.

[34] M. Renksizbulut and M. C. Yuen. Experimental study of droplet evaporation in a high temperature air stream. *ASME Journal of Heat Transfer*, 106:384–388, 1983.

[35] M. Gavaises. *Modelling of Diesel Fuel Injection Processes*. PhD thesis, Imperial College, University of London, 1997.

[36] F. P. Incropera and D. P. DeWitt. *Introduction to Heat Transfer*. Wiley, New York, NY, USA, 3rd edition, 1996.

[37] C. H. Chiang, M. S. Raju, and W. A. Sirignano. Numerical analysis of convecting, vaporizing fuel droplet with variable properties. *International Journal of Heat and Mass Transfer*, 35(5):1307–1324, 1992.

[38] H. A. Dwier, P. Stapf, and R. R. Maly. Unsteady vaporization and ignition of a three-dimensional droplet array. *Combustion & Flame*, 121(1-2):181–194, 2000.

[39] R. J. Haywood, R. Nafziger, and M. Renksizbulut. A detailed examination of gas an liquid phase transient processes in convective droplet evaporation. *ASME Journal of Heat Transfer*, 111:495–502, 1989.

[40] S. K. Aggarwal. Modeling of a dilute vaporizing multicomponent fuel spray. *International Journal of Heat and Mass Transfer*, 30(9):1949–1961, 1987.

[41] N. Abani, A. Munnannur, and R. D. Reitz. Icef 2007-1667. reduction in numerical parameter dependencies in diesel spray models. In *Proc. ASME Internal Combustion Engine Division*. Charleston, South Carolina, USA, 2007.

[42] S. Post, V. Iyer, and J. Abraham. A study of the near-field entrainment in gas jets and sprays under diesel conditions. *ASME Journals of Fluids Engineering*, 122:385–395, 2000.

[43] Sandia ECN website *http://www.sandia.gov/ecn/*. Engine Combustion Network, February 2015.

[44] J. Abraham and V. Magi. A virtual liquid source (vls) model for vaporizing diesel sprays. *SAE Technical Paper 1999-01-0911*, 1999.

[45] D. P. Schmidt and C. J. Rutland. A new droplet collision algorithm. *Journal of Computational Physics*, 164:62–80, 2000.

[46] A. Kösters and A. Karlsson. A comprehensive numerical study of diesel fuel spray formation and combustion in openfoam. *SAE Technical Paper 2011-01-0842*, 2011.

[47] G. D'Errico, G. Ettorre, and T. Lucchini. Comparison of combustion and pollutant emission models for di diesel engines. *SAE Technical Paper 2007-24-0045*, 2007.

[48] G. D'Errico, T. Lucchini, F. Atzler, and R. Rotondi. Computational fluid dynamics simulation of diesel engines with sophisticated injection strategies for in-cyinder pollutant controls. *Energy and fuels*, 26:4212–4223, 2012.

[49] N. Nordin. *Complex chemistry modeling of diesel spray combustion*. PhD thesis, Chalmers University of Technology, Department of Thermo Fluid Dynamics, 2001.

[50] H. Jasak. *Error analysis and estimation for the finite volume method with applications to fluid flows*. PhD thesis, Imperial College of Science, Technology and Medicine, London, UK, 1996.

[51] H. J. Ferziger and M. Perik. *Computational methods for fluid dynamics*. Springer, 2002.

[52] R. I. Issa. Solution of the implicitly discretized fluid flow equations by operator-splitting. *Journal of Computational Physics*, 1986.

[53] C. Huang and A. Lipatnikov. Modeling of gasoline and ethanol hollow-cone sprays using openfoam. *SAE Technical Paper 2011-01-1896*, 2011.

[54] C. Kralj. *Numerical simulation of Diesel spray processes*. PhD thesis, Imperial College of Science, Technology and Medicine, 1995.

[55] C. Crowe, M. Sommerfeld, and Y. Tsuji. *Multiphase flows with droplets and particles*. CRC Press LLC, 1998.

[56] H. Kosaka, T. Suzuki, and T. Kamimoto. Numerical simulation of turbulent dispersion of fuel droplets in an unsteady spray via discrete vortex method. *SAE Technical Paper 952433*, 1995.

[57] C. Baumgarten. *Mixture formation in internal combustion engines*. Springer, 2006.

[58] T. Lucchini, G. D'Errico, and D. Ettorre. Numerical investigation of the spray-mesh-turbulence interactions for high-pressure, evaporating sprays at engine conditions. *International Journal of Heat and Fluid Flow*, 32:285–297, 2011.

[59] J. M. García-Oliver, J. M. Pastor, A. Pandal, N. Trask, E. Baldwin, and D.P. Schmidt. Diesel spray cfd simulations based on the sigma-y eulerian atomization model. *Atomization and Sprays*, 23:71–95, 2013.

[60] CMT website *http://www.cmt.upv.es/ECN03.aspx*. CMT-Motores Térmicos, Universitat Politècnica de València, February 2015.

[61] G. D. Vahl and G.D. Mallinson. False diffusion in numerical fluid mechanics. Report 1972/FM/1. *University of New South Wales, School of Mechanical and Industrial Engineering*, 1972.

[62] OpenFOAM website *http://www.openfoam.org/*. The OpenFOAM Foundation, February 2015.

[63] S. Gaikwad, K. Arora, V. Korivi, and S. Cho. Steady and transient cfd approach for port optimization. *SAE International Journal of Materials and Manufacturing*, 1:754–762, 2009.

[64] J. W. Campbell, G. Hardy, and F. Personeni. Diesel engine intake port-flow stability and application of cfd using a hybrid-low-reynolds new wall method. *THIESEL 2006 Conference on Thermo- and Fluid Dynamic Processes in Diesel Engines*, pages 569–588, 2006.

[65] O. Colin, A. Benkenida, and C. Angelberger. 3d modeling of mixing, ignition and combustion phenomena in highly stratified gasoline engines. *Oil and Gas Science and Technology*, 58:47–62, 2003.

[66] S. Singh, R. D. Reitz, and M. P. B. Musculus. Comparison of the characteristic time (ctc), representative interactive flamelet (rif), and direct integration with detailed chemistry combustion models against optical diagnostic data for multi-mode combustion in a heavy-duty di diesel engine. *SAE Technical Paper 2006-01-0055*, 2006.

[67] T. Lucchini, G. D'Errico, A. Onorati, G. Bonandrini, L. Venturoli, and R. Di Gioia. Development of a cfd approach to model fuel-air mixing in gasoline direct-injection engines. *SAE Technical Paper 2012-01-0146*, 2012.

[68] G. Bonandrini, R. Di Gioia, D. Papaleo, and L. Venturoli. Numerical study on multiple injection strategies in disi engines for particulate emission control. *SAE Technical Paper 2012-01-0400*, 2012.

[69] R. N. Dahms, T.D. Fansler, M.C. Drake, T. W. Kuo, A.M. Lippert, and N. Peters. Modeling ignition phenomena in spray-guided spark-ignited engines. *Proceedings of the Combustion Institute*, 32(2):2743–2750, 2009.

[70] A. D. Gosman. State of the art of multi-dimensional modeling of engine reacting flows. *Oil and Gas Science and Technology*, 54(2), 1999.

[71] H. Barths, C. Hasse, and N. Peters. Computational fluid dynamics modelling of non-premixed combustion in direct injection diesel engines. *International Journal of Engine Research*, 1(3):249–267, 2000.

[72] J. P. Duclos, M. Zolver, and T. Baritaud. 3d modeling of combustion for di-si engines. *Oil and Gas Science and Technology*, 54:259–264, 1999.

[73] K. Y. Huh and A. D. Gosman. A phenomenological model of diesel spray atomization. *Proceedings of the International Conference on Multiphase Flows*, 2009.

[74] C. Bai and A. D. Gosman. Mathematical modeling of wall films formed by spray wall interaction. *SAE Technical Paper 960626*, 1996.

[75] R. N. Dahms, M. C. Drake, T. D. Fansler, T. W. Kuo, and N. Peters. Understanding ignition processes in spray-guided gasoline engines using high-speed imaging and the extended spark-ignition model sparkcimm. part a: Spark channel processes and the turbulent flame front propagation. *Combustion and Flame*, 158(11):2229–2244, 2011.

[76] H. Jasak, J. Y. Luo, B. Kaludercic, A. D. Gosman, H. Echtle, Z. Liang, F. Wirbeleit, M. Wierse, S. Rips, A. Werner, G. Fernström, and A. Karlsson. Rapid cfd simulation of internal combustion engines. *SAE Technical Paper 1999-01-1185*, 1999.

[77] H. Si, J. Fuhrmann, and K. Gartner. Boundary conforming delaunay mesh generation. *Computational Mathematics and Mathematical Physics*, 50(1):38–53, 2010.

[78] J. Schoberl. Netgen an advancing front 2d/3d-mesh generator based on abstract rules. *Computing and Visualization in Science*, 6:41–52, 1997.

[79] N. Sinha, P. Cavallo, R. Lee, A. Hosangadi, D. C. Kenzakowski, S.M. Dash, H. Affes, and D. Chu. Novel cfd techniques for in-cylinder flows on tetrahedral grids. *SAE Technical Paper 980138*, 1998.

[80] D. Schmidt, S. Toninel, S. Filippone, and G. Bianchi. Parallel computation of mesh motion for cfd of ic engines. *SAE Technical Paper 2008-01-0976*, 2008.

[81] P. K. Senecal, K. J. Richards, E. Pomraning, T. Yang, M. Z. Dai, R. M. McDavid, M. A. Patterson, S. Hou, and T. Shethaji. A new parallel cut-cell cartesian cfd code for rapid grid generation applied to in-cylinder diesel engine simulations. *SAE Technical Paper 2007-01-0159*, 2007.

[82] X. Yang, A. Solomon, and T. Kuo. Ignition and combustion simulations of spray-guided sidi engine using arrhenius combustion with spark-energy deposition model. *SAE Technical Paper 2012-01-0147*, 2012.

[83] Z. Wang, R. Scarcelli, S. Som, and S. McConnell et al. Multi-dimensional modeling and validation of combustion in a high-efficiency dual-fuel light-duty engine. *SAE Technical Paper 2013-01-1091*, 2013.

[84] R. Scarcelli, N. Matthias, and T. Wallner. Numerical investigation of combustion in a lean burn gasoline engine. *SAE Technical Paper 2013-24-0009*, 2013.

[85] T. Lucchini, G. D'Errico, H. Jasak, and Z. Tukovic. Automatic mesh motion with topological changes for engine simulation. *SAE Technical Paper 2007-01-0170*, 2007.

[86] T. Lucchini, G. D'Errico, and M. Fiocco. Multi-dimensional modeling of gas exchange and fuel-air mixing processes in a direct-injection, gas fueled engine. *SAE Technical Paper 2011-24-0036*, 2011.

[87] T. Lucchini, G. D'Errico, F. Brusiani, and G. Bianchi. A finite-element based mesh motion technique for internal combustion engine simulations. *International Conference on Modeling and Diagnostics for Advanced Engine systems*, 2(3), 2008.

[88] H. Jasak and Z. Tuković. Automatic mesh motion for the unstructured finite volume method. *Transactions of FAMENA*, 30(2):1–18, 2007.

[89] P. M. Knupp. Algebraic mesh quality metrics for unstructured initial meshes. *Finite Elements in Analysis and Design*, 39:217–241, 2003.

[90] J. H. Ferziger and M. Peric. *Computational Methods for Fluid Dynamics*. Springer, 2002.

[91] D. L. Reuss, R. J. Adrian, C. C. Landreth, D. T. French, and T. D. Fansler. Instantaneous planar measurements of velocity and large-scale vorticity and strain rate in an engine using particle-image velocimetry. *SAE Technical Paper 890616*, 1989.

[92] D. L. Reuss, T. Kuo, B. Khalighi, D. Haworth, and M. Rosalik. Particle image velocimetry measurements in a high-swirl engine used for evaluation of computational fluid dynamics calculations. *SAE Technical Paper 952381*, 1995.

[93] A.Y. Alharbi and V. Sick. Investigation of boundary layers in internal combustion engines using a hybrid algorithm of high speed micro-piv and ptv. *Experiment in Fluids*, 49(4):949–959, 2010.

[94] D. C. Haworth. Large-eddy simulation of in-cylinder flows. *Oil and Gas Science and Technology*, 54(2):175–185, 1999.

[95] K. Liu and D. C. Haworth. Large-eddy simulation for an axisymmetric piston-cylinder assembly with and without swirl. *Flow, Turbulence & Combustion*, 85:279–307, 2010.

[96] P. Abraham, K. Liu, D. Haworth, D. Reuss, , and V. Sick. Evaluating large-eddy simulation (les) and high-speed particle image velocimetry (piv) with phase-invariant proper orthogonal decomposition (pod). *Oil and Gas Science and Technology, proceedings of LES4ICE 2012 - Large Eddy Simulation for Internal Combustion Engine Flows*, 2013.

[97] P. E. Farrell and J. R. Maddison. Conservative interpolation between volume meshes by local galerkin projection. *Computer Methods in Applied Mechanics and Engineering*, 200(1-4):89–100, January 2011.

[98] M. Jangi and X. S. Bai. Multidimensional chemistry coordinate mapping approach for combustion modelling with finite-rate chemistry. *Combustion Theory and Modelling*, 16(6).

[99] F. Contino, H. Jeanmart, T. Lucchini, and G. D'Errico. Coupling of in situ adaptive tabulation and dynamic adaptive chemistry: An effective method for solving combustion in engine simulations. *Proceedings of the Combustion Institute*, 33:3057–3064, 2011.

[100] A. Krishnasamy, R. Reitz, W. Willems, and E. Kurtz. Surrogate diesel fuel models for low temperature combustion. *SAE Technical Paper 2013-01-1092*, 2013.

[101] C. F. Powell, Y. Yue, R. Poola, J. Wang, M. C. Lai, and J. Shaller. X-ray measurements of high pressure fuel sprays. *SAE Technical Paper 2001-01-0531*, 2001.

[102] A. Linne, M. Paciaroni, T. Hall, and T. Parker. Ballistic imaging of the near field in a diesel spray. *Experiments in fluids*, 40:836–846, 2006.